CONSTRICTED CURRENT PERPENDICULAR TO PLANE (CPP) MAGNETIC SENSOR VIA ELECTROPLATING

A DISSERTATION
SUBMITTED TO THE FACULTY OF THE GRADUATE SCHOOL
OF THE UNIVERSITY OF MINNESOTA
BY

Xiaobo Huang

IN PARTIAL FULFILLMENT OF THE REQUIREMENTS
FOR THE DEGREE OF
DOCTOROF PHILOSOPHY

Bethanie J.H. Stadler, Advisor

JANUARY 2011

Acknowledgments

I would like to take this opportunity to extend my deepest gratitude to following people who have been greatly helpful, supportive and encouraging.

First of all, I would like to convey my sincere thanks and appreciation to my advisor, Dr. Bethanie J. Hills Stadler, for her inspiring and encouraging way, patience to guide me to a deeper understanding of knowledge and research throughout my graduate study.

I am grateful to Dr. Stephen Campbell, for serving as the Chair of the Examination Committee. I thank Dr. Tianhong Cui and Dr. Rhonda Franklin for serving in the Examination Committee.

I also would like to thank NMP group members, Dr. Liwen Tan, Dr. Patrick McGary, Dr. Xiaoyuan Qi, Dr. Sang-Yeob Sang, Dr. Ratnanjali, Khandwal, Neeta Basantkumar, Neel Speetzen, Vladimir Makarov, Mazin Maqableh, Madhukar Reddy, and Anirudh Sharma. In this group, we are not only as group mates, but also good friends.

At last, I would like to express my deep sense of appreciation to my wife, Hao, for supporting me with her love and understanding.

Abstract

Electrochemically deposited magnetic nanowires have gained increasing attention since current perpendicular to the plane giant magnetoresistance (CPP-GMR) was observed in multilayered nanowires. Magnetic nanowires have potential for fundamental studies, including measuring spin diffusion lengths and understanding the mechanisms of the electron spin transfer. They also have great potential technological applications as CPP-GMR sensors, magnetic random access memory (MRAM), and next generation magnetic recording heads. Small diameter nanowires are desired in order to have large current density per device and a high areal density for device arrays, for example, 2 Tb/in^2 media. In this research, E-beam lithography, nano-imprinting, and self-assembled nanoporous alumina templates (AAO) were studied to achieve as small diameter nanopores as possible. AAO templates with 10 nm diameter were fabricated using both Al foils and Al thin films. Very small diameter (10 nm) CPP-GMR Co/Cu nanowires were fabricated into AAO templates using electrochemical deposition. The magnetic transport properties of these multilayered and trilayered Co/Cu nanowires were investigated. It was found that nanowire anisotropies parallel and perpendicular to the nanowires were dependent on the thicknesses of Co and Cu layers. GMR of 19% was achieved with 10 nm diameter nanowires at room temperature. The magnetic free layers were as thin as 4.5 nm with GMR of 18%. Spin transfer torque switching current densities were measured to be

10^6 – 10^8A/cm^2. The measurement of spin transfer torque was conducted numerous times with high repeatability in the critical switching currents from parallel to antiparallel alignment ($J_{P\text{-}AP}$) and slight variations in back ($J_{AP\text{-}P}$). Small resistance area products (RA) of 0.003Ωμm ^{2} were achieved with trilayers that had 40Ω total resistance. All of results in this study show that nanowires with 10 nm diameters have potential application as next generation CCP-GMR sensors and spin transfer torque MRAM.

Table of Contents

List of Tables

List of Figures

Chapter 1

Chapter 2

Chapter 3

CHAPTER 1 INTRODUCTION

Nanostructured magnetic materials have attracted both scientific and technological interest due to new properties. They have potential applications in next generation magnetic storage techniques, for example, giant magnetoresistance (GMR), tunneling magnetoresistance (TMR), magnetic random access memory (MRAM), and magnetic recording media. Nanostructured magnetic materials can be fabricated by two types of methods. One type involves top-down methods. Magnetic materials are deposited by vacuum techniques, then lithography and etching process are used to define structures. On the other hand, bottom-up methods, for example electrodeposition into nanoporous templates, involve building nanostructures "*in situ"*. Electrodeposition is one of the most efficient, convenient, and cost-effective methods for fabricating nanostructured materials.

1.1 Magnetic Sensors Fabricated by Thin Film Technologies

1.1.1 Giant Magnetoresistance (GMR) Sensors

Baibich *et al.* (1)found GMR in Fe(001)/Cr(001) superlattice multilayer deposited by Molecular Beam Epitaxy (MBE) at 4.2 K in 1988. The highest magnetoresistance was observed in [(Fe 30 Å)/(Cr 9 Å)]. Parkin *et al.* (2) found GMR of 6.5% in multilayered Fe/Cr structures fabricated by sputtering in 1990, and demonstrated that the thickness of the Cr layers had an effect on magnetic properties of multilayer structures due to Ruderman-Kittel-Kasuya-Yosida (RKKY) interactions. RKKY

refers to a coupling mechanism of nuclear magnetic moments. The GMR of sputtered [(Co 15 Å)/(Cu 9 Å)]$_{15}$ multilayered structures obtained by Barhelemy *et al.* (3) was 78% at 2 K and 45% at 300 K. Spizzo *et al.* (4) investigated the effects of Co layer thickness on GMR of Co/Cu multilayer grown by sputtering. As the Co layer thickness was reduced, sample resistivity increased and a short range surface roughness was enhanced which increased the interfacial disorder. The enhanced resistivity led to a low GMR ratio. Dieny *et al.* (5) (6) invented spin valve structures in 1991. A spin valve structure is a sandwich structure which contains two ferromagnetic layers and one non-magnetic layer. One of the magnetic layers is a magnetically soft layer, and the other is magnetically hard layer. In the parallel state, the spin valve structure shows low resistance. In the anti-parallel state, it shows high resistance. The ferromagnetic layers are individually switched by the application of an external field. Remarkably, spin valves were commonly used as commercial hard drive readers by the end of 1990s. Shinjo *et al.* (7) found that NiFe/Cu/Co spin valve structures provided GMR of about 14% at low applied magnetic fields. TMR sensors have taken over reader head due to higher MR ratio.

GMR sensors are divided into two major types, current in the plane (CIP) GMR and current perpendicular to the plane (CPP) GMR. The physics of these two types of GMR are very different. The current is parallel to the planes of the layers in CIP-GMR. CIP-GMR is due to spin-dependent electron scattering at the interfaces or in the bulk of the ferromagnetic films. (8)In CPP-GMR, the current is perpendicular to

the planes of the layers. The spin accumulation effects were described by the model of Valet and Fert. (9) These effects are important for the CPP-GMR and not for the CIP-GMR. In CIP-GMR, the scaling length is the mean free path (λ). But, in CPP-GMR, the scaling length is the spin diffusion length (l_{sf}). People begun to focus on CPP-GMR since CPP showed higher GMR than CIP. (10) But, it is difficult for CPP-GMR to measure the resistance because the resistance of thin films is very tiny across their thickness. The first CPP-GMR measurement was performed by using superconductive leads at low temperature which limited the actual application of CPP-GMR. As nanofabrication techniques developed, nano-pillars were easily achieved. CPP-GMR has been used as readers of hard drivers and other applications.

Current-perpendicular-to-plane (CPP)-GMR readers are one option for next generation readers in hard drives due to high MR ratios and small resistance. However, as areal density increases over 300 GB/in^2, the reader size needs to be reduced accordingly. Nakamoto *et al.* (11) (12) predicted GMR readers below 40$\times$40 nm^2 perform better than tunneling magnetoresistance (TMR) readers, and they fabricated CoFe/Cu/CoFe reader with width of 80 nm by sputtering. GMR of 6 % was obtained in this structure. In order to overcome a problem of small GMR ratio, Peng *et al.*(13) developed current-confined-path (CCP) GMR reader which had the width of current path of 6 nm. The well-defined conducting channel reduced the effective current flow area resulting in an increased GMR sensor resistance. However, CCP layers have to be manufactured by using photolithography, ultrahigh vacuum

sputtering and ion milling processes, increasing the complexity of the fabrication process.

1.1.2 TMR Sensors

As mentioned above, TMR sensors have higher MR ratios than GMR sensors, therefore they are currently more popular for readers in hard drives. TMR is a magnetoresistive effect occurring in magnetic tunneling junctions. TMR sensors have similar structures as GMR sensors, but the non-magnetic layer is a thin insulator (such as, Al_2O_3, MgO). Electrons can tunnel from one magnetic layer to the other if the insulator layer is thin enough. TMR sensors are often manufactured by photolithography and thin film technology. Jullière (14) discovered the effect of TMR in Fe/GeO/Co at 4.2 K in 1975. Miyazaki *et al.* (15) found TMR of 18 % in Fe/Al_2O_3/Fe junction at room temperature. The highest TMR with Al_2O_3 insulators was 70% at 300 K. To further increase TMR ratio, a novel TMR sensor utilizing MgO as the tunnel barrier layer was recently developed. Al_2O_3 is an amorphous material. As a result, electrons are scattered, which decreases their conductivity through the barrier layer. In contrast, electrons can propagate through MgO without dispersion because the MgO deposits as a single crystal. Parkin *et al.* (16) fabricated CoFe/MgO/CoFe junction by sputtering in which TMR was 200 % at 300 K. TMR of 230% was reported by Diayaprowara *et al.* (17) from crystalline CoFeB/MgO/CoFeB at room temperature. To date, TMR of 1100% has been observed in CoFeB/MgO/CoFeB junction at 4.2 K (18). As areal density of media keeps

increasing, physical width of TMR is between 90 to 100 nm in commercial TMR heads. (19) But the resistance of TMR sensors is too high for very high areal density media due to relatively larger RA product. This limits the application of TMR as the next generation of reader (13).

1.1.3 Spin Transfer Torque Devices

Spin transfer torque switching is a new technique which has potential applications in MRAM. When a spin-polarized current flows between the magnetic layers in magnet-nonmagnet multilayer structures, the current exerts a torque on the magnetization of magnetic layers. If the torque is large enough, the magnetization of magnetic layer switches, resulting in a change in resistance of the multilayers. In order to achieve switching, a high current density is required, typically 10^7 to $10^9 A/cm^2$. Two general experimental approaches have been used to direct current flow through small areas in the magnetic multilayers to achieve high densities. One approach is a point-contact geometry made by using a very sharp tip or using lithography techniques. The other was to make nanopillar devices by electron beam lithography (20).

Myers *et al.* (21) measured STT switching in magnetic multilayer devices of Co/Cu/Co fabricated by evaporation in high vacuum chamber. To achieve sufficiently high current density, electron-beam lithography and reactive ion etching were used to produce a bowl-shaped conductive point in an insulator layer. They mentioned magnetic switching happens when the switching current density was over a threshold.

Tsoi *et al.* (22) measured STT switching in magnetic multilayer devices using mechanical point contact to a metallic multilayer. (Cu/Co)n multilayers were prepared by sputtering with n ranging from 20-50 with layer thickness t_{Co}=1.5 nm and t_{Cu}=2.0-2.2 nm. Current densities as high as 10^9 A/cm^2 were injected into the multilayers to switch the magnetization of the Co layers. Seki *et al.* (23) investigated the effect of STT switching in 90^o magnetization configurations with current-induced magnetization reversal in thin film of metallic FePt/Au/FePt pillars to solve these two problems. The magnetization of one of the FePt layers (polarizer) was perpendicular to the plane. It was found that the magnitude of the switching current density was reduced to around 10^7 A/cm^2.

Since 1995, people started investigating STT switching in TMR structures. Al_2O_3 was used as the barrier layer in most of the early studies. With the development of thin film technology, MgO barrier layers were used as the barrier layer for the application of STT switching. STT switching in tunnel junctions have great potential in STT devices. Hayakawa *et al*. (24) studied current-driven magnetization switching in CoFeB/MgO/CoFeB magnetic tunnel junctions, which were fabricated by electron-beam lithography and magnetron sputtering. After annealing at 270 and 300 C^o, the switching current density was 10^5 A/cm^2.

A summary of GMR, TMR, and STT switching for thin film samples is shown in Table 1.1.

Table 1.1. Summary of GMR, TMR, and STT switching of thin film samples

	Depostion Methode	Material	Thickness of Layers (nm)	MR	Ic (A/cm^2)	References
GMR	**MBE**	**Fe/Cr**	**Fe: 3, Cr: 0.9, 1.2, 1.8**	**70% at 4.2K**		(1)
	Sputtering	**Fe/Cr**	**Fe: 2, Cr: 5**	**6.50%**		(2)
	Sputtering	**Co/Cu**	**Co: 1.5 Cu: 0.9**	**78% at 2K, 45% at 300K**		(3)
	Sputtering	**Co, Ni, NiFe/Cu, Ag, Au**	**supper lattice**	**8.70%**		(6)
	Sputtering	**NiFe/Cu/Co**	**NiFe: 3, Cu: 5, Co:3**	**14%**		(7)
	Sputtering	**CoFe/Cu/CoFe**	**CoFe: 3, Cu: x CoFe: 1**	**6%**		(13)
TMR	**Sputtering**	**Fe/GeO/Co**	**GeO: 10**	**14%**		(14)
	Sputtering	**Fe/Al_2O_3/Fe**	**Fe: 100, Al_2O_3: 5.5, Fe: 100**	**18%**		(15)
	Sputtering	**CoFe/MgO/CoFe**	**CoFe: 0.8, MgO: 2.9, CoFe: 2.9**	**200%**		(16)
	Sputtering	**CoFeB/MgO/CoFeB**	**CoFeB: 3, MgO: 1.8, CoFeB: 3**	**230%**		(17)
STT switching	**Eveporation, e-beam lithography**	**Co/Cu/Co**	**Co: 2, Cu: 4, Co: 100**		**2 mA**	(21)
	Sputtering	**Co/Cu**	**Co: 1.5 Cu: from 2 to 2.2**		**10^9**	(22)
	Sputtering	**FePt/Au/FePt**	**FePt: 20, Au: 5, FePt: 1.5**		**10^7**	(23)
	Sputtering	**CoFeB/MgO/CoFeB**	**CoFeB: 2, MgO: 0.85**		**10^5**	(24)

1.2 Electrochemically Deposited Magnetic Nanowires

Electrochemically deposited magnetic nanowires have attracted research interest due to their small dimensionalities. They show potential applications as magnetic recording media, magnetic reader, and magnetic random access memory (MRAM). Electrochemical deposition is a cost-effective and simple method to grow nanowires with high aspect ratio. Many types of magnetic nanowires can be fabricated by this method.

1.2.1 Template Fabrication

Electrochemical deposition has been used to grow magnetic nanowires in nanoporous templates including track-etched polycarbonate membranes, anodic aluminum oxide, and diblock co-polymembranes (25) (26) (27) (28) (29) (30). Before this thesis work (31), the smallest magnetic-multilayered nanowires (30 nm diameters) had been achieved using track-etched polycarbonate templates (27) (32). These membranes have the advantage of large interpore spacing so that single wires have been easily contacted during fundamental studies. However, they will not be ideal for eventual applications that require either high densities or very insulating surroundings, such as magnetoresistive random access memory (MRAM) and recording heads. On the other hand, nanoporous anodic aluminum oxide (AAO) templates have closely spaced pores in an insulating matrix. Compared to polycarbonate membranes, AAO membranes present many advantages with respect to thermal stability, mechanical resistance, and oxidation protection for electrodeposited magnetic materials. Furthermore, adjustment of pore density and diameter as well as nanopore ordering is possible with AAO. In recent years, AAO has become a popular template system for the synthesis of various functional nanostructures. The majority of current perpendicular to plane giant magnetoresistance (CPP-GMR) studies involving AAO has used commercial templates where varying diameters and branching structures can result in misleading magnetic information unless the structure is known and accounted for (33).

Masuda *et al*. (34) (35) developed a two-step anodization method which can be used to grow AAO templates with very uniform diameters and straight nanopores. Lee *et al*. (36) summarized the relationship between the diameter of the nanopores and anodization conditions, such as, temperature, applied voltage, and acid (as shown in Fig. 1.1). Three growth regimes were obtained. In the first regime, below 40 V, nanopores with diameters from 25 nm to 70 nm were grown in sulfuric acid (H_2SO_4). In the second regime, nanopores with diameters from 50 nm to 150 nm were grown in oxalic acid ($H_2C_2O_4$). In the third regime, above 160V, nanopores with diameters from 200 nm to 250 nm were grown in phosphoric acid (H_3PO_4). The smallest nanopores (25 nm diameter) made in AAO before this work were made using 19 V in sulfuric acid (32). A few CPP-GMR studies have used homemade AAO with the smallest nanopores being 40-60 nm in diameter (37) (38). The effects of anodization voltage and the concentration of the electrolyte on the current density and AAO structure were also studied by Zhao *et al.* (39). It was found that the current density was exponentially dependent on anodization voltage and the relation between the electrolyte concentration and the diameter of AAO was linear. Since then, AAO templates have been widely used to fabricate nano-size materials due to the advantages of AAO templates. Nanopores in AAO template are columnar, very uniform in diameter along each pore and monodisperse, and parallel to each other. The diameters of the nanopores can be adjusted from a few nanometers to several hundred nanometers by varying the anodization conditions, such as, acid,

concentration, voltage, and temperature. (34) (35) Very large area (> 1 cm^2) AAO with very high nanopore density (> $2.5*10^{12}$ holes/m^2) and high aspect ratio (> $1.7*10^3$) can be inexpensively and reliably fabricated. AAO is thermally stability and has very good mechanical resistance. The materials deposited in AAO can be prevented from oxidizing. AAO is one of most prominent templates for synthesis of nanowires and nanotubes with controllable diameter and high aspect ratio.

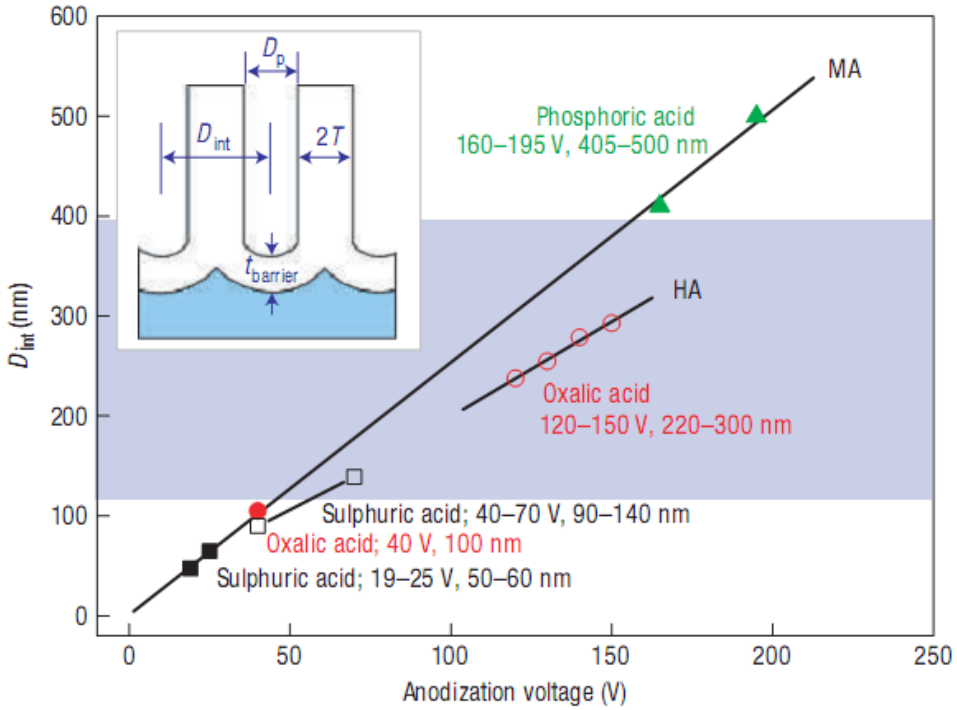

Fig. 1.1.The relation between the diameter of the nanopores in AAO templates and various anodization conditions (36).

However, the two-step anodization method has limitations in that the nanopore arrays do not have long range order (grains less than 1um only). In order to solve this

problem, nano-imprinting methods have been introduced by our group, Masuda and Goesele (40) (41) (42). After nano-imprinting with master stamps that have long range order, nanopore arrays with large domains of perfect order have been achieved, and these will be useful for future devices. Choi *et al.* combined nano-imprint lithography and anodization to prepare AAO template with 50 nm diameter pores and different spacing from 50 nm to 500 nm (43).

Short nanowires have potential applications as sensors. In order to grow short nanowires, it is important to develop thinner AAO templates. Xu *et al.* (44) developed a method to make thinner AAO templates. In their method, 3 μm thick Al was deposited by sputtering on p-type, Ti-coated silicon substrates. After two-step anodization, very thin (< 1μm) AAO templates were successfully formed on the Si substrate. After the metal film was fully anodized, the anodization process was continued for 90-120 min to remove the barrier layer at the bottom of the pores, shown in Fig.1. The Ti film was used as the electrode for electroplating nanowires into the nanopores. The diameter of these nanopores still depended on the anodization conditions, but this dependence varied from bulk anodization. Also, the Ti electrode can be destroyed by the barrier layer removal, so care must be taken. Zou *et al.* from our group (45) combined nano-imprinting and thin film anodization together to fabricate very uniform 500 nm thick templates with 163 nm pores and center to center distances of 400 nm.

Other methods were used to fabricate nanoporous templates. Peng *et al.* (46) used focused ion beam (FIB) to pattern polished Al foil in order to obtain long range order. Then, the patterned Al was anodized to form ideally ordered nanopores. The smallest nanopore they achieved was close to 10 nm. But, this method was limited by the working environments (for example, vacuum chamber), the sample area, and the higher cost. Nanoporous templates also have been made by electron beam lithography (EBL) (47). In these methods, photoresist polymethylmethacrylate (PMMA) has been coated on Si substrates. Then, perfectly ordered and very uniform PMMA nanoporous templates (nanopore size > 20 nm) were fabricated in one-step process of EBL on Si substrates. However, EBL is a very expensive and slow process which limits its broad application. Meanwhile, the requirements of the fabrication conditions (such as, high vacuum, clean room) and the equipment are extremely strict in order to acquire the smallest structure.

1.2.2 Magnetic Nanowires

Many magnetic single-element and alloy nanowires (for example, Co, Ni, Fe, FeNi, CoCu, CoPt, CoPd) have been studied not only for fundamental studies, but also for potential application, such as, magnetic recording media, sensors, and other devices (48) (49). These nanowires have been deposited into nanoporous templates by electrochemical deposition methods. The diameters of the nanowires are determined by the nanoporous templates because the wire growth is confined by nanopores.

Han *et al.* (50) have studied magnetization reversal mechanisms of single material nanowires (Ni, Co, NiFe, and CoPt) in AAO and polycarbonate template with pore size of 30 nm, 50 nm, and 80 nm. It was summarized that the magnetization reversal mechanisms determined the coercivity (Hc) of the nanowires. Magnetostatic interaction among wires reduced Hc and remnant squareness (S). Strong magnetostatic coupling among nanowires not only suppressed Hc and S significantly, but also induced a change in the magnetization reversal mechanisms. Overall, the easy axis changed from parallel to perpendicular to the wire axis. Melle *et al.* (51) have mentioned the existence of quantum tunneling effects in the magnetization reversal of 45 nm diameter Ni nanowires. It would be interesting to study problems of magnetic configuration and magnetization reversal in nanowires with diameters of 10 nm where the quantum effects would appear more clearly. The magneto-optical properties of Ni in AAO templates have also been studied by Melle *et al.*. Ni nanowires showed a strong increase of magneto-optical activity compared with Ni bulk material due to the high optical anisotropy of Ni nanowire arrays.

The magnetic properties of alloy nanowires vary with the composition changes. $Fe_{1-x}Ni_x$ nanowires with 50 nm diameters have been investigated by Liu (52). The magnetic properties of nanowires were related to a variation of Ni content in $Fe_{1-x}Ni_x$ nanowires because the crystal structure of the nanowires also changed. $Co_{1-x}Pt_x$ nanowires were investigated in Zhang (53). When the Pt content ranged from 9 to 86%, the crystal structure of the $Co_{1-x}Pt_x$ nanowires changed from hcp to a mixture of

hcp and fcc phases and finally to pure fcc. The change of crystal structure led to changes in Hc and Ms. The major axis coercivity was 1780 Oe at $Co_{0.5}Pt_{0.5}$, then was 1550 Oe for a composition of $Co_{0.33}Pt_{0.67}$. The Ms value decreased from 1273 to 29 emu/cc as the Pt content increased from 9 to 86%. Single nanowires can be considered infinite cylinders, therefore the easy axes of the $Co_{1-x}Pt_x$ nanowires were decided by a combination of magnetocrystalline anisotropy and shape anisotropy (πMs^2) which varied with the composition.

CoCu alloy nanowires in commercial AAO with 20 nm diameter nanopores have been investigated by Schwarzache *et al.* (54). The coercivity of the CoCu nanowires decreased when annealing temperatures and pressure increased because larger Co rich particles were generated due to phase separation after annealing. Fedosyuk *et al.* (55) have mentioned 1 % GMR measured in CoCu alloy nanowires in commercial AAO templates with 20 nm diameter nanopores. Blythe *et al.* (56) have found Co-rich clusters in 20 nm diameter CoCu nanowires compared with thin films of similar composition which affected the magnetic properties of CoCu nanowires.

The magnetic properties of Co, Ni and Fe nanowires as a function of nanowire diameter ranging from 30 nm to 500 nm have been investigated by Piraux's group (57). It was reported that the coercivity of these magnetic nanowires decreased when nanowire diameter increased. It was believed to be due to multi-domain splitting when the diameter increased. Garcia has pointed out that a multi-domain structure is energetically favorable in Co nanowires when the diameter is larger than 35 nm (58).

Pirota (59) found that the magnetic properties of nanowires were determined by the geometrical arrangement of nanowire arrays and the magnetic nature of single nanowires. Meanwhile, Piraux has also concluded that the magnetic properties of Fe and Ni nanowires are governed by the shape anisotropy. However, in the case of Co nanowires, there was a competition between shape anisotropy and magnetocrystalline anisotropy due to a large crystalline anisotropy in hcp Co, 5×10^6 erg/cm^3 compared to shape anisotropy $\pi Ms^2 = 5\times10^6$ erg/cm^3 at room temperature. This competition led to unique magnetic behaviors and undesired hysteresis loops with much reduced squareness ratios in Co nanowires. Therefore, tailoring the Co c-axis alignment was very important. The remnant magnetization of Co nanowires was enhanced by aligning the Co c-axis along the nanowires, but it decreased when the c-axis was perpendicular to the nanowires.

Several methods have been developed to control crystallographic orientation in Co nanowires. In particular, the pH of the electrolyte has been the most widely used parameter (60). It has been concluded that c-axes prefer to align along the nanowire axes when the wires are grown at high pH (> 5.8), but at low pH (3.8 – 4.0), the nanowires prefer to have an in-plane c-axes (61) (62). The effect of external magnetic fields is the second most studied parameter affecting the Co crystal structure. Ge's group found that the Co c-axis followed the external magnetic field direction when the fields were larger than 450 Oe during Co nanowire growth (63). Co nanowires preferred to have c-axes out-of-plane when the magnetic field was parallel to the

nanowires and in-plane when the magnetic field was perpendicular to the nanowires. However, Cobian found the field only had a significant effect when the bath parameters were optimized, for example without the typical additions of Lewis acids. (64) Magnetic properties of electrodeposited Co nanowires have also been controlled by other methods such as, electrolytic bath composition, deposition current density, temperature, agitation, and electrodeposition dynamics (65).

The magnetic properties of nanowires are affected by other factors besides the crystal structure. Smaller diameter Co nanowires showed large coercivity when the magnetic field direction was parallel to wire axes. However, when diameters of Co nanowires were less than 50 nm, it was possible to form single domain nanowires. As mentioned above, Garcia *et al*. (58) used magnetic force microscopy (MFM) to study Co nanowires and found that single magnetic domains were revealed in Co nanowires with 35 nm diameters. Also, strong dipolar interactions between nanowires in high density arrays contributed to the magnetic properties of the nanowires. The dipolar interactions can be represented by $H_{dipolar} \propto L/s^3$ in which L is the length of nanowires and s is the space between nanowires (66). Electroplated Ni nanowires with 180 nm diameter in AAO templates were studied by Escrig *et al*. in 2007 (67). Remanence as a function of the magnetostatic interaction in the arrays was studied by a simple magnetic phenomenological model. It was found that the remanence of nanowire arrays was strongly influenced by the size of samples due to the dipolar interactions between nanowires. MFM images were used to investigate the different

remanent states by counting the number of wires pointing in each direction. O'Barr *et al.* (68) and Lederman *et al.* (69) also used MFM to investigated single Ni nanowires with diameters from 20 nm to 500 nm. Positive and negative poles at the end of nanowires were shown on MFM images which meant single Ni nanowires had single domains with magnetization along the nanowire axes. The switching mechanism was a curling mode for large diameter nanowire (>90 nm) and a Stoner-Wohlfarth (SW) mode for smaller diameter nanowire (<60 nm).

It was found that the resistance of arrays of Co nanowires with 90 nm diameters changed when the magnetic field was applied parallel or perpendicular to the current. This change was due to a dependence of resistance on the angle between magnetization and current, called anisotropic magnetoresistance (AMR) (70). Groups in Lausanne and Louvain measured AMR on Ni and Co nanowires to be around 1% (71).

Electrodeposited multilayered nanowires are ideal for investigating CPP-GMR effects because nanowires with large aspect ratios can be easily grown. These high aspect ratio nanowires can provide much higher electrical resistance than that of thin films which make CPP-GMR measurements more accurate. Then, once a good structure has been found, lower aspect ratios of the same system can be made for lower resistance while maintaining the GMR ratios, as shown in chapter 5 below. CPP-GMR in nanowires deposited by electrodeposition has been shown to be very similar to those of conventional multilayers prepared by thin film vacuum processes.

This technique also appears to result in higher quality interfaces in structures with < 10 nm diameters because etching processes often lead to unfavorable damage of the interfaces at the sidewalls. Within months of each other, Piraux, Blondel and Liu reported the discovery of GMR in electrodeposited multilayered nanowires (26) (27) (72). Electrodeposited multilayered nanowires have since been utilized to study magnetic properties in several systems which include Co/Cu (26) (72) (37) (73) (74) (75) (76) (77), Ni/Cu (78) (79) (80), NiFe/Cu (32) (70) (81), CoNi/Cu (29) (33) (81) (82), Fe/Cu (83) , Fe/Cr (84), CoPt/Pt (85) (86), and Co/Au (83). Fig. 1.2 shows Co/Cu multilayered nanowires in a polycarbonate template with 40 nm nanopores (87).

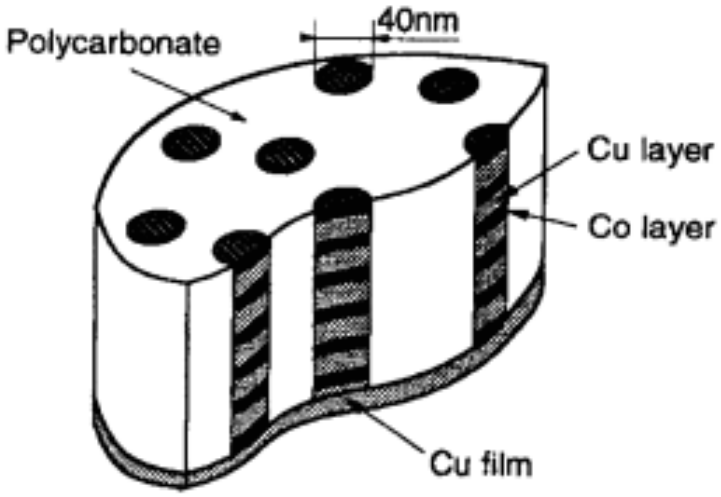

Fig. 1.2. Multilayered Co/Cu nanowire in track-etched polymer template (86)

GMR in CoNi/Cu nanowires grown by electrodeposition has been studied as a function of CoNi and Cu layers thickness (33). The GMR effect decreased with

increasing thickness of Cu layers (t_{Cu}), which was explained using the series-resistor model (88) (89) or the Valet-Fert model (90) under the long spin diffusion approximation. The saturation field decreased with increasing t_{Cu} due to the reduction of dipole interaction between neighboring CoNi nanowires. When the thickness of CoNi layers (t_{CoNi}) increased, the GMR effect first increased then decreased. After the CoNi layers were thick enough (> 510 nm), the GMR did not change with further increases in thickness. The reduced GMR changes for small t_{CoNi} might be due to discontinuities in very thin CoNi layers (< 2 nm). The decrease in GMR change with increasing t_{CoNi} was due to the spin diffusion length explained by the Valet-Fert model. Effects of dipole-dipole interactions between magnetic layers were also investigated. The dipolar coupling tended to align the magnetization of adjacent magnetic layers antiparallel to each other when magnetic layers were thin disk shapes. If the Cu layers were thin enough (< 4.5 nm), Ruderman-Kittel-Kasuya-Yosida (RKKY) type exchange in interlayer coupling should be considered (91) (92).

A change in magnetization of 20 % ($\Delta R/R$= GMR) has been observed at room temperature in electrodeposited CoNi(5 nm)/Cu(5 nm) multilayered nanowires with 1500 bilayers in track-etched polycarbonate membranes (81). GMR of 20 % at room temperature and 80 % at 4.2 k has been observed in electrodeposited NiFe(12 nm)/Cu(4 nm) multilayered nanowires in track-etched polycarbonate templates (93). Fe(8 nm)/Cu(10 nm) electrodeposited multilayered nanowires in track-etched polycarbonate templates showed 12% GMR at 5 K. (93) CoNi(5.4 nm)/Cu(2.1 nm)

multilayered nanowires in commercial AAO templates had 55% GMR at room temperature (29).

The Co/Cu system has absorbed the most interest due to intrinsic differences of reduction potentials and good matching of band structures between Co and Cu. In 1994, Piraux *et al.* (94) (59) studied Co/Cu multilayered nanowires that were electrodeposited in polycarbonate membranes with 40 nm diameter nanopores. GMR of 15% was successfully achieved in their Co (10 nm)/Cu (10 nm) systems at room temperature (Fig. 1.3).

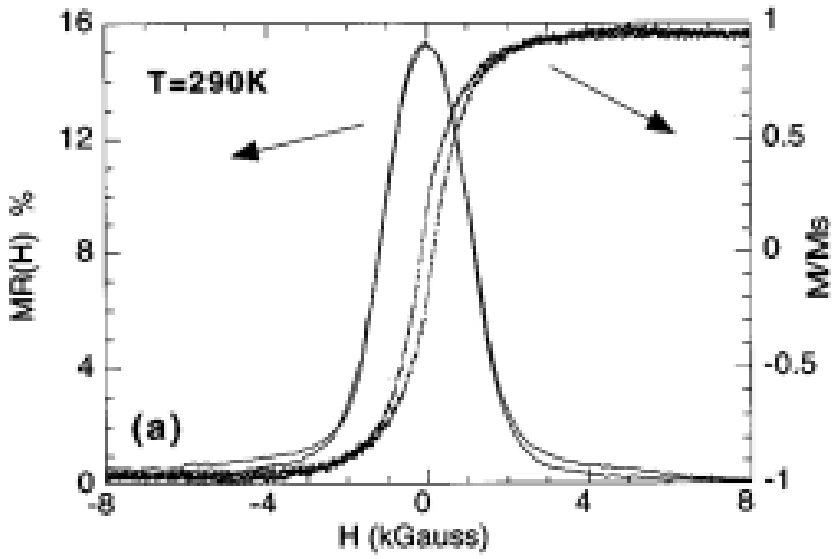

Fig. 1.3. Magnetoresistance of Co/Cu multilayered nanowires of 40 nm diameter when the applied field was parallel to films (72).

The effects of both magnetic and non-magnetic layer thickness have been investigated in multilayered Co/Cu nanowires (25) (26) (30). GMR decreased when thickness increased. Finally, GMR vanished when thickness of each layer was larger

than spin diffusion length (SDL) of each material. These results have been compared with results of Valet-Fert model (95). Interfaces and bulk spin-dependent scattering parameters and SDL in the nonmagnetic and ferromagnetic layers were extracted. SDLs of Cu and Co were 140 nm and 59 nm, respectively, at low temperature. SDL of Cu and Co in electrodeposited nanowires was about 20 nm to 30 nm at room temperature (27). Ohgai *et al.* (30) studied Co/Cu multilayered nanowires in nanopores with 60 nm diameters. The thicknesses of Cu and Co layers were adjusted to from 5 nm to 15 nm. Co/Cu multilayered nanowires reached GMR of 20% when the thicknesses of Cu and Co layers were equal to 10 nm. GMR of 50 nm diameter Co/Cu multilayered nanowires was 13% which was measured by four point measurement method (96). Blondel *et al.* (26) measured CPP-GMR of multilayered electrodeposited Co/Cu nanowires and obtained 14% GMR at room temperature. PC membranes with 80 nm nanopore diameter and 6 μm nanopore length were used as nanoporous templates. Blondel *et al.* have tested different layer thicknesses and found that a larger GMR existed for layers less than 10 nm. To obtain pure layered nanowires, Blondel *et al.* (73) have compared their results with a dual bath technique electrodeposition with ones obtained from single bath deposition. The thicknesses of each layer of Co/Cu nanowires were kept same. GMR of 8% in 10 nm layers using the dual bath technique was reported. On the other hand, GMR of 22% in 8 nm layers was obtained from single bath electrodeposition. It was concluded that impurities of Cu in Co layers, inherent in the single bath, were not the determining factor for GMR

effects. CPP-GMR of 11% in Co/Cu nanowires at room temperature and 22 % at 5 K were found by Liu *et al.* (27). The nanoporous templates used polycarbonate membranes with 30 nm nanopore diameters and 400 nm nanopore diameters, respectively. Dubois *et al.* (82) deposited Co(10 nm)/ Cu(5 nm) multilayered nanowires which showed 30 % CPP-GMR in PC membranes at 77 K. Garcia *et al.* (58) found that multilayered nanowires had transverse and oblique magnetic domains when nanowires had extreme magnetic layer thickness, such as Co (170 nm)/Cu (10 nm) and Co (25 nm)/Cu (190 nm).

Piraux *et al.* also investigated Co/Cu multilayered nanowires with 70 nm diameter. In multilayered nanowires, the aspect ratios of magnetic layers were reduced compared with homogeneous nanowires. So, shape anisotropy could no longer be treated using infinite cylinders. It was necessary to determine crystalline anisotropy and shape anisotropy precisely. Both electrolytic bath acidity and deposition potential had effects on magnetic and structural properties of homogeneous Co nanowires and multilayered Co/Cu nanowires. The C-axis of Co layers was found to be perpendicular to the nanowires axes at strong negative deposition potentials, eg: -1.2 V and was parallel at lower potentials, eg: -0.9 V, at the same pH. It was possible to control the orientation of the c-axis of multilayered Co/Cu nanowires by changing the deposition potential (97) (98).

Cho *et al.* (99) studied the effects of an external magnetic field applied during electrodeposition of multilayered Co/Cu nanowires with different diameters in

commercial AAO templates. For 50 nm diameter nanowires, their magnetic properties were affected by external fields. For 200 nm diameter nanowires, their magnetic properties were little affected by external fields. This was related with mechanism of nanowire growth in different diameter AAO templates which means the diameter of templates affected the orientation of crystals. Both Co (111) and (220) peaks appear on the 200 nm diameter nanowires. Only Co (111) peak appears for 50 nm diameter nanowires.

Tan (100) investigated the effects of Cu layer thickness on coercivity and magnetization reversal of multilayered Co/Cu nanowires with 40 nm diameter in AAO templates. The coercivity of Co/Cu nanowires decreased with increasing Cu thickness. Magnetization reversal was a combination of rotation and spin flipping as decided by Cu thickness and the angle between nanowire axis and the direction of the applied field. When the applied field was perpendicular to the nanowires axis, magnetization reversal was rotation in thinner Cu samples, but the reversal mechanism appeared to vary from rotation to flipping for thicker Cu samples. When the applied field was parallel to the nanowire axis, dominant magnetization reversal process appeared to be spin flipping for all of samples. These results were due to strong exchange coupling.

Encinas and Piraux (101) studied the effects of dipolar interactions on effective anisotropy field as a function of magnetic and nonmagnetic layer thicknesses in electrodeposited $Co_{0.96}Cu_{0.4}$/Cu multilayered nanowires with 140 nm diameter. In

order to avoid the effects of magnetocrystalline anisotropy, FCC Co was used. It was found that the effective anisotropy field decreased with reduction of $Co_{0.96}Cu_{0.4}$ layers thickness or increase of Cu spacer layers. Magnetostatic interactions between magnetic layers and their effects on the total anisotropy field were used in an analytical model. Its results agreed very well with experimental data.

$$H_{eff}^{Co/Cu} = 2\pi M_s(1-3P)\left(1-3\left|\sum_{k=0}^{j}(N_{2k}-N_{2k-1})\right|\right)$$

where *P* is the packing faction, *N* is the demagnetization factor.

Pullini *et al.* (96) used electron and ion-beam microscopes to detect structures and morphology defects of electrodeposited Co/Cu multilayered nanowires with different diameters. The most common defect was the tilt of the layers, which varied along the length of the nanowires. When the diameter of the nanowires increased, this effect was clearly observed. However, the GMR was very close to that of Co/Cu nanowires fabricated by conventional high vacuum deposition techniques which proved the electrodeposition method was a promising technique. Interfaces of electrodeposited Co/Cu multilayers have been studied on the multilayered Co/Cu films by Nallet *et al*. (102). A Fresnel technique using electron microscopy was used to measure interface width and layer roughness. It was found that the roughness of the interfaces was 0.4 ± 0.2 nm and the thickness of the inter-diffusion layers was 0.3 ± 0.2 nm. Qualities of interfaces were comparable to that of layers made by physical deposition techniques.

A summary of all of samples introduced in previous paragraphs is shown in table 1.2.

Table 1.2. Summary of electrochemical deposited nanowires

Type of nanowires	Templates	Materials	Diameter (nm)	Thickness of layers (nm)	MR	Reference
Single element and alloy nanowires	Polycarbonate	Ni, Co, NiFe, CoPt	30, 50, 80			(50)
	AAO	Ni	>10			(51)
	AAO	FiNi	50			(52)
	AAO	CoPt	14			(53)
	AAO	CoCu	20			(54)
	AAO	CoCu annealing			1%	(55)
	AAO	CoCu	20			(56)
	Track-etched polymer	Co, Ni, Fe	from 30 to 500			(70)
	Polycarbonate	Co	35			(58)
	AAO	Ni	from 20 to 500			(68), (69)
	Polycarbonate	Ni, Co	80		AMR 1%	(71)
Multilayered nanowires	AAO	CoNi/Cu	20, 250	Cu:4.2-44, CoNi:2-510	23%	(89)
	Polycarbonate	(Co, Ni)/Cu	80	Co,Ni: 5, Cu: 5	15-20%	(81)
	Polycarbonate	NiFe/Cu	90	NiFe: 1.5-12, Cu: 4-10	80% at 4.2K	(103)
	Polycarbonate	Fe/Cu	100	Fe: 8, Cu: 10	12% at 5K	(83)
	AAO	CoNi/Cu	20	CoNi: 5.4, Cu: 2.1	55% at RT, 115% at 77k	(29)
	Polycarbonate	Co/Cu	40	Co: 10, Cu: 10	15%	(94)
	Track-etched polymer	Co/Cu	30, 50, 100	Co: 4.5, Cu: 4.7	13%	(96)
	Polycarbonate	Co/Cu	80	Co: 20, Cu: 40	14%	(26)
	Polycarbonate	Co/Cu	80	Co: 10, Cu: 10	8% in dual bath, 22% in single bath	(73)
	Polycarbonate	Co/Cu	30	Co: 4.8, Cu: 3	11% at RT, 22% at 5K	(27)
	Polycarbonate	Co/Cu	100	Co: 10, Cu: 5	30% at 77K	(83)

	AAO	Co/Cu	50, 200	Co: 50, 25, Cu: 30		(99)
	AAO	Co/Cu	40	Co: 5, Cu: from 1 to 8		(100)
	Polycarbonate	Co/Cu	80, 500		10%	(104)
	Polycarbonate	CoCu/Cu	140	CoCu: from 17 to 213, Cu: 4		(101)

The discussion above pertained mostly to transport properties of arrays of multilayered nanowires, but transport in a single nanowire is also an interesting topic. In order to measure a single nanowire, Enculescu *et al*. (104) used irradiated polycarbonate membranes to prepare a single nanopore. After subsequent chemical etching, a single Co/Cu multilayered nanowire was grown into this single nanopores and a gold contact was sputtered onto the upper surface of the template. It exhibited up to 10% CPP-GMR at room temperature.

1.2.3 Spin Transfer Torque (STT) Switching

Spin transfer torque (STT switching) switching is a hot topic for spintronics currently. Because most work has been focused on nanostructures fabricated by vacuum processes, STT switching phenomena in the electrodeposited multilayered nanowires is an interesting new research direction. Fabian *et al.* studied 40 nm diameter Co(30 nm)/Cu (10 nm)/Co(10 nm) pseudo-spin-valves buried in the middle of a long Cu nanowires, produced by electrodeposition in track-etched polymer templates. The trilayer structure was obtained by a double-bath technique. The irreversible parts of hysteresis of a single Co/Cu/Co nanowire were studied. In order to contact with a single nanowire, the deposition process was monitored by checking the potential between the top and bottom surfaces of the membrane. The potential

dropped to zero when a film on the surface started to deposit. A single nanowire had grown out of templates at this time. Two-level fluctuations of the magnetization states of pseudo-spin-valve pillars were triggered by spin-polarized currents of 10^7 A/cm^2 at room temperature. (105).

A spin-transfer torque effect (STT switching) has also been studied in Co/Cu/Co trilayered nanowires electrodeposited in AAO templates (106) (107) (108). Spin transport properties of single nanowires at room temperature were investigated. For small applied magnetic fields, the resistance changed above a critical injected current because magnetic reversals were driven by a spin-polarized current. Critical current densities for the magnetization reversal were in the 10^7 A/cm^2 range as in the PC membrane wire discussed in the previous paragraph. Under large applied magnetic fields, differential resistance showed some peaks which could be explained by high frequency excitation of the free layer magnetization. Furthermore, when a high current was injected in the presence of a high magnetic field, STT switching generated a magnetization precession in the GHz range that led to microwave emission. This opened the possibility for the development of nano-sized tunable microwave oscillators.

Piraux's group studied the effects related to spin transfer torque on single and trilayered NiFe(30 nm)/Cu(10 nm)/NiFe(6 nm) nanowires with 85 nm diameter and Co(2 nm)/Cu(2 nm)/Co(25 nm) nanowires with 90 nm diameter in AAO on Si. AFM was used to make a hole to contact a single nanowire. Then, a gold electrode was

deposited into the hole as an electrode. Fig. 1.4 shows how to contact with single nanowire by this method (108). Critical current densities of NiFe/Cu/NiFe nanowires were -4.4 $\times 10^7$ A/cm^2 for parallel (P) state to antiparallel (AP) state transition and 7 $\times 10^7$ A/cm^2 for the transition from AP to P state. The critical current densities of Co/Cu/Co nanowire were -7.3 $\times 10^7$ A/cm^2 for parallel (P) state to antiparallel (AP) state transition and 2.2 $\times 10^7$ A/cm^2 for the transition from AP state to P state (Fig. 1.5) (109).

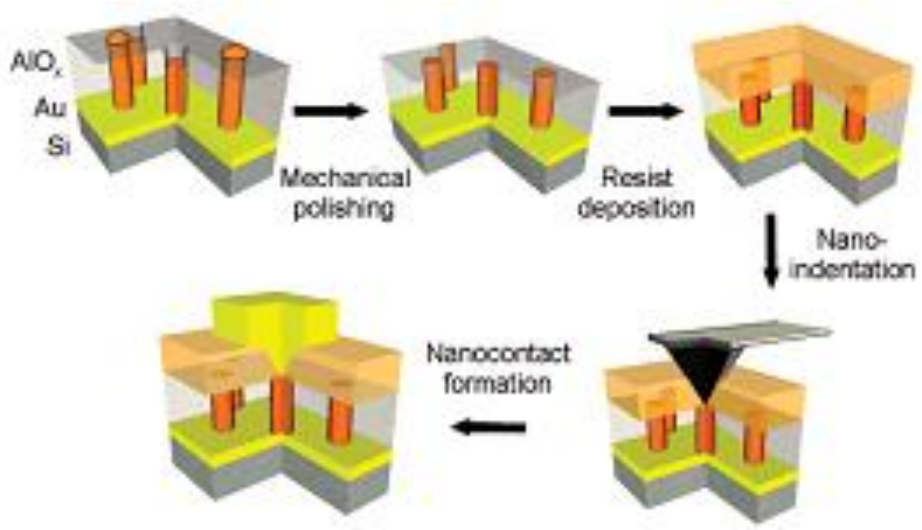

Fig. 1.4. The single nanowire contacting process using an AFM tip (108).

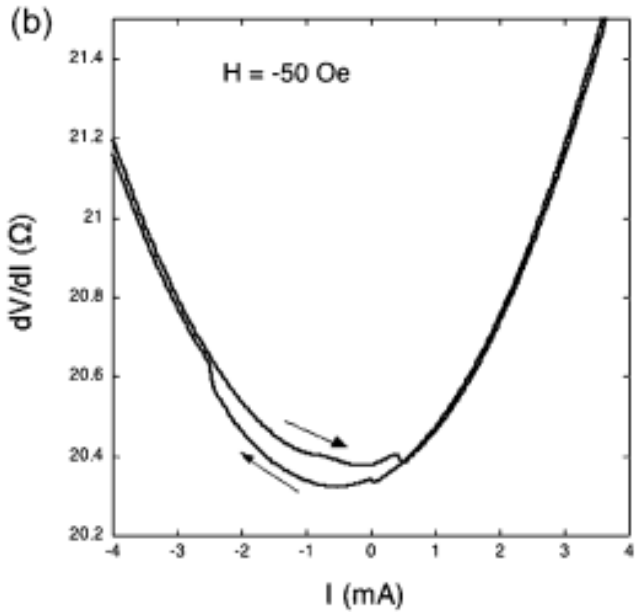

Fig. 1.5. Resistance of single NiFe/Cu/NiFe nanowire as function of bias DC current at H = - 50 Oe (109).

The effects of spin-polarized currents on magnetization states in different electrodeposited single 60 nm diameter nanowires have also been studied by Wegrowe (110). In order to understand the effect of current induced magnetization switching, three types of nanowires were prepared which included Ni nanowires, multilayered Co(10 nm)/Cu(10 nm) nanowires, and pseudo spin-valve pillars Co(30 nm)/Cu(10 nm)/Co(10 nm). It was found that two different mechanisms accounted for magnetization reversal: exchange torque and spin transfer torque.

A summary of results from all of STT switching references is shown in Table 1.3.

Table 1.3 Summary of STT switching of electrodeposited nanowires

Tempalts	Materials	Diameter(nm)	Thickness (nm)	Ic (A/cm^2)	Reference
Polycarbonate	Co/Cu/Co	40	Co: 30, Cu: 10, Co: 10	10^7	(105)
AAO	Co/Cu/Co	90	Co: 2, Cu: 2, Co: 25	10^7	(109)
AAO	NiFe/Cu/NiFe	85	NiFe: 30, Cu: 10, NiFe: 6	10^7	(108)
Polycarbonate	Co/Cu/Co	60, 80	Co: 30, Cu: 10, Co: 10	10^7	(110)

In conclusion, electrochemically deposited magnetic nanowires show potential for applications such as GMR sensors and STT devices due to their advantages. It is an inexpensive fabrication method to grow close packed nanowires. GMR of 55% was achieved on electrodeposited CoNi/Cu nanowires. It is easy to acquire the high current density for STT application because of the small areas of the nanowires (as low as $75nm^2$ which is ten times smaller than the smallest vacuum fabricated STT structure to date).

1.3 Advantages of Electrodeposited Multi-layered Nanowires to Other Sensors

In order to create diameters of ~10nm from thin film GMR and TMR structures, the fabrication processes are usually very complicated, including mask design, thin film deposition, photolithography, electron-beam lithography, and ion milling. Every step requires a special and expensive instrument. On the other hand, electrochemical deposition can be used to grown multilayered magnetic nanowires inexpensively with

very high densities and high quality. The diameter of nanowires and thickness of each layer can be accurately controlled. In addition, the crystal structure of the deposited metals can also be easily controlled by deposition conditions. GMR ratio of 20% was found in 10nm diameter electrodeposited Co/Cu multilayered nanowires at room temperature. (31) Therefore, electrodeposited magnetic nanowires show potential for applications as the next generation of reader for high areal density media due to good heat dispersion and adequate MR. The high densities of electrodeposited magnetic nanowires also mean they have great potential for future applications in MRAM. However, the switching current density of electrodeposited nanowires is around 10^7 A/cm^2 which is higher than that of thin film TMR structures. Since TMR sensors cannot be made electrochemically because they require an insulating layer, the reduction of switching current and enhancement of MR ratios will be the most important aspects of future research.

CHAPTER 2 OVERVIEW OF TECHNOLOGY

This chapter introduces how to form anodic aluminum oxide (AAO) templates for electrodeposited nanowires and what giant magnetoresistance (GMR) and spin transfer torque (STT) are in detail. Meanwhile, the material characterization methods used in this research are introduced including X-ray diffraction (XRD), vibrating samples magnetometer (VSM), atomic force microscopy (AFM), and scanning electron microscope (SEM)

2.1 Anodic Aluminum Oxide (AAO) templates

The anodization setup used in this research is shown in Fig 2.1. A polished aluminum foil and a platinum wire worked as the anode and cathode respectively. A potential between two electrodes and temperature of the electrolyte were kept constant to form uniform AAO templates.

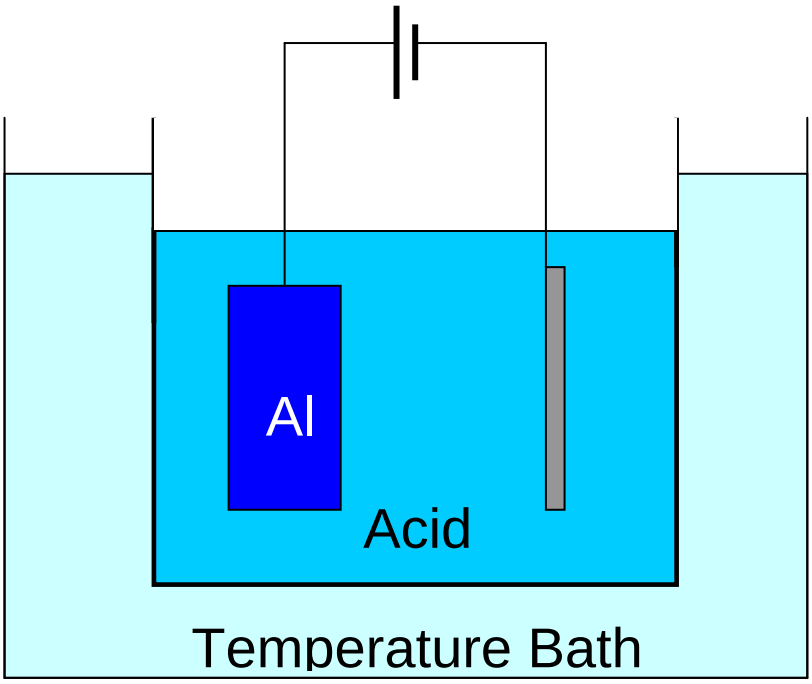

Fig 2.1 Anodization setup

A thin layer of alumina forms on the surface of a polished Al when it is anodized in the acid. During the anodization, there are two competitive processes, formation and dissolution, respectively. The following reactions occur at the metal/oxide interface:

$$Al(s) \rightarrow Al^{3+}(s) + 3e^{-}$$

Meanwhile, a water molecule is split to a hydroxyl anion and ionic hydrogen

$$H_2O \rightarrow OH^{-} + H^{+}$$

Then, Al^{3+} reacts with OH^{-} to form Al_2O_3.

$$2Al^{3+} + 3OH^{-} \rightarrow Al_2O_3 + 3H^{+}$$

A reversal reaction happens during the formation of an alumina film. The formed Al_2O_3 in the anodization process reacts with the hydrgens formed in the previous reaction.

$$Al_2O_3 + 6H^{+} \rightarrow 2Al^{3+} + 3H_2O$$

Fig. 2.2 shows the reaction at the oxide/electrolyte (o/e) interface and metal/oxide (m/o) interface. The reaction occurring at the o/e interface is electric field enhanced chemical dissolution. At the same time, the metal dissolution at the m/o interface is a charge transfer or electrochemical reaction. The key variable along the interfaces determining the reaction rate of the interface is the local electric field. (111) The distribution of the local electric field depends on the topography of the interfaces at o/e and m/o. Small topographic differences with the interfaces cause inhomogenities

in the applied electrical field which affects the different reaction rates across the interfaces.

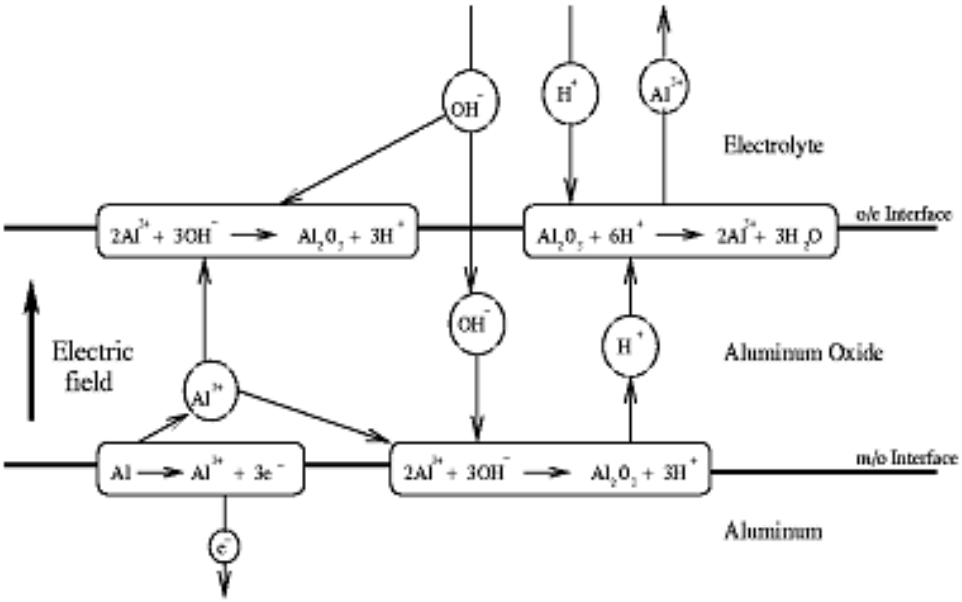

Fig. 2.2. Schematic diagram showing the electrochemical reactions and ionic paths involved during anodization of aluminum (111)

AAO growth consists of several stages as shown in Fig. 2.3 and the distribution of the applied electrical field is also shown at the different stages. First, a layer of compact oxide (barrier layer) is developed by the application of an electric field (Fig. 2.3 A). Inhomogeneities in the current distribution are caused by small topographic differences with this barrier layer. The applied electrical field at this stage is indicated by arrows in Fig. 2.3 B. This non-uniform electrical field causes a different dissolution rate of the oxide in the barrier layer, and nanopores start to form. When the electrical field and the dissolution rate in the alumina between two pores decrease, nanopores further grow (Fig. 2.3 C). As the Al continues to be anodized, the

nanopores keep growing. After a few of minutes, the nanopores within the AAO template have ordered at the m/o interface (Fig. 2.3 D). (112)

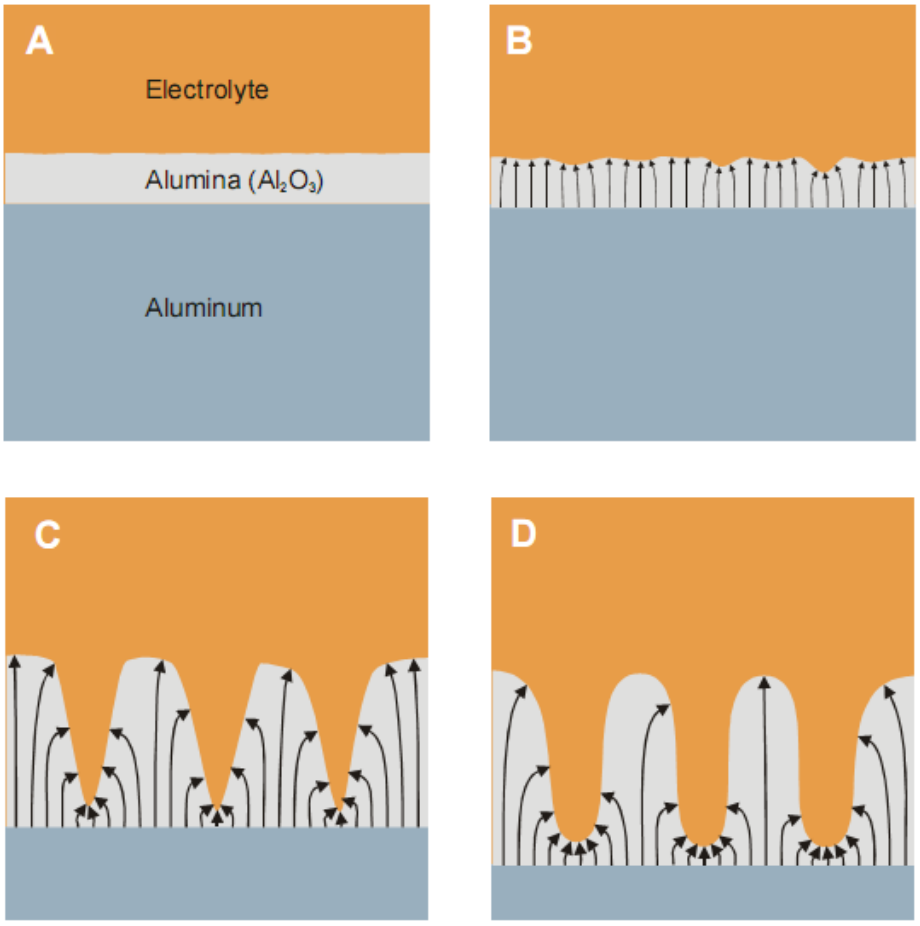

Fig. 2.3. Stages in the development of AAO during anodization (arrows correspond to locally electrical fields) (112)

The growth process can be experientially monitored by analyzing the anodization current versus anodization time as shown in Fig. 2.4 (113). Stages I, II, III in Fig. 2.4 correspond separately to stages A, B, and C (D) in Fig. 2.3. In the stage I, the current

drops dramatically because the barrier layer forms on the surface of Al. After small nanopores form in the surface of the barrier layer, the alumina at the bottom of nanopores starts to dissolve in the electrolyte. Therefore, the current slowly increases which is shown in the stage II. When the growth of nanopores achieves steady state, the anodization process is a uniform process in which the anodization current keeps constant (stage III). During the stage of steady pore growth, the anodization rate is constant. The thickness of AAO template linearly increases with the anodization time. So, the thickness of AAO can be controlled by the anodization time of the stage III.

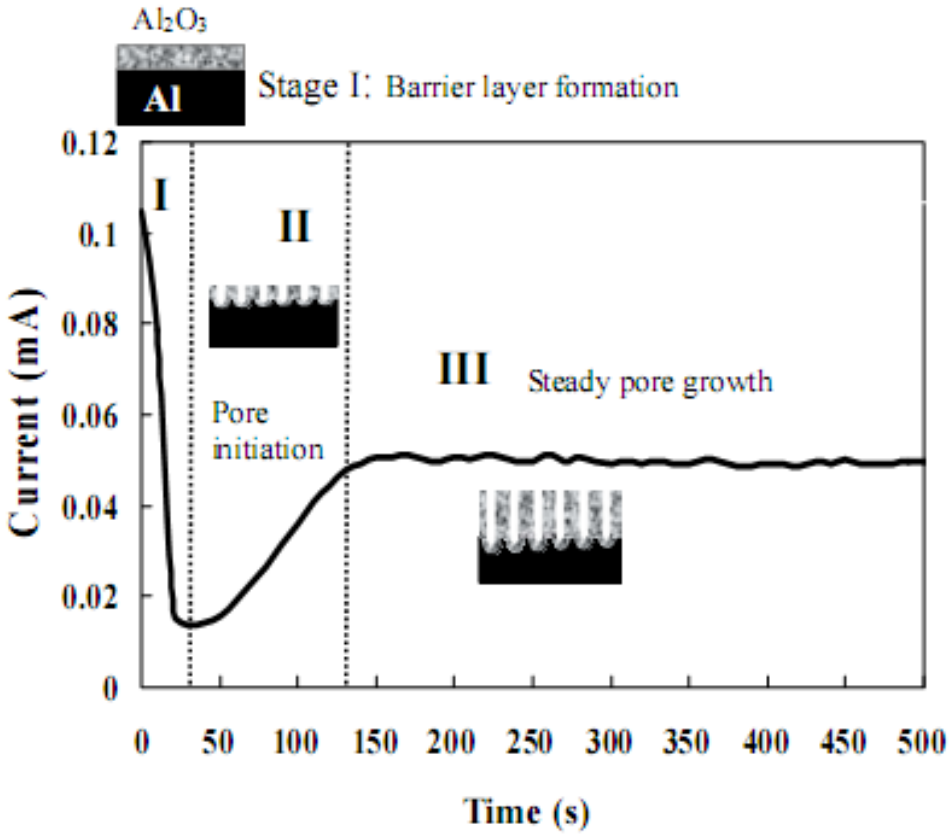

Fig. 2.4. A diagram of anodization current versus anodization time (113)

As mentioned beforehand, the nanopores thickness is linearly related with the anodization time. However it is necessary to emphasize that both the oxidation and dissolution rates of the alumina are completely different at different anodization conditions, such as temperature, electrolyte, concentration of electrolyte, and voltage.

The interpore distance (D_{int}) is linearly proportional to the applied potential with a proportionality constant (k (nm/V), $2.5 < k < 2.8$).

$$D_{int} = kV$$

The thickness of the barrier layer (D_B) is half of the interpore distance. (114)

$$D_B = D_{int}/2$$

If the aluminum used for anodization has impurities, the defects will form around impurity area since impurities have different volume expansion coefficients as the aluminum. Therefore, in order to obtain self-ordered AAO, it is very critical to use aluminum with a high purity (> 99.999%). Aluminum is easily oxidized at the ambient condition, so before the anodization process, the oxidized layer on the surface of aluminum must be removed. Then, the electrochemical-polishing process is applied to improve the smoothness of the aluminum surface.

Temperature is another key factor for the formation of AAO since the oxidation and dissolution rate of alumina depend on temperature. With all the other parameters

maintained at constant, the current density increases as the temperature increases. The increased current density doesn't increase the anodization rate because the dissolution rate of alumina at the interface between the electrolyte and oxide increases as well. At a high temperature, the dissolution rate is faster than the rate of oxide formation. Therefore, AAO can't form on the surface of Al. Meanwhile, local heating at the working surface can cause an inhomogeneous electric field distribution at the bottom of nanopores which leads to local electrical breakdown of the alumina (Fig. 2.5). But if the temperature is too low, the electrolyte may freeze. Therefore, optimized temperature needs to be used for each different electrolyte. For example, anodization is performed at 40 V in oxalic acid at 5 ~ 18 ^{o}C or at 195 V in phosphoric acid at 0 ~ 2 ^{o}C. A magnetic stirrer is used to avoid temperature gradients in the electrolyte. Another reason to use the stirrer is to effectively remove hydrogen bubbles and local heat on the surface of the aluminum electrode to allow a homogenous diffusion of anions into pore channels. It is worth mentioning that the growth rate of porous alumina is affected by the temperature. The growth rate is low if the anodization temperature is low.

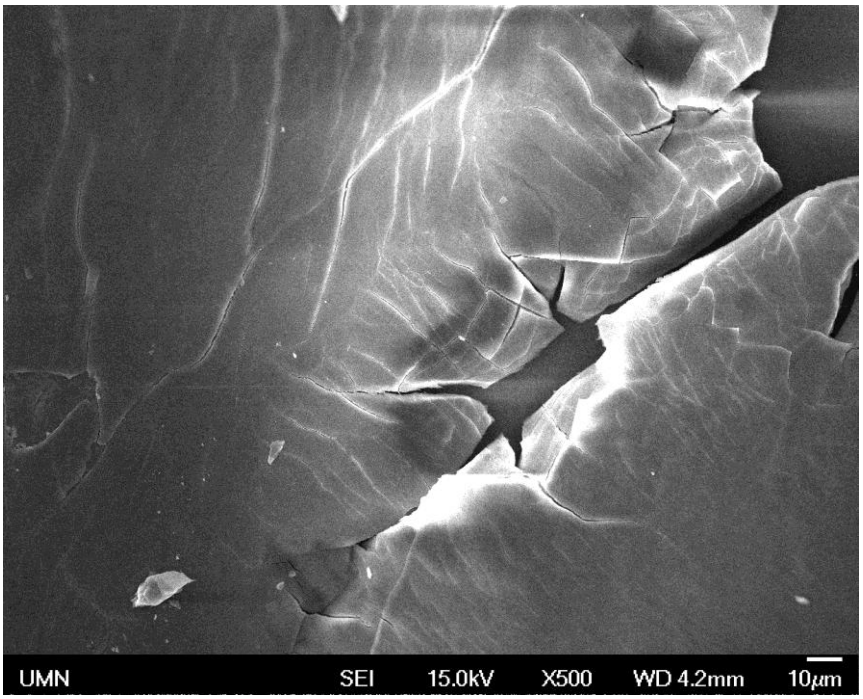

Fig. 2.5. SEM image of AAO after electrical breakdown

The thickness of alumina increases linearly with anodization time, but the current efficiency and porosity don't usually vary with time or the alumina thickness. This indicates that the current density is constant during the anodization procedure. Therefore the resistance of entire film is constant as the porous oxide grows. Anodization procedure is a slow process. Table 2.1 shows an anodization rate of aluminum in different electrolytes (115). In order to achieve highly ordered AAO templates, long anodization time is normally required (72). While the thickness of a barrier layer at the bottom of the AAO still keeps constant at the same anodization conditions.

Table 2.1. Anodizing rate of Al in different electrolytes

	Electrolyte Concentration (at 27 ^{0}C)	Anodization Rate (Å/S)
1	15 % sulfuric acid	10.0
2	2 % oxalic acid	11.8
3	4 % phosphoric acid	11.9
4	3 % chromic acid	12.5

2.2 Giant Magnetoresistance (GMR)

2.2.1 GMR effect

Multilayered nanowires are ideal structures to study the CPP-GMR. Electrodeposited magnetic multilayered nanowires have gained a great deal of interest since Piraux measured GMR of 15% on Co/Cu electrodeposited multilayered nanowires in 1994. (72) Electrodeposition offers many advantages over the conventional deposition methods. First, it is easy to reach the micro range of the thickness of each layer without affecting the quality of the interface. Meanwhile, electrodeposition can be used to grow multilayered structures with high aspect ratio. The high aspect ratio leads to large signals and precise measurements. Second, electrodeposited nanowires are ideal structures for achieving high injection current densities due to their small size. The spin accumulation effects generated by the high injection current can generate magnetic excitations and reverse the magnetization of magnetic layers. Such effects are named a spin transfer torque (STT switching) which shows the potential application as the next generation of storage memory called Magnetoresistive Random Access Memory (STT-MRAM).

The resistance of GMR structures depends on the relative orientation of the magnetization in each magnetic layer. There are two stable states (Fig. 2.6), parallel state (P) and anti-parallel state (AP). When magnetizations of all magnetic layers are parallel to each other, called parallel state, GMR structures show a low resistance. When magnetizations of all magnetic layers are anti-parallel, called anti-parallel state, GMR structures have a high resistance.

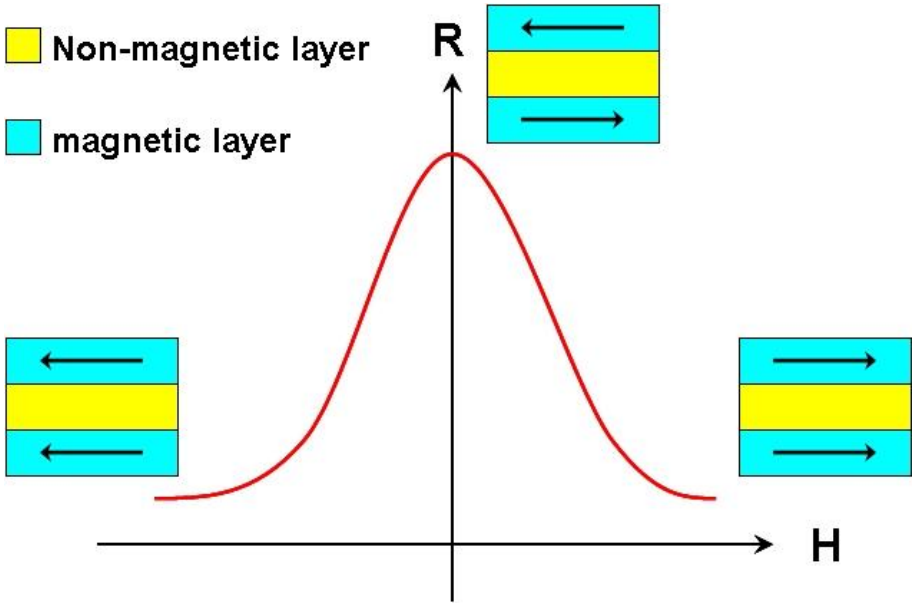

Fig. 2.6. R vs. H of GMR

The magnitude of the GMR effect is defined by:

$$GMR = \frac{\rho_{ap} - \rho_p}{\rho_p} = \frac{\sigma_p}{\sigma_{ap}} - 1$$

where ρ_P and ρ_{AP} are the resistivity for a P and AP states, respectively, σ_P and σ_{AP} are the corresponding specific conductance.

2.2.2 Theoretical model of giant magnetoresistance (GMR)

The conductivity of metals is proportional to the density of state (DOS) at the Fermi level ($D(E_F)$). Band structures determine transport behaviors of metals. The electrons have two spin angular momentums (spin-up and spin-down) which are called majority electrons and minority electrons respectively. Fig. 2.7 shows the DOS

of Fe, Co, Ni, and Cu. The number of spin-up and spin-down electrons are same for non-magnetic metal (for example, Cu). On the other hand, for ferromagnetic materials (e.g. Fe, Co, and Ni), band structures are not symmetric due to exchange interactions between magnetic ions. Since the numbers of electrons of spin-up and spin-down are not same, it causes two different DOS at the Fermi level ($D_{\downarrow}$ (E_F) and $D_{\uparrow}$ (E_F)) and different spin sub-band conductance ($g_{\downarrow}$ and $g_{\uparrow}$).

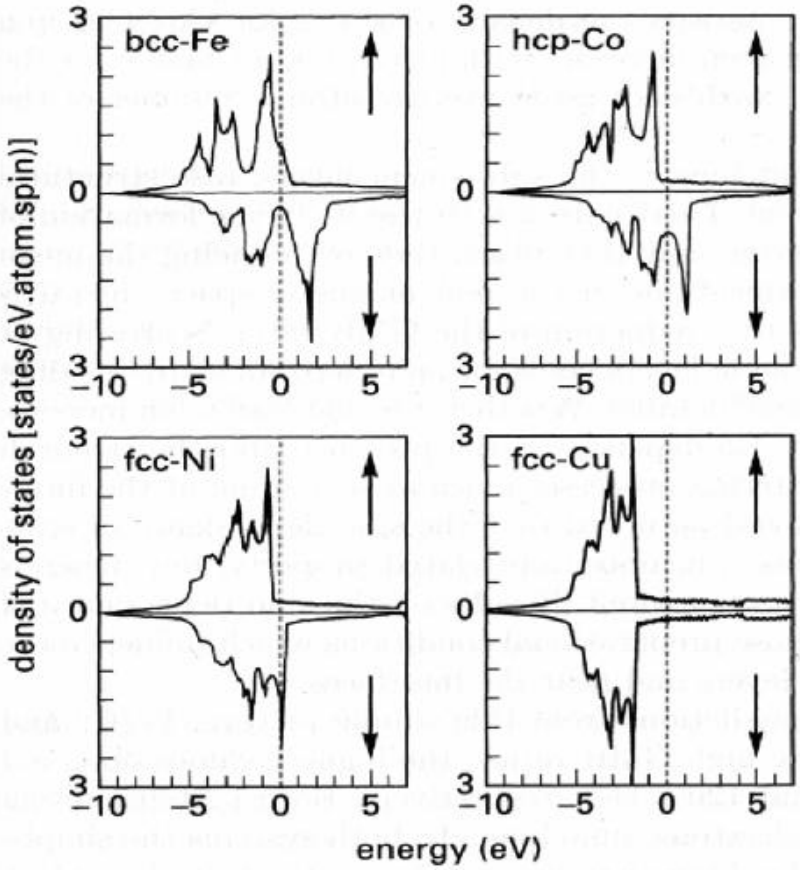

Fig. 2.7. Density of state of Fe, Co, Ni, and Cu (116)

The spin polarization is defined as a ratio of the density of states of spin-up and spin-down electrons at the Fermi level.

$$P = \frac{\left(D_{\uparrow}(E_F) - D_{\downarrow}(E_F)\right)}{D_{\uparrow}(E_F) + D_{\downarrow}(E_F)}$$

For non-magnetic metal, P is equal to zero since the density of states of spin-up and spin-down electrons are equal. But for ferromagnetic materials, since the density of sate of spin-up and spin-down electros are different, P is higher than zero, but less than one.

The Mott model of two spin channels can explain the magnetoresistance effect. The resistance is different for P and AP states. For P state and AP state, the resistivity is ρ_1 and ρ_2 as shown in Fig. 2.8.

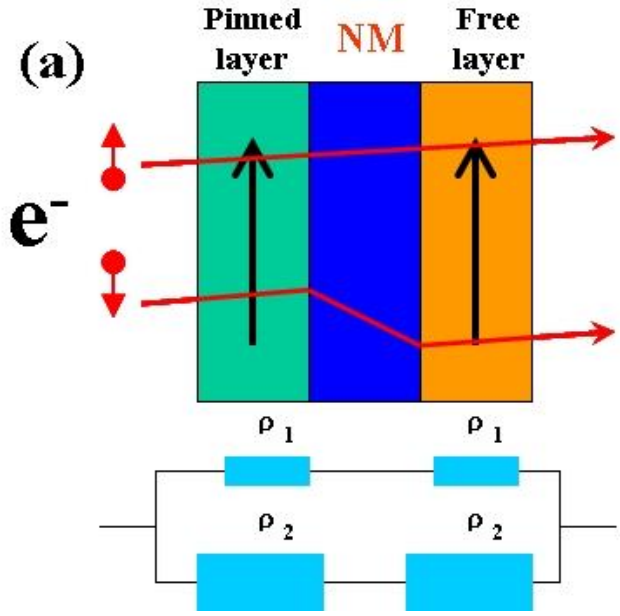

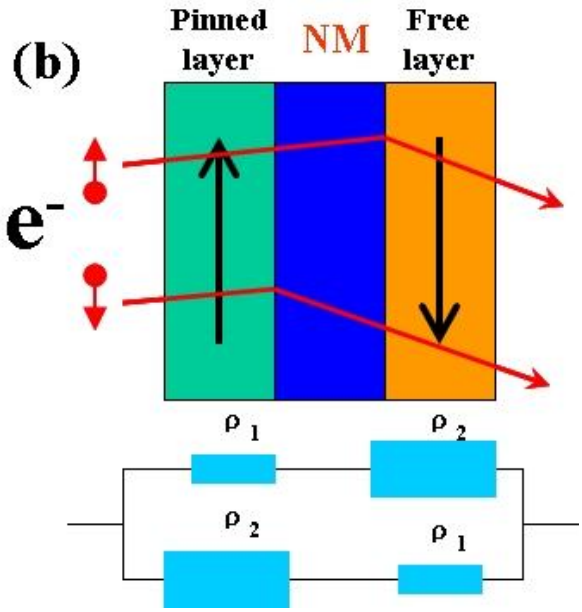

Fig. 2.8. Mott's mode of the two spin channel for the resistivity in the situation of a) parallel state; (b) antiparallel state.

If neglect the resistivity ρ of a non-magnetic interlayer, ρ_P is given by the equation:

$$\rho_P = \frac{2\rho^+\rho^-}{\rho^+ + \rho^-}$$

ρ_{AP} is given by the equation:

$$\rho_{AP} = \frac{\rho^+ + \rho^-}{2}$$

So, the magnitude of GMR amounts is given by:

$$GMR = \frac{\rho_{AP} - \rho_P}{\rho_P} = \frac{(\rho^+ - \rho^-)^2}{4\rho^+\rho^-}$$

Stoner mode is used to discuss the behavior of ferromagnetic 3d metals (Fig. 2.9). Since 4s electrons have reduced effective mass compared to 3d electrons, 4s electrons carry out the electric transport. A large DOS of 3d electrons at the Fermi energy results in an enlarged scattering of 4s electrons into empty 3d states which shows a high resistivity. The scattering probability for a parallel state of ferromagnetic layers is lower than that of an antiparallel state due to the exchange splitting of the DOS for 3d electrons. For an antiparallel state, an alternating change of the resistivity occurs for each spin channel which results in a large total resistivity. For a parallel state, the spin channel shows a low resistivity which leads to a low total resistivity. (116)

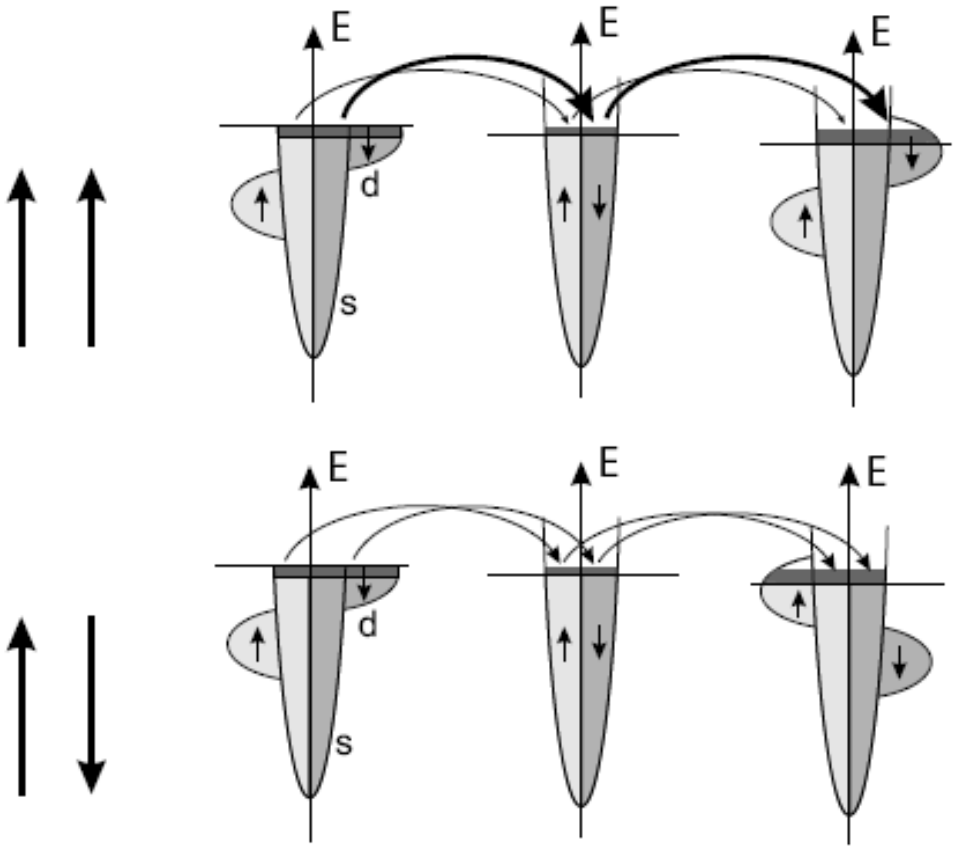

Fig. 2.9. Dependence of the resistivity on the relative orientation of the magnetization. (116)

When the resistivity of the non-magnetic interlayer is considered, assuming the non-magnetic interlayer with a cross-sectional area A and thickness d, the R_P and R_{AP} are shown by the following equations:

$$R_P = \frac{(1+\alpha\gamma)(1+b\gamma)}{2+\alpha\gamma+b\gamma} \cdot \frac{2\rho d}{A}$$

$$R_{AP} = (2+\alpha\gamma+b\gamma) \cdot \frac{\rho d}{2A}$$

$$\gamma = \frac{d_m}{d}$$

$$\alpha = \frac{\rho^+}{\rho}$$

$$b = \frac{\rho^-}{\rho}$$

where *dm* is the thickness of the magnetic layer, and

So, the magnitude of the GMR amounts to:

$$GMR = \frac{(a-b)^2}{4(a+1/\gamma)(b+1/\gamma)}$$

Valet-Fert model (Fig. 2.10) is widely used to explain CPP-GMR. The base of this model is the two-spin current model. Meanwhile, interfacial resistance is included. Interfacial resistance contributes to the spin accumulation at the interfaces between ferromagnetic layers and non-ferromagnetic layer. In this model, the resistance of a multilayer structure is expressed by the equation:

$$R^{(P,AP)} = M(r_0 + 2r_{SI}^{(P,AP)})$$

where,

$$r_0 = (1-\beta^2)\rho_F^* t_F + \rho_N^* t_N + 2(1-\gamma^2)r_b^*$$

$$r_{SI}^{(AP)} = \frac{\frac{(\beta-\gamma)^2}{\rho_N^* l_{sf}^N}\tanh\left[\frac{t_N}{2l_{sf}^N}\right] + \frac{\gamma^2}{\rho_F^* l_{sf}^F}\coth\left[\frac{t_F}{2l_{sf}^F}\right] + \frac{\beta^2}{r_b^*}}{\frac{1}{\rho_N^* l_{sf}^N}\tanh\left[\frac{t_N}{2l_{sf}^N}\right]\frac{1}{\rho_F^* l_{sf}^F}\coth\left[\frac{t_F}{2l_{sf}^F}\right] + \frac{1}{r_b^*}\left[\frac{1}{\rho_N^* l_{sf}^N}\tanh\left[\frac{t_N}{2l_{sf}^N}\right] + \frac{1}{\rho_F^* l_{sf}^F}\coth\left[\frac{t_F}{2l_{sf}^F}\right]\right]}$$

$$r_{SI}^{(p)} \frac{\frac{(\beta-\gamma)^2}{\rho_N^* l_{sf}^N}\cosh\left[\frac{t_N}{2l_{sf}^N}\right] + \frac{\gamma^2}{\rho_F^* l_{sf}^F}\coth\left[\frac{t_F}{2l_{sf}^F}\right] + \frac{\beta^2}{r_b^*}}{\frac{1}{\rho_N^* l_{sf}^N}\coth\left[\frac{t_N}{2l_{sf}^N}\right]\frac{1}{\rho_F^* l_{sf}^F}\coth\left[\frac{t_F}{2l_{sf}^F}\right] + \frac{1}{r_b^*}\left[\frac{1}{\rho_N^* l_{sf}^N}\tanh\left[\frac{t_N}{2l_{sf}^N}\right] + \frac{1}{\rho_F^* l_{sf}^F}\coth\left[\frac{t_F}{2l_{sf}^F}\right]\right]}$$

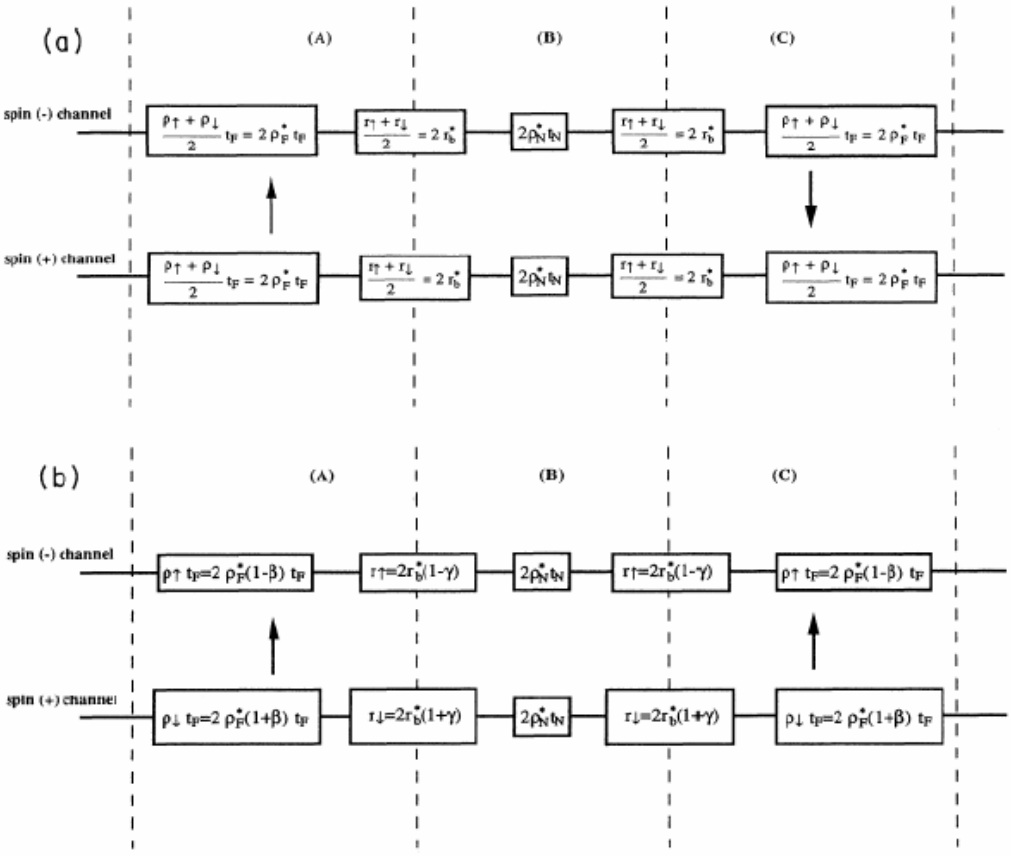

Fig. 2.10. Equivalent resistance array of V-F model (117)

l_{sf} : spin diffusion length

β : bulk spin asymmetry coefficient

γ : interfacial spin asymmetry coefficient

$\rho_{N,F}$: non-magnetic and ferromagnetic layer bulk resistivity, respectively.

$$\rho^*_{N,F} = \frac{\rho_{N,F}}{(1-\beta^2)}$$

$$r^*_{N,F} = \frac{r_b}{(1-\gamma^2)}$$

γ_b : interfacial resistance.

$t_{N,F}$: thickness of non-magnetic and magnetic layers.

Vale-Fert model can be simplified by some assumptions. If $t_{N,F} << l_{sf}$, called in the long spin diffusion limit, the resistance of a multilayer can be simplified to:

$$R^P = R^{AP} - \frac{\{\beta\rho^*_F[t_F/(t_F+t_N)]L + 2\gamma r^*_b M\}^2}{R^{AP}}$$

M: the number of bilayers, and $L = (t_N + t_F)$

When the thickness of non-magnetic layer (t_N) is much larger than its spin diffusion length (SDL), l^N_{sf} and the thickness of ferromagnetic layer (t_F) is much smaller than its SDL, l^F_{sf}. MR of multilayer decreases as $e^{(-t_N/l^N_{sf})}$.

When $t_F >> l^F_{sf}$ and $t_N << l^N_{sf}$, MR is expressed as:

$$\frac{(R^{AP}-R^P)}{R^P} = \frac{2p\beta l^F_{sf}}{(1-\beta^2)t_F}$$

where, *p* is the proportion of antiparallel configurations between the neighbor layers. If p is equal to 1, it represents a perfect configuration.

2.3 Spin transfer torque (STT) switching

Since Slonczewski predicted current-induced magnetization switching (CIMS) in 1996 (118), spin transfer torque (STT) switching has been observed in many different measurements. Most of researchers investigated these phenomena using magnetic nanopillars with pseudo-spin-valve structures. Spin-valve structure devices have normally three layers. Two ferromagnetic layers are on the both sides of a layer of non-magnetic layer, which is very similar as a basic GMR structure. But the difference from the GMR structure is that magnetization of one of two ferromagnetic layers is very hard to switch, called pinned layer. It is pinned by for example, exchange coupling, thickness. Magnetization of the other ferromagnetic layer is very easy to switch, which is called free layer.

When electrons pass through these trilayer structures, spin-polarized electrons apply a torque on the magnetization of free layer. The torque increases with increasing the current density. As the torque is large enough, it can switch the magnetization of the free layer. This torque is called spin transfer torque. The material systems mostly studied are Co/Cu systems which include thin film stacks made by vacuum processes (119) (120) and electrodeposited nanowires (108) (121) (31). In order to achieve a higher current density, the thin film stacks not only need very complicated vacuum systems to deposit spin valve structures, but also have to be

pattered to nanopillars by e-beam lithography which is a slow and costly process. Compared with the thin film structures, electrodeposited nanowires show many advantages, such as low cost, easy process, and high efficiency. Recently spin valve structure electrodeposited nanowires retain many interest from industries and academia because they show higher potential applications than giant magnetoresistance (GMR) sensors, (122) magnetic random access memory (MRAM), and recording heads of ultra-high areal density medias. Spin transfer torque can be predicted as following equation.

$$\tau_{1,2} \propto I\hat{S}_{1,2} \times (\hat{S}_1 \times \hat{S}_2)$$

where I is the current and $\hat{S}_1$ and $\hat{S}_2$ are unit vectors of a local magnetic moments of each ferromagnetic layer.

The spin transfer torque is proportional to the current density. $\hat{S}_1$ and $\hat{S}_2$ are natural properties of two ferromagnetic layers. In two ferromagnetic layers, one is thicker than the other. The moment of the thicker layer and thinner layer is $\hat{S}_2$ and $\hat{S}_1$, respectively. Fig. 2.11 shows how electrons switch the magnetization of free layer. When electrons flow from $\hat{S}_2$ to $\hat{S}_1$, they are polarized by $\hat{S}_2$. The spin transfer torque will turn $\hat{S}_1$ toward $\hat{S}_2$. When electrons flow from $\hat{S}_1$ to $\hat{S}_2$, electrons reflected by $\hat{S}_2$ apply STT on $\hat{S}_1$ which turns $\hat{S}_1$ away from $\hat{S}_2$. So, two states, parallel state and antiparallel state, can be achieved separately by changing the current direction when the current density is higher than threshold value.

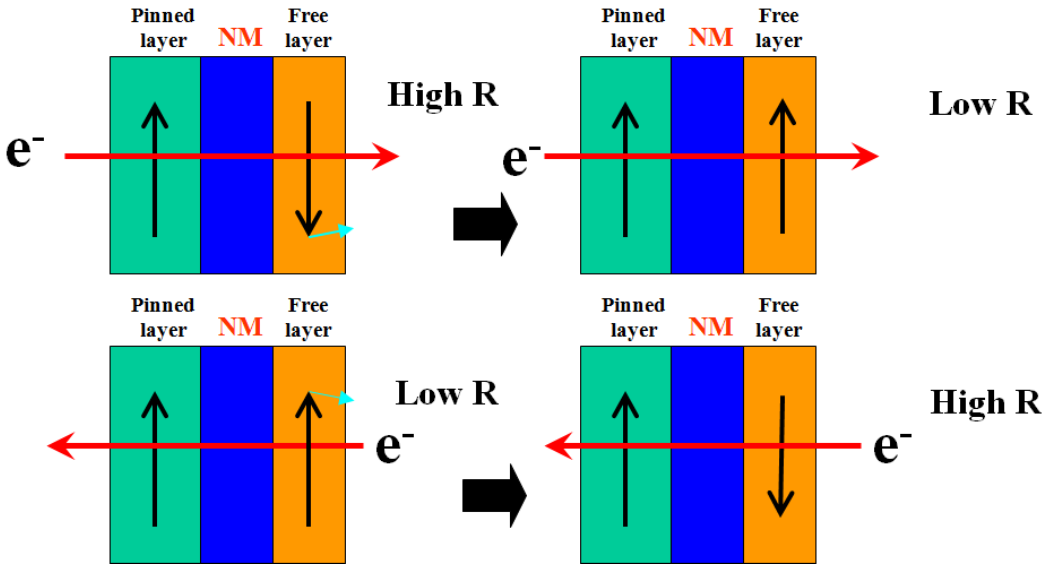

Fig. 2.11. STT switching

Fig. 2.12 shows a STT switching transfer curve. The current induced the free layer magnetization switching when the current achieved threshold. The switching critical current can be calculated by two equations.

$$I_c^+ = \alpha eMAt[H + H_{an} + 2\pi M]/hg(0)$$

$$I_c^- = \alpha eMAt[H - H_{an} - 2\pi M]/hg(\pi)$$

where, α is the phenomenological Gilbert damping parameter, M is the magnetization of the free layer, H_{an} is the anisotropy filed, A is the area of free layer, t is the thickness of the free layer, g(0) and g(π) are the efficiency of spin-transfer switching for parallel state (0) and antiparallel state (π), respectively.

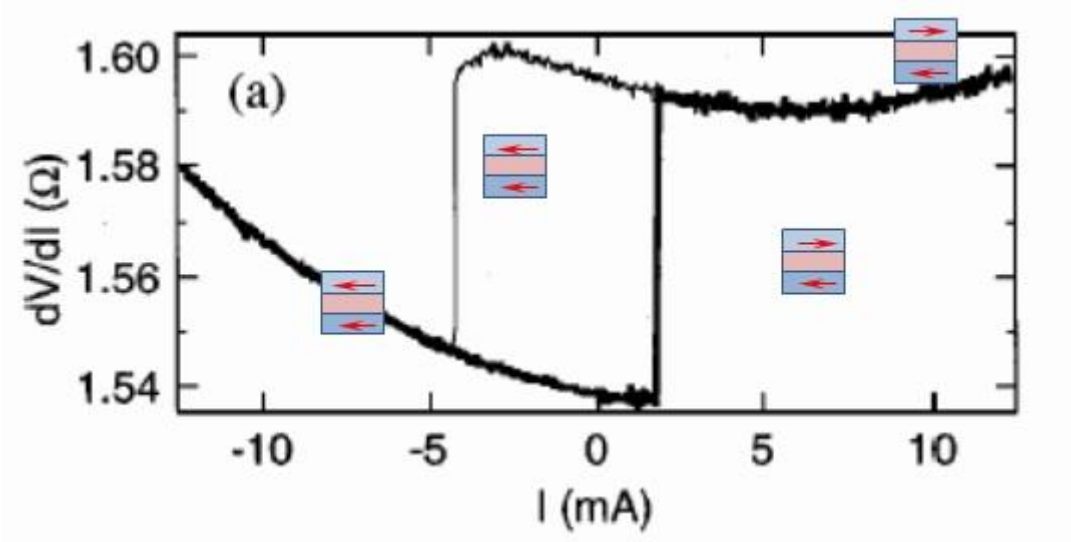

Fig. 2.12. Spin transfer curve of a nanopillar spin-transfer device (123)

2.4 Characterization Tool Background

2.4.1 X-Ray Diffraction (XRD)

X-ray diffraction (XRD) is a versatile, non-destructive technique that reveals detailed information about the crystallographic structure of natural and manufactured materials. Fig. 2.13 shows an XRD setup. The X-ray diffraction instrument is composed of three main parts as shown in Fig 1.1: X-ray source, a sample goniometer, and a X-ray detector. According to the relative position and motion of these three parts, a X-ray operation can be categorized into many modes, the most important of which are: wide angle diffraction, rocking curve, and in-plane diffraction. When an X-ray beam is directed at a solid material, the X-rays will be scattered in all directions. If these material atoms have long-range order, the lattice planes will cause interference between scattered X-rays, resulting in a unique diffraction pattern which can be captured, for example by an areal detector. This

pattern can provide the following structural information: crystalline phase identification, grain size, structural evolution in layered materials, microstrain analysis, macroscopic stress measurement and texture analysis. Structural information can be obtained from any crystalline material, including metals, ceramics and polymers.

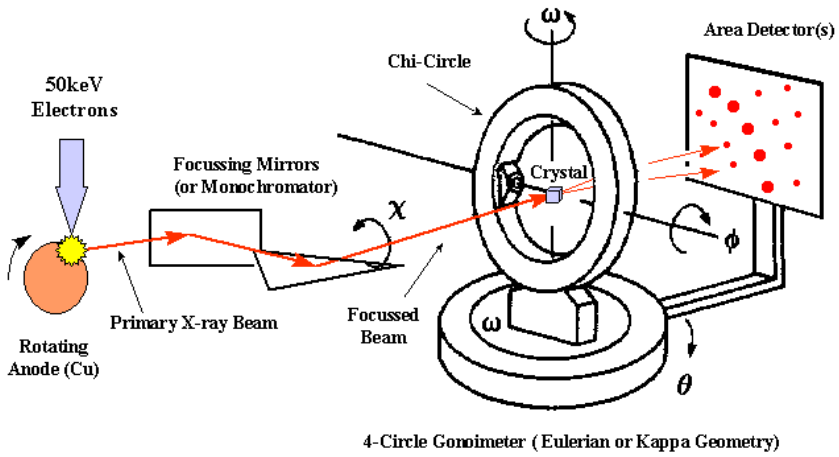

Fig. 2.13 XRD apparatus. (124)

X-rays are electromagnetic radiation with typical photon energies in a range of 100 eV - 100 keV. Short wavelength X-rays (hard X-rays) in a range of a few angstroms to 0.1 angstrom (1 keV - 120 keV) are used for diffraction applications. They are ideally suited for probing the structural arrangement of atoms and molecules in a wide range of materials because the wavelength of x-rays is comparable to atomic spacings. X-rays are generated by X-ray tubes when a focused electron beam is accelerated toward an anode, typically a rotating Cu disk. When the electrons

encounter the anode, X-rays with a characteristic wavelength are emitted, for example, 1.5406 Å for Cu Kα.

When X-ray photons collide with, electrons of a sample material, the photons will be scattered, and in certain conditions, they may interfere with each other. If the materials are crystalline, the atoms are arranged in periodic fashion. This periodicity leads to an interference called diffraction when specific geometric conditions are met, as defined by Bragg's law (Fig. 2.14). Here, two atomic planes are separated by the interplane spacing *d*, and incident X-rays that are scatterd by these planes travel different lengths as shown.

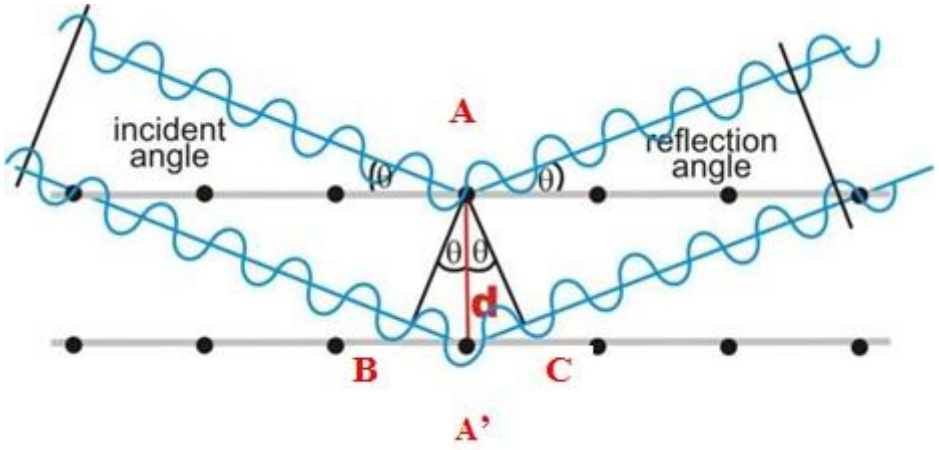

Fig. 2.14 A geometry of Bragg's law for a diffraction of X-rays from a set of crystal planes.

$$BA' + A'C = n\lambda = 2d\sin\theta$$

Where n is an integer, λ is the wavelength of radiation, d is the interplanar spacing, and θ is the diffraction angle or Bragg angle.

Bragg's conditions are satisfied by different d-spacings in materials at specific angles. Therefore, a plot of the angular position vs. intensity of the resultant diffracted peaks of is characteristic of the sample. Based on the results of X-ray diffraction, structural, physical and chemical information about the material can be obtained.

For a wide angle diffraction setup, sample gonoimeter rotates and θ is changed. The angle, 2θ, between the source and the detector to is kept constant. The angle, θ, between the sample and the source is changed. Every crystalline plane which meets Bragg law, can diffract the incident beam at a certain θ's, and a lattice parameter can be obtained from the peak position.

Phase identification using x-ray diffraction relies mainly on the positions of the peaks in a diffraction profile and to some extent on the relative intensities of these peaks. However the shapes of the peaks contain additional and often valuable information. Shrinking crystallite size causes peak broadening. The Scherrer equation explains peak broadening in terms of incident beam divergence which makes it possible to satisfy the Bragg condition for non-adjacent diffraction planes. Once instrument effects have been excluded, the crystallite size is easily calculated as a function of peak width (specified as the full width at half maximum peak intensity), peak position and wavelength.

The crystallite size as measured by the Scherrer method:

$$\langle L \rangle_{vol} = \frac{K\lambda}{B_{1/2} cos\theta}$$

Where $< L >_{vol}$ is the volume-weighted size, θ is the Bragg angle, λ is the wavelength of the X-ray, *K* is a unit cell geometry dependent constant whose value is typically between 0.85 and 0.99, $B_{1/2}$ is the full-width –half-max of the peak.

Rocking curve measurements are used as a gauge of the quality of epitaxial films. In a rocking curve measurement, θ is changed with a fixed 2θ angle. This measurement allows very precise measurements of diffraction angle around a specific angle of interest. The Full Width at Half Maximum (FWHM) is indicative of the mosaic spread and is inversely proportionally to the dislocation density in the film.

In order to acquire the highest signal from nanowire samples by focusing X-ray on as small as area, the Bruker-AXS Microdiffractometer was used in our experiment (Fig. 2.15).

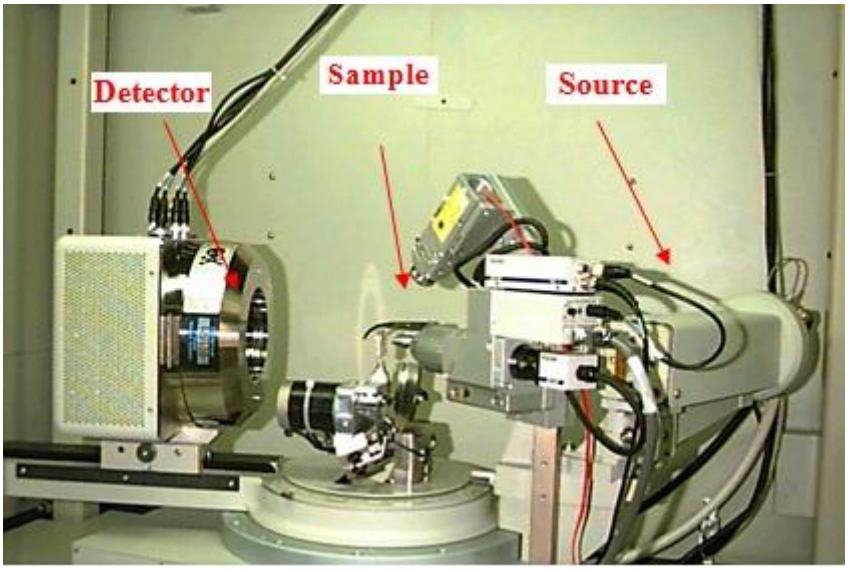

Fig. 2.15 Bruker-AXS Microdiffractometer

2.4.2 Vibrating Sample Magnetometer (VSM)

Magnetic properties of material are often measured by vibrating sample magnetometer (VSM), (Fig. 2.16). A basic VSM includes a vibration exciter, electromagnets, pickup coils and a sample holder. The sample holder rod is mounted on the vibration exciter which moves up and down at a set of frequency, typically 85 Hz. The samples can be rotated 360 ^{o} which allows angular measurements (in plane and out of plane). There are also three knobs for adjusting the x, y, and z position of the sample. When a magnetic sample is placed within a uniform magnetic field, the magnetization of the sample will align with the field by magnetic domain growth, or alignment of the individual magnetic spins. The alignment of the magnetization will be the larger as the applied field becomes stronger and internal magnetic structure is overcome. The magnetic field called the magnetic stray field will be generated by a magnetic dipole moment of sample. When the sample is made to undergo sinusoidal motion (i.e. mechanically vibrated), the magnetic stray field is changing as a function of time and can be sensed by a set of pick-up coils. A voltage read by the pick-up coils changes due to a change in magnetic flux, which is proportional to the magnetic moment of the sample. A standard sample of Ni with a given magnetization is used to calibrate VSM system to guaranty the measurement of samples accurate. The samples must be saddled at the center of pickup coils before starting measurement to ensure the sample is at the center of the field. Typical measurements include the M-H loops (hysteresis loops), magnetic moments, and anisotropy measurements.

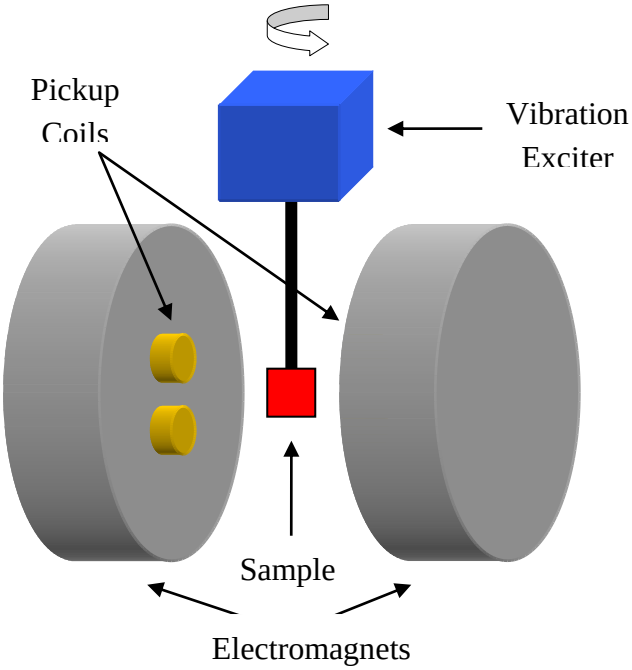

Fig. 2.16 A diagram of vibrating sample magnetometer (VSM)

2.4.3 Atomic Force Microscopy (AFM)

Gerd Binning and Heinrich Rohrer developed scanning tunneling microscope (STM) which was a precursor of atomic force microscopy (AFM). AFM, used on both conductors and insulators, was invented in 1986 by Binning, Quate, and Gerber. Sample information is gathered by scanning the surface with a mechanical probe. A atomically sharp tip is used to scan across a surface and specific probe-sample interactions are monitored. Piezoelectric elements enable the very precise scanning by adjusting accurate and precise movement.

Most AFM modes can work very well in ambient air and even in a liquid environment. Fig. 2.17 shows the setup of an AFM. The resolution of AFM is on a scale from angstroms to 100 microns. The AFM tip is positioned several nanometers

above the sample surface at the end of a cantilever beam. AFM relies on the forces between the tip and sample (Fig. 2.18). As the tip is moved to the sample's surface, the force is in an attractive regime. As it moves closer, the force regime switches to repulsive regime. The force is calculated by measuring the deflection of cantilever of AFM. The cantilever beam deflects according to Hooke's law when the tip is attracted or repelled by the sample surface. The variation of the height of tip is recorded as the tip scans across the sample surface. A feedback mechanism produces a topographic image of the surface. A laser is used to detect the deflection of the cantilever, and piezoelectric control is used to adjust the sample height to keep the deflections constant.

Hooke's Law:

$$F = -kZ$$

Where the force is F (N), the spring constant for the cantilever is k (N/m), and the deflection is Z (m).

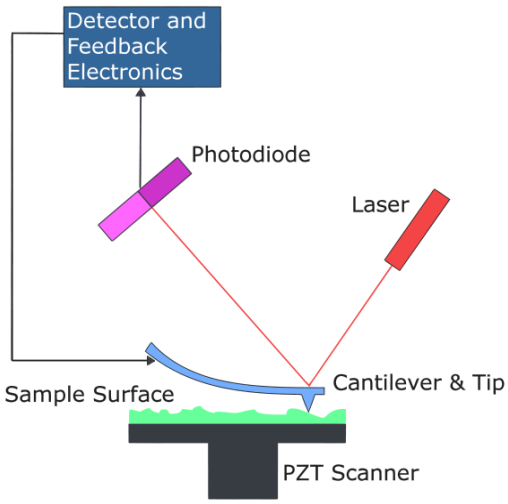

Fig. 2.17 A diagram of atomic force microscopy (AFM) (125)

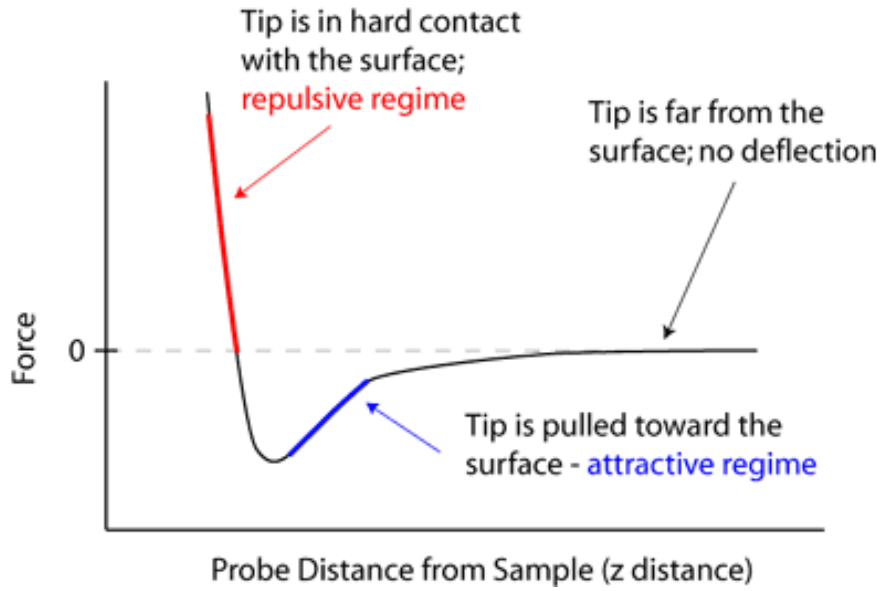

Fig. 2.18 Forces is as the function of distance between tip and sample (126)

The AFM has two working modes: contact mode and tapping mode. In contact mode, AFM tip operates by scanning the tip through the adsorbed layer on the sample surface. A constant deflection between the cantilever and the sample is maintained by vertically moving the scanner. The constant deflection in principle is the same as maintaining the constant force between the tip and sample. According to the Hooke's Law, the applied forces ranged from nN to μN with a general force constants range from 0.01 to 1.0 N/m. In tapping mode, AFM tip lightly taps the sample surface. The cantilever is oscillated at or near its resonance frequency with amplitude ranging typically from 20 nm to 100 nm. The amplitude is kept constant during scanning. The advantage of the tapping mode AFM is that it requires lower forces and causes less damage to soft sample surfaces.

Compared with two-dimensional images of electron microscopes, AFM provides a true three-dimensional surface profile. Samples do not require any special treatments (metal or carbon coating) for AFM. But, AFM measurement normally is a very slow process and an area of AFM images is much smaller than that of scanning electron microscope (SEM) images.

Besides the topographical image, AFM can be used to measure many forces, for example, mechanical contact force, capillary forces, electrostatic forces, magnetic forces, Van der Waals forces, chemical bonding, and so on. These often require specialized tips and data analysis.

2.4.4 Scanning Electron Microscope (SEM)

Max Knoll obtained the first SEM image on silicon steel in 1935. Then, Manfred von Ardenne performed the physical principles of the SEM and beam specimen interactions in 1937. The SEM was further developed by Charles Oatley and Gary Stewart. Finally, DuPont delivered the first SEM instrument.

SEM is a type of electron microscope that is used primarily to image the sample surface. In SEM, an electron beam is emitted from an electron gun made from a tungsten filament, lanthanum hexaboride cathodes, or zirconium oxide. An energy of the electron beam ranges from a few hundred eV to 40 keV. After being focused by a set of condenser lenses, the electron beam spot is about 0.4 nm to 5 nm in diameter. When a high-energy beam of electrons scans the sample, the electrons interact with the atoms of the sample. The electrons lose energy by repeated random scattering and

absorption in the sample. The interaction length extends from less than 100 nm to 5 μm into the sample surface.

The energy exchange between the electron beam and sample atoms generates many types of signals, including secondary electrons, back scattered electrons, X-rays, transmitted electrons. (Fig 2.19) These signals produce information about the sample surface topography, composition, or electrical conductivity. The secondary electrons are used to image of the sample surface. SEM can produce very high resolution images about 1 to 5 nm in size. Unlike optical and transmission electron microscopes, magnification in SEM is controlled by the current supplied to the x, y scanning coils, and not by objective lens power. SEM also can show spatial variation in chemical compositions of samples by back scattered electrons and energy dispersive X-ray spectroscopy (EDS). Back scattered electrons are electrons that are reflected from the sample by elastic scattering. Its images show information of the distribution of different elements in the sample. EDS X-rays are generated when the electron beam removes an inner shell electron from the sample, so a higher energy electron drops to the inner shell. The emitted X-ray has energy equal to the difference between the electron states, and is therefore characteristic of the element that emitted it. So X-ray energies can be used to identify the composition of the sample.

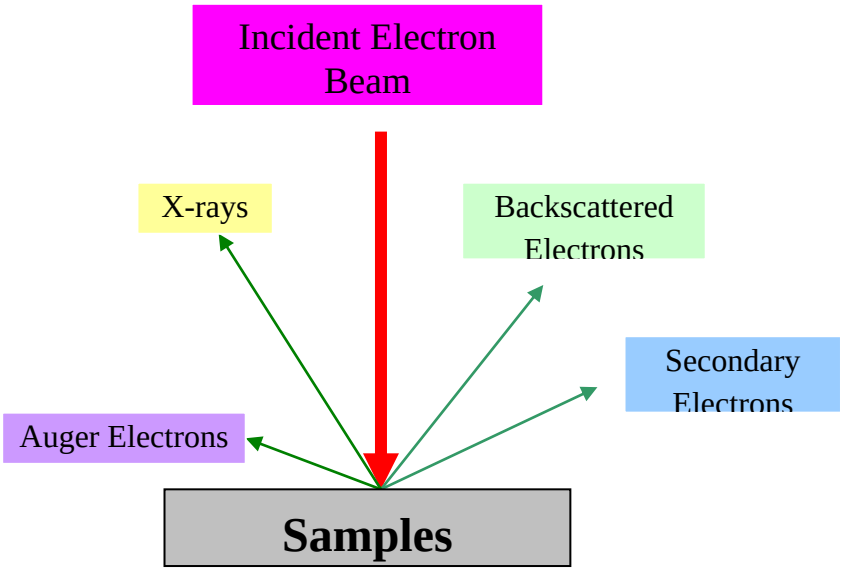

Fig. 2.19 The interaction between electron and specimen

A SEM system has some essential components including electron source, electron lenses, sample stage, detectors, power supply, vacuum system, cooling system, and so on. (Fig. 2.20)

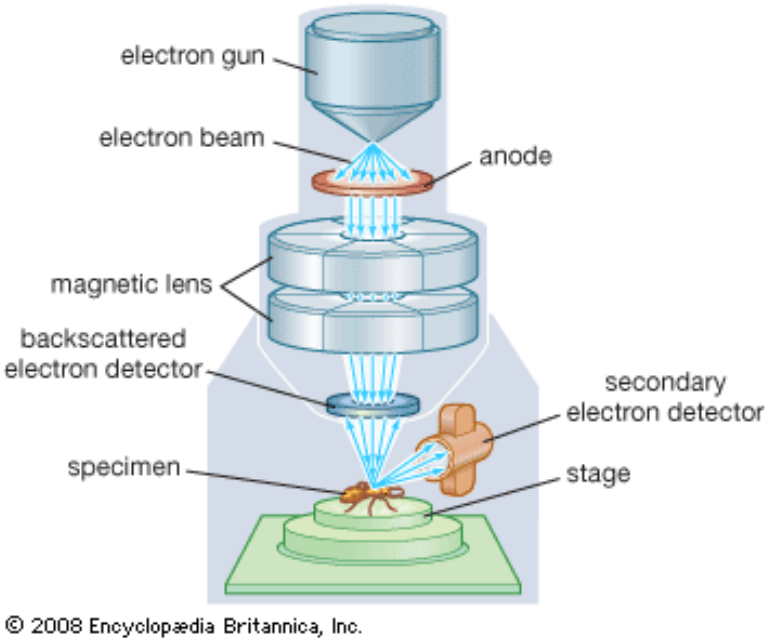

Fig. 2.20 Scanning electron microscope (SEM) (126)

SEM samples must be electrically conductive, at least at a surface. For nonconductive samples, they are charged during a scanning process by the electron beam. This causes scanning faults and other image artifacts. In order to solve this issue, an ultra-thin layer of electrically conducing material (Au, Pt, or C) is coated on a surface of samples by sputter coating or evaporation. After the coating, maximize signal and improved spatial resolution are acquired by preventing charging. Meanwhile, because SEM works in a vacuum on the order of 10^{-5}-10^{-6} torr, it is necessary that samples must be stable in the high vacuum system.

CHAPTER 3 FABRICATION OF NANOPORE ARRAYS

In order to form magnetic nanowires by the electrochemical deposition method, it is necessary to first fabricate nanopore templates. In addition to having nano-sized holes, the templates must be chemically and thermally stable during the electrodeposition process. In order to form high aspect ratio nanowires, the templates must also have very good mechanical properties. Many types of nanopore templates have been used to form nanowires by the electrodeposition method, including track etched polymer membranes, anodic porous alumina (AAO), nano-imprinting, and photoresist patterning by photolithography or e-beam lithography. In this research, different technologies were used to form templates with 10 nm diameter nanoholes. The templates included free-standing templates (self assembled AAO and prepatterned nanoimprinted AAO) and templates on Si (e-beam resist patterned pores and AAO from Al films).

3.1 Two-step Anodization

The nanopores discussed above are generally randomly distributed as grown on the Al surface because they form due to inhomogeneities in the current distribution caused by small topographic differences. Since Masuda developed the two-step anodization method (34), highly-ordered, uniform, straight AAO have been widely used as nanoporous templates to fabricate nano-size materials. It was found that

nanopore arrangement was improved after a long anodization period because the nanopores self-assembled at the metal-oxide interface to form defect-free regions in large domains.

The two-step anodization process used in this work is shown in Fig. 3.1. High purity alumina foils (> 99.99%) were degreased in acetone for 10 minutes at room temperature and rinsed in methanol, isopropyl alcohol (IPA), and deionized (DI) water separately. After drying in nitrogen, the native oxide layer was removed using a 1 M NaOH solution for 3 minutes. A DI water rinse and N_2 drying were followed by electrochemical polishing to remove defects of the surface of the Al foil. The electrochemical polishing solution was a 1: 5 mixture of perchloric acid ($HClO_4$) and ethanol, and a constant potential of 18 V at 6 ^{0}C was applied. A first anodization was then performed in acid. The pores beaome ordered at the AAO/Al interface after a long first anodization. So, this first layer of alumina was etched away by a mixture of 5% H_3PO_4 and 1.8% chromic acid at 60 ^{0}C for couple of hours depending on the thickness of alumina. This left indents on the surface of the Al which nucleated ordered pores during the second step of anodization. The Al was anodized again at the same anodization conditions. After couple hours of anodization, ordered nanopores were obtained in the new AAO. Because AAO formed on both sides of the Al foil, it was necessary to separate two AAO to make two free-standing AAO membranes. The layer of Al between the two AAO layers was etched using a saturated mercuric chloride ($HgCl_2$) solution for three hours at room temperature. The layer of alumina at

the bottom of the pores,called the barrier layer, was removed by 5% phosphoric acid for couple of minutes. Finally, ordered nanopores were ready for the electrochemical deposition of nanowires.

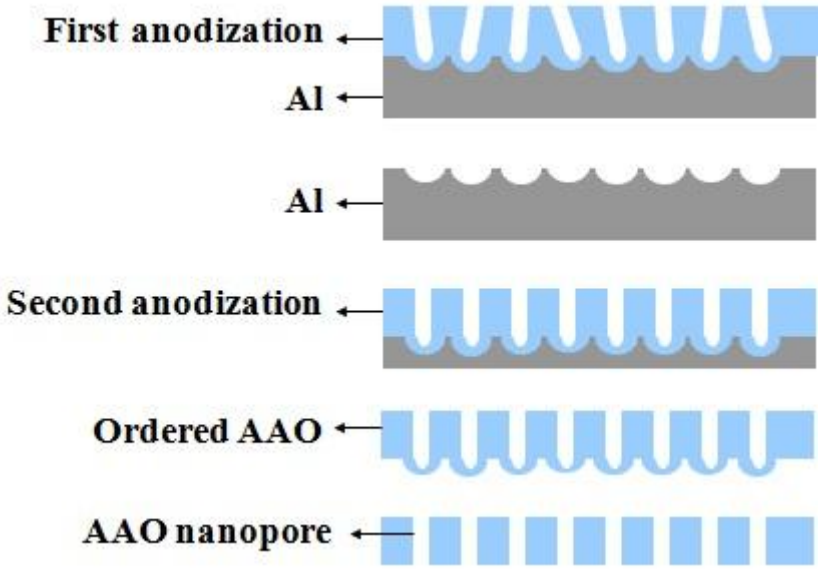

Fig. 3.1 AAO fabrication procedure of two-step anodization

Fig. 3.2 shows SEM images of AAO after the first anodization (a) and the second anodization (b).It is clear that the nanopores from the second anodization are much more uniform and ordered than those from the first anodization. Nanopores after the second anodization have a hexagonal distribution on AAO surface. Imperfections can still be found in Fig. 3.2 (b). This problem is due to two reasons. One is the defect from the original Al foil, which is shown in the area of the red circle 1. Although high purity Al foils are used to make AAO templates, they have some defects from Al

manufacturing, such as defects and scratches. The other reason is the grain boundaries in the Al precursor, which is shown in an area of the red circle 2.

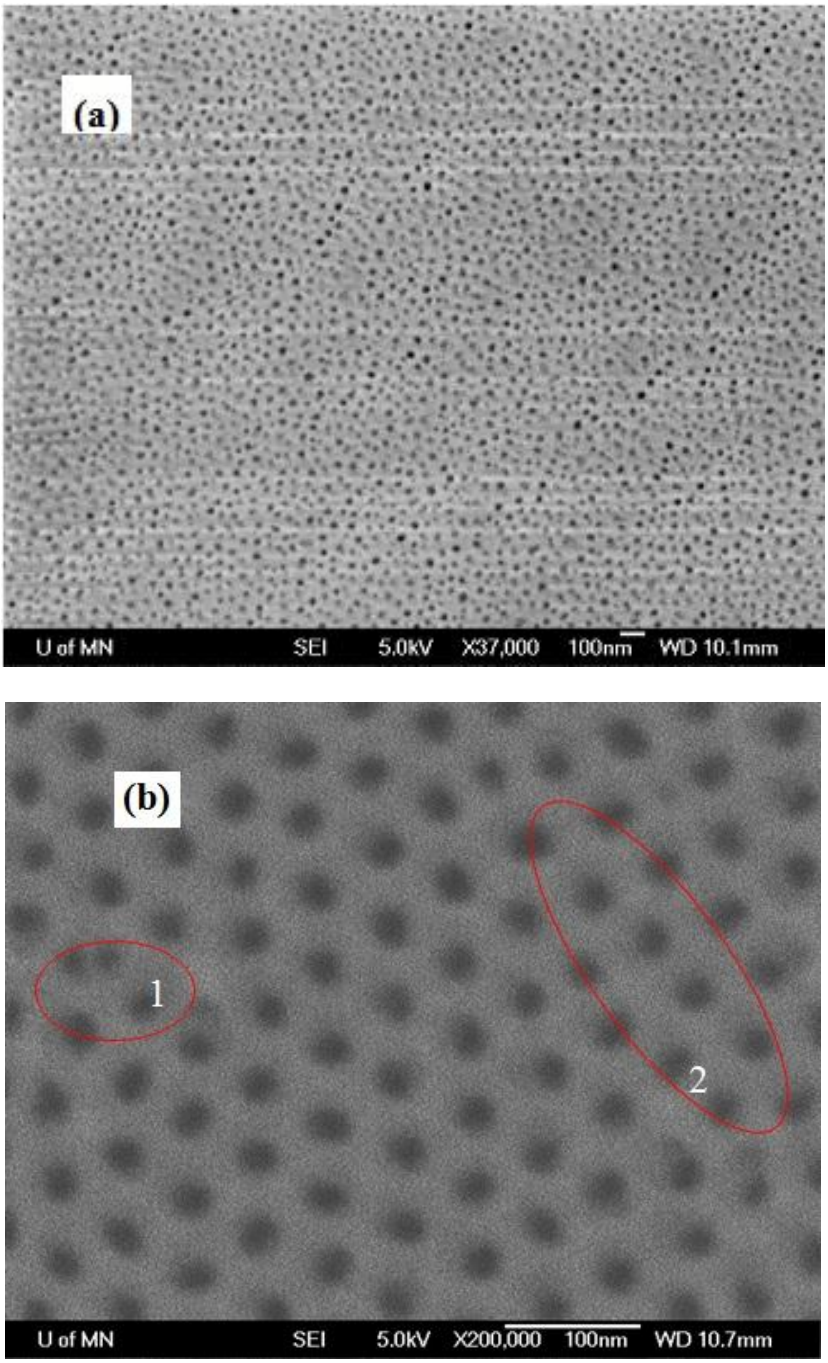

Fig. 3.2 SEM images of AAO (nanopore diameter is 20 nm)

(a) after the first anodization, (b) after the second anodization

The nanopore diameter is dependent on the anodization conditions. Most researches have focused on 40 nm to 60 nm, 90 nm to 140 nm, and 220 nm to 300 nm regimes, respectively. (36)The diameter of nanopores can be adjusted from a couple of nanometers to hundreds of nanometers by controlling the anodization conditions (especially the anodization potential and the type of acid). Small diameter nanopores can be achieved when Al foil is anodized in H_2SO_4 at low anodization potentials.

In this research, it was very important to fabricate 10 nm diameter nanopores for small device areas. In order to achieve 10 nm diameter nanopores, Al foil in this work was anodized in different concentrations of H_2SO_4 under different anodization potentials at 1 ^{0}C. Polished Al foil was anodized for 3 hours as the first anodization to force order at the interface between AAO and Al foil. After etching away the first layer of AAO, the Al was anodized for 14 hours at the second step of anodization to achieve thick enough AAO templates for handling.

Fig. 3.3 is a summary of nanopore diameter versus different anodization conditions for the first-step anodization. When the anodization potential was increased, the distribution of nanopore diameters became broad although the average diameter did not increase initially. The optimal concentration appeared to be 1.5 M H_2SO_4, the smallest nanopores were fabricated at 15 V during the first-step anodization. So, this recipe was used for second-step anodization to form ordered nanopore with 10 nm diameters.

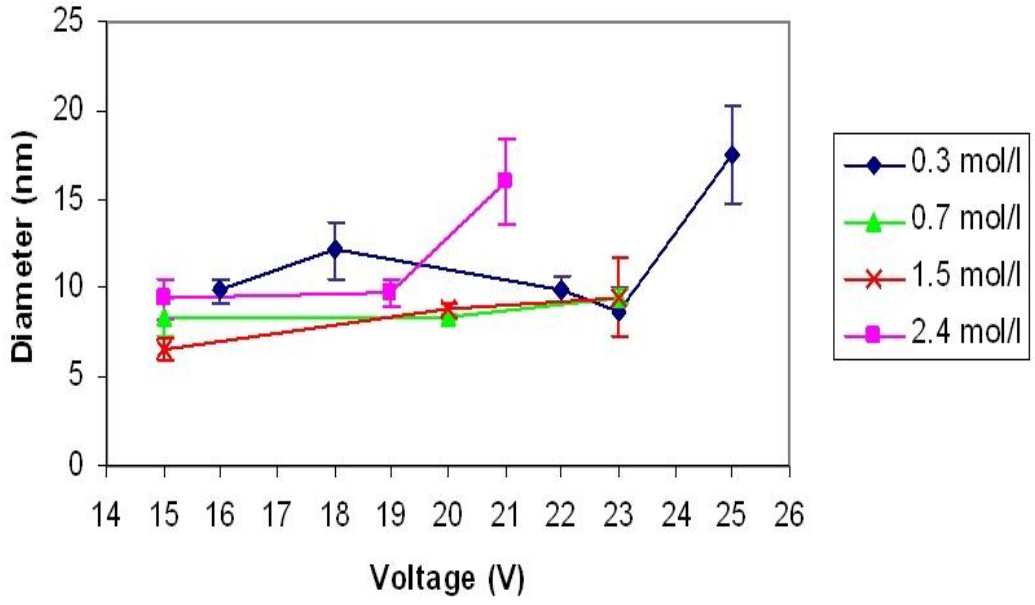

Fig. 3.3 Al was anodized in different concentrations of H_2SO_4 at 1 ^oC during the first-step anodization

Fig. 3.4 shows SEM images AAO templates including a top view (a) and a cross section (b). From the top view, ordered and uniform nanopores distributed on the surface of AAO. The diameter of nanopores was less than 10 nm. The spacing from center to center of the nanopores was 30 nm and their areal density was 1.1×10^{13} pores/cm^2. Parallel nanopores were observed in the cross section of nanopores. The pores appear rough, but this is a fracture surface because the small diameters do not polish well for cross sectional imaging. The total thickness of the AAO templates was 17 μm after 14 hours of anodization. The rate of Al anodization under this condition was 3.37 Å/s.

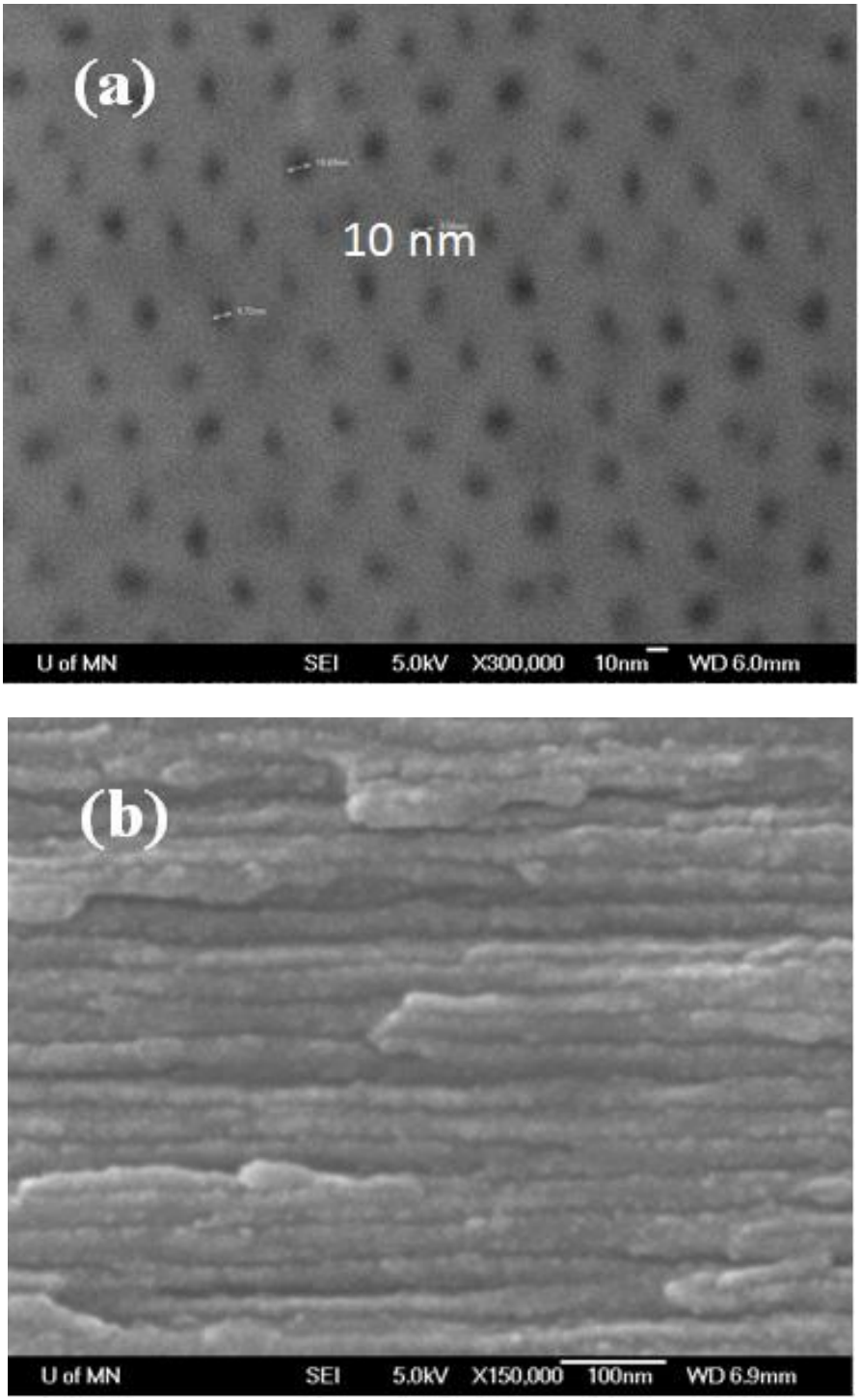

Fig. 3.4 AAO with 10 nm diameter nanopores.

(a) top view, (b) cross section

3.2 Nano-imprinting

Two-step anodization is limited in its by its resulting short range order. For example, MRAM, high density magnetic storage media, (127) and photonic crystals (128) all require templates with a long range order. Nano-imprinting (41) the Al precursor can be used to solve the limitations of two-step anodization. Also, electron-beam lithography (EBL) (129) can be used for long range order, and initial work in this area will be discussed in the next section.

Nano-imprinting the Al precursor can be used to fabricate AAO nanopore arrays with long range order over millimeter-scaled domains. Although the fabrication of a master stamp is a slow and expensive process because EBL is often used, nano-imprinting is still an inexpensive method because this stamp can be used many times. Meanwhile, the size and distribution of nanopores can be very precisely controlled. When the patterned nano-imprint dimensions match the self-ordering conditions of anodization, ordered and uniform nanopores form in the resulting oxide after one-step anodization. The nano-imprint process is shown in the following steps. 1) Fabricate a master stamp with nanometer-sized, ordered patterns by EBL; 2) Use the master stamp to imprint the surface of electrochemically polished Al foil; 3) Anodize the patterned Al foil under required anodization conditions shown in previous chapter.

The fabrication process of a master stamp and an AAO template is shown in Fig. 3.5. First, 500 nm thick Si_3N_4 was grown on Si by low pressure chemical vapor deposition (LPCVD) system. Second, 30nm thick negative e-beam photoresist, NEB-

31, was coated on top of Si_3N_4 by spin coating. Third, the coated NEB-31 was patterned by a Raith-150 system. The accelerating voltage was 20 KV and the aperture size was 10 m in Raith-150. After developing in DC-26, NEB-31 patterns were formed on the surface of Si_3N_4 (Fig. 3.6). The NEB-31 pattern was used as a mask to etch Si_3N_4 by reactive ion etching (RIE) form a master stamp (Fig. 3.7). The patterns of the master stamp were then transferred to the surface of an electro-chemically polished Al foil by nano-imprinting process. During nano-imprinting, the surfaces of the Al foil and the master stamp were kept parallel to prevent relative movement between two surfaces. After the two surfaces contacted each other, a constant force of 1000 lb/mm^2 was applied for 30 seconds. Fig. 3.8 is images of patterned Al foil. The imprint depth was as deep as 211.4 nm. Because the measurement was limited by the diameter of nanoimprints and the length of the AFM tip, the AFM tip may not have contacted the bottom of the nanoholes on Al foil. The patterned Al was anodized by a one-step anodization process at 195 V in phosphoric acid at 0 ^oC. Finally, an AAO template with ordered uniform nanopores was ready for electroplating nanowires. From Fig. 3.9, it is clearly shown that the nanopore size is very uniform through the thickness of the template, and the nanopores were perfectly parallel each other. There is a very clear line between the patterned area and unpatterned area. Nanopores only distributed uniformly in the patterned area. In the unpatterned area, nanopores were randomly distributed similar to what happened in the first anodization in a self-assembled process as discussed in the last section.

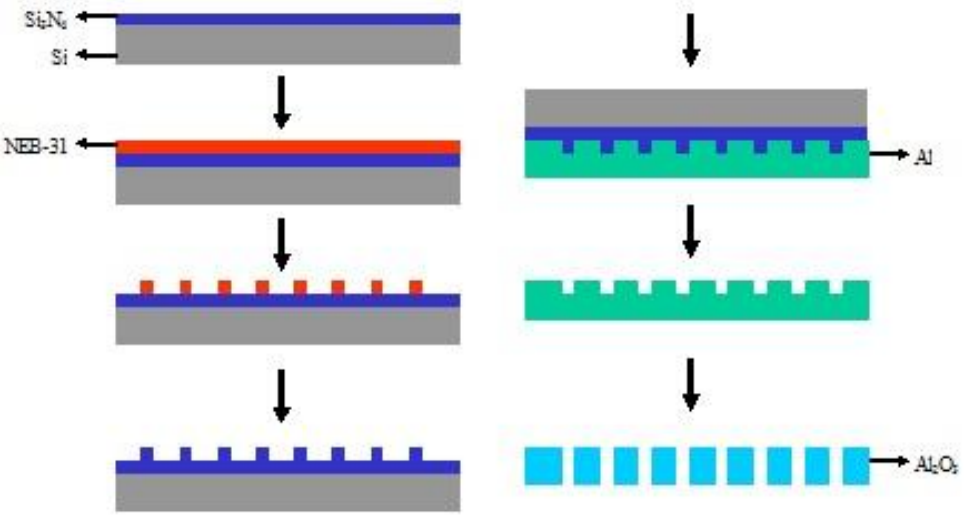

Fig. 3.5. Fabrication process of master stamp and nanoimprinted AAO template

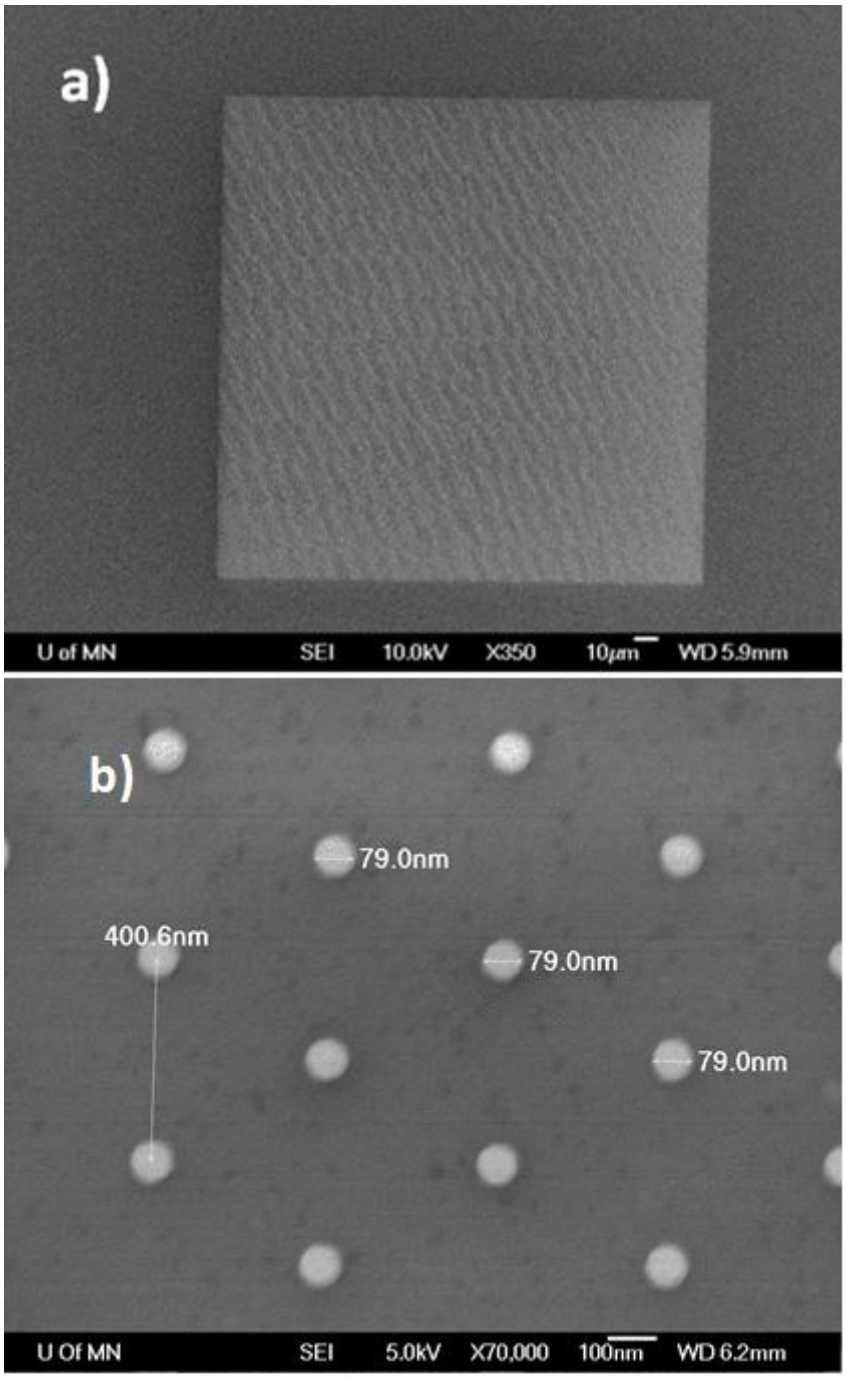

Fig. 3.6 NEB-31 pattern overview (a) and zoomed in (b).

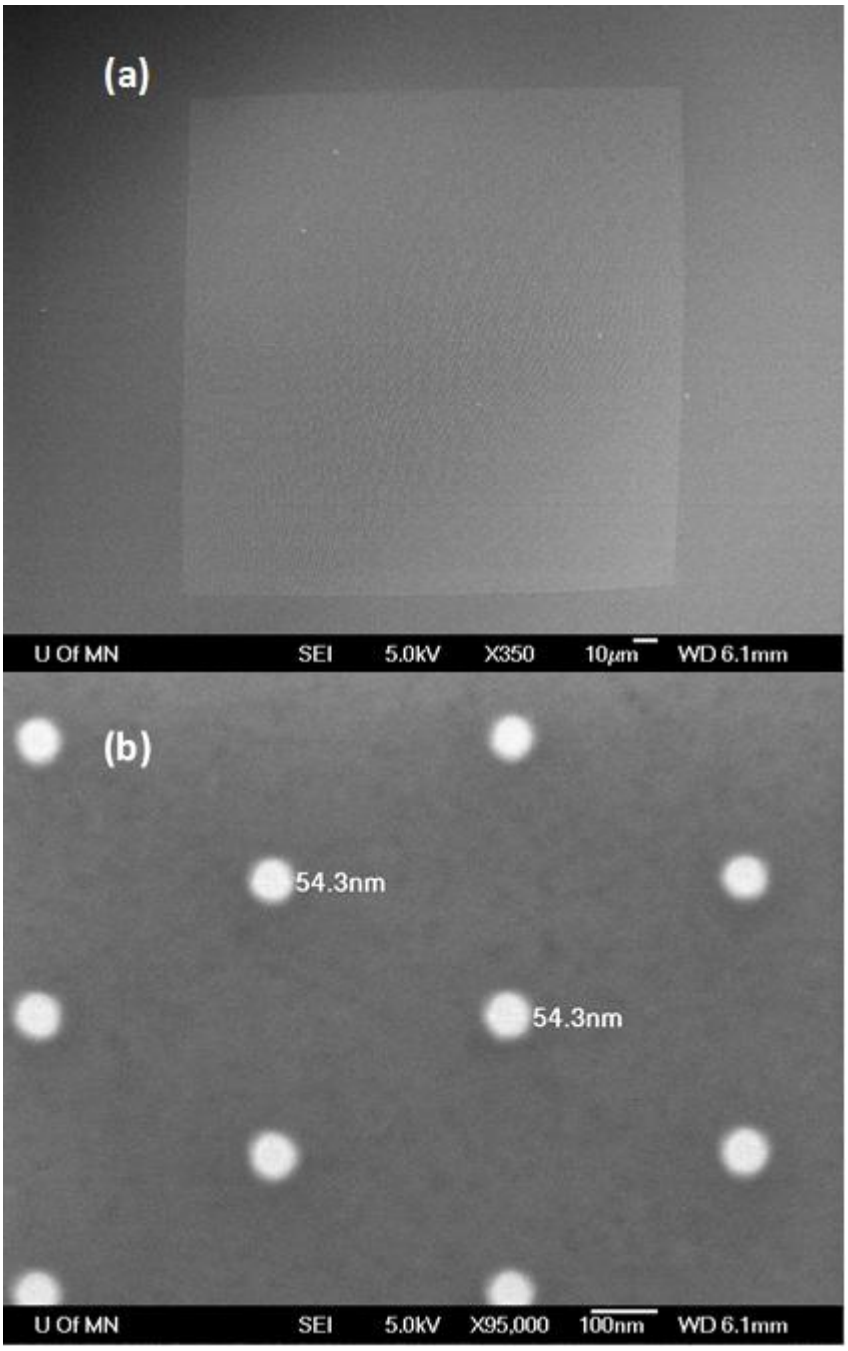

Fig. 3.7. Si_3N_4 pattern overview (a) and zoomed in (b).

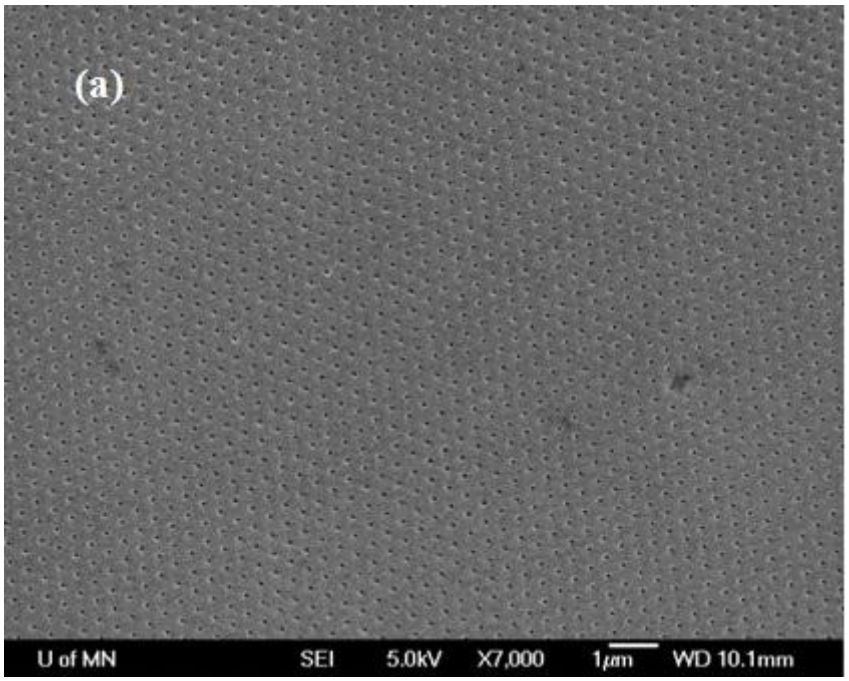
(a)
U of MN
SEI
5.0kV
X7,000
1μm
WD 10.1mm

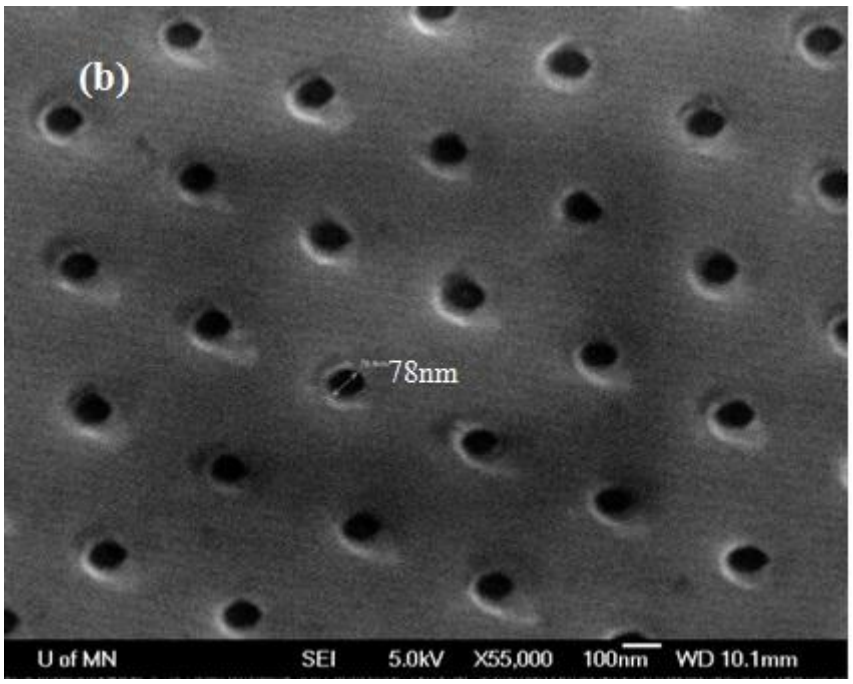
(b)
78nm
U of MN
SEI
5.0kV
X55,000
100nm
WD 10.1mm

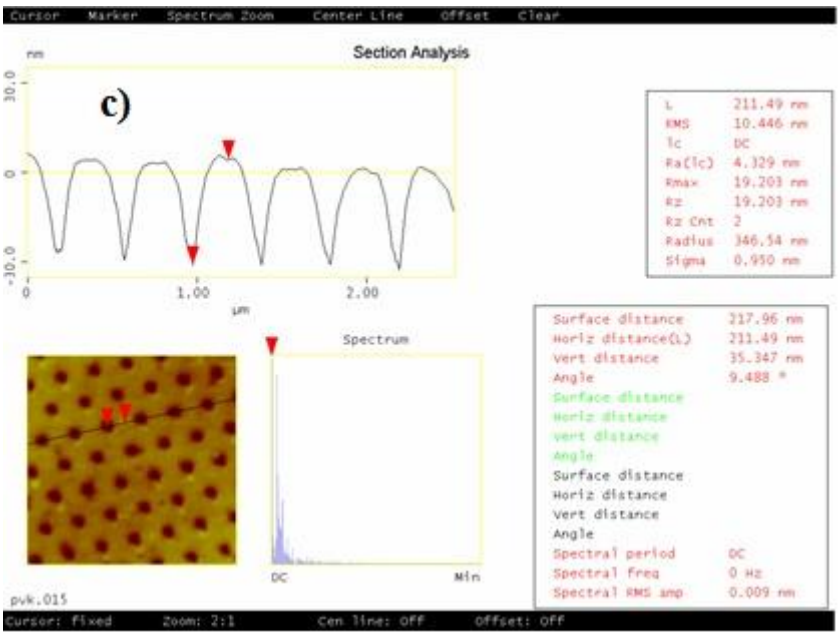

Fig. 3.8 Imprinted Al foil overview (a), zoomed in (b), AFM image (c).

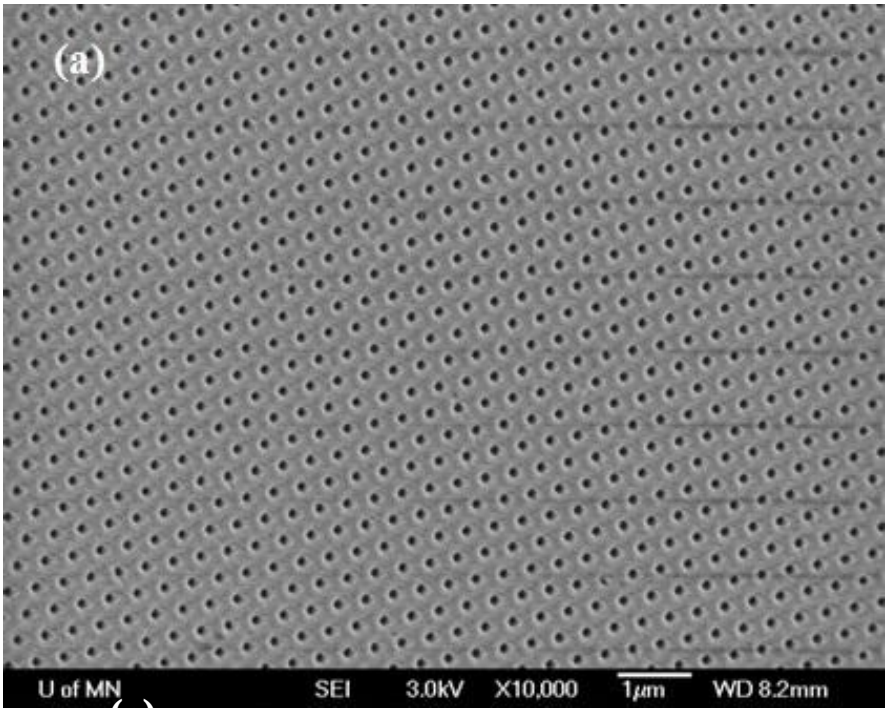

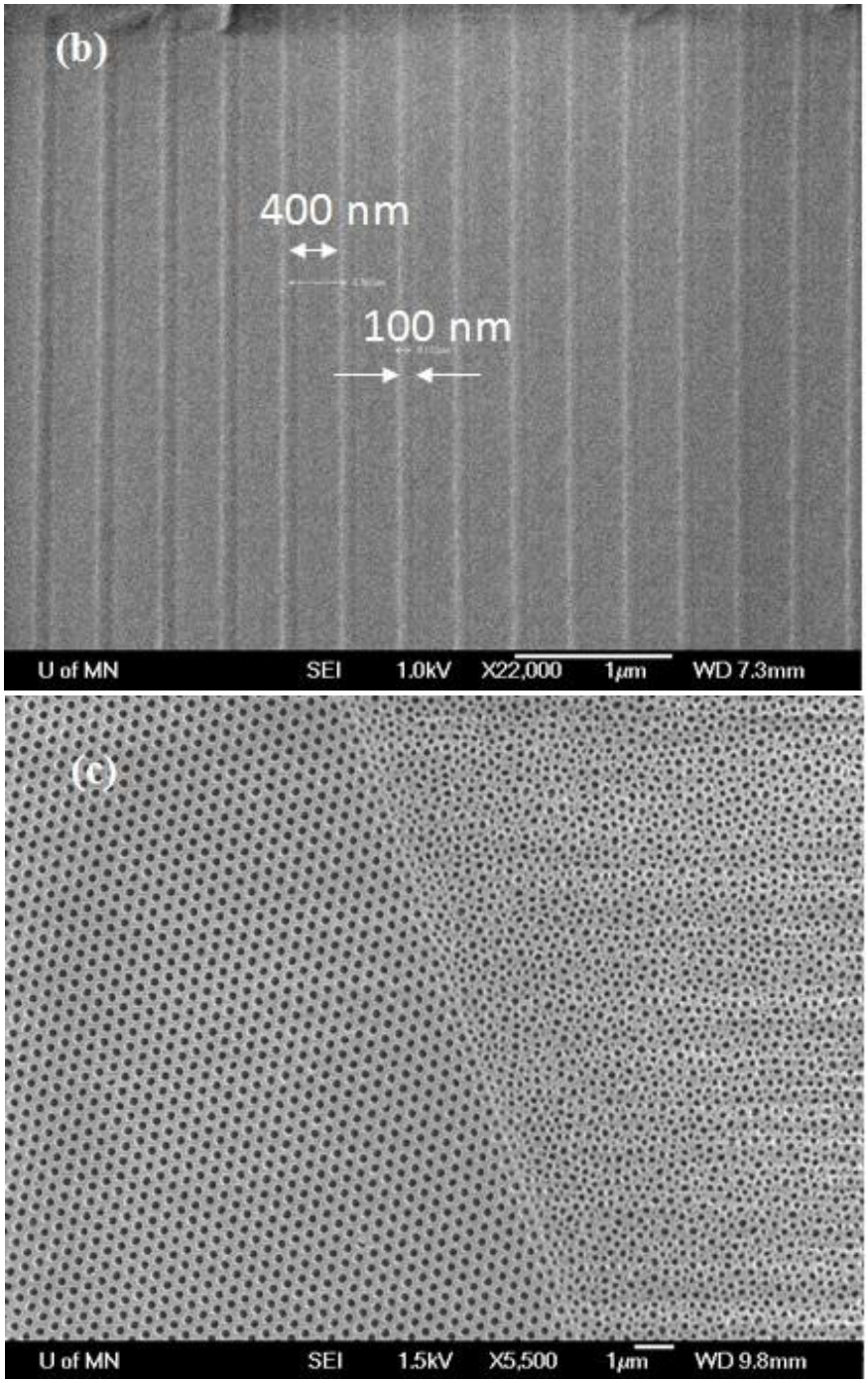

Fig. 3.9. AAO template made by nanoimprinting Al (a) top view, (b) cross-section view, (c) boundary between patterned and unpatterened areas

As disused in the previous paragraph, one of the problems with two-step anodization is the disordered nanopores that form at the grain boundaries of the

precursor Al. Nano-imprinting shows an advantage here (Fig. 3.10). It is clearly shown that nanoholes uniformly distributed in the oxide, even over the boundary of Al grains.

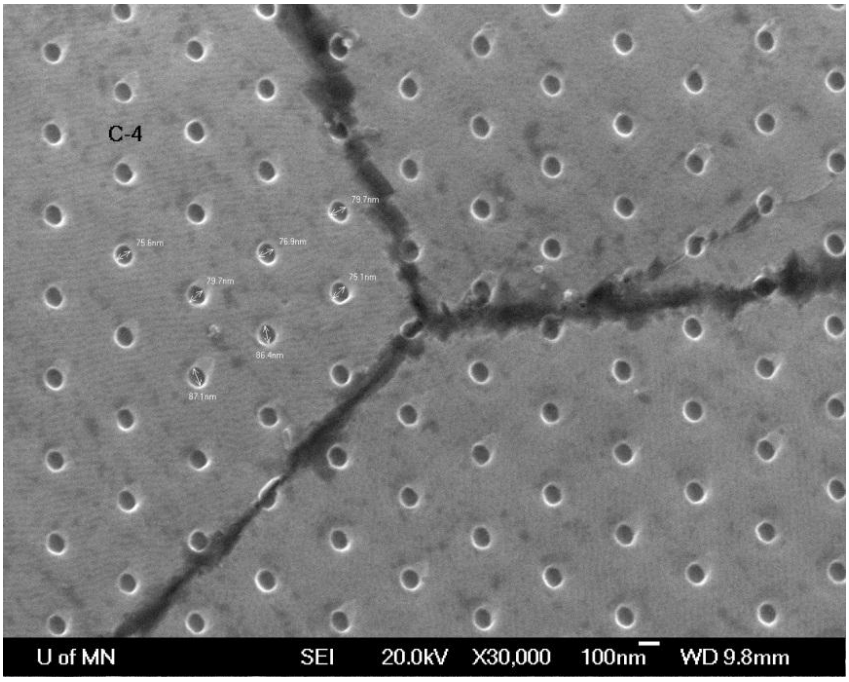

Fig. 3.10 Nanohole pattern across Al domain boundaries of Al foil after nano-imprint

During the nano-imprint process, it is very important to prevent the master stamp and the Al foil from slipping relatively to each other to avoid scratches by the Si_3N_4 pattern (Fig. 3.11). Ordered nanopore could not be achieved by anodizing this Al, but it is encouraging that the master stamp survives such events to be used 10-100 more times.

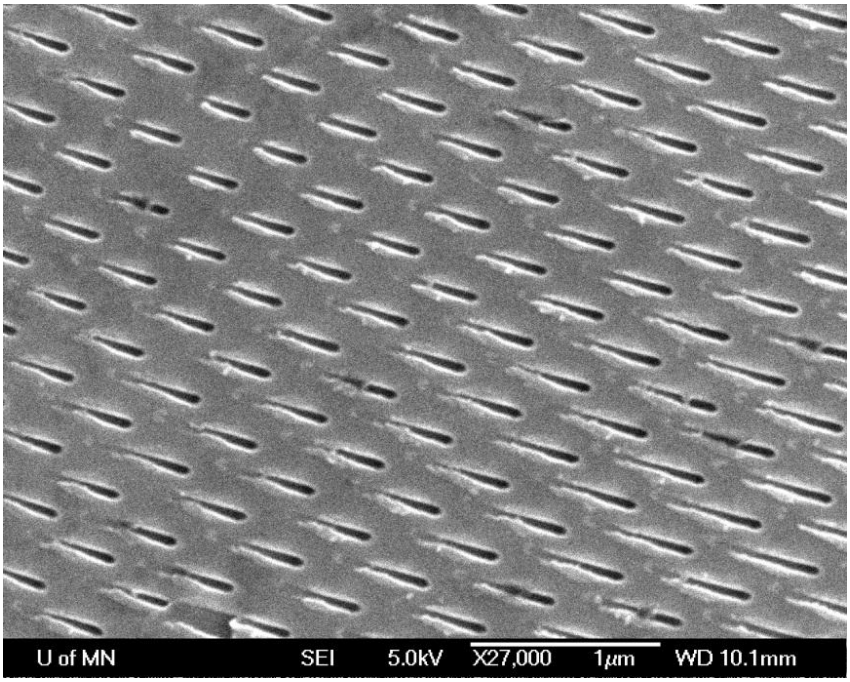

Fig. 3.11 Scratch on surface of Al foil due to stamp slipping.

Once the success of nanoimprinting was determined, optimization of the master stamp fabrication had to be performed because in this work, it was very important to fabricate nanoholes with as small a diameter as possible. This very small spacing is challenging even with EBL because the resolution of EBL is limited by the Raith-150 system (acceleration voltage, aperture size, and resolution), fabrication conditions (vibration, temperature, and humidity), and NEB-31 photoresist (resolution and thickness). So, it was necessary to use a dose test to know the smallest diameter pattern possible by EBL. Fig. 3.12 shows the results of a dose test where a group of patterns was designed with varying doses for different rows. The dose was increased step by step. One result of the dose test is the relation between dose and diameter of patterns. From Fig. 3.12, it was clearly shown that the diameter of pillars increased

gradually as the dose increased. At low doses, the patterns could be resolved. Fig. 3.13 shows the dose test results of NEB-31. The spacing between patterns was designed 50 nm, 100 nm, 200 nm, 300 nm, and 400 nm. When the spacing was smaller than 100 nm, the patterns were not resolved even at very small doses (≈ 0.002 pAs). When the spacing was bigger than 200 nm, single dots could be found. The diameter of dots increased linearly with increasing dose. For patterns with 200 nm spacing, the smallest diameter of a single dot was 70 nm at 0.0025 pAs. After the dose was increased to 0.0035 pAs, the dot diameter was 90 nm. Then, all of dots merged and formed a film as the dose increased further due to overexposure. For patterns with 300 nm spacing, the smallest diameter of a single pattern was 60 nm at 0.0025 pAs. At 0.01 pAs, the diameter of the dots was 140 nm, and increased doses again resulted in a photoresist film. For patterns with 400 nm spacing, the smallest diameter of a single pattern was 50 nm as dose was 0.002 pAs. As the dose was increased to 0.015 pAs, the diameter increased to 170 nm. So, the smallest pattern was 50 nm with spacings of 400 nm.

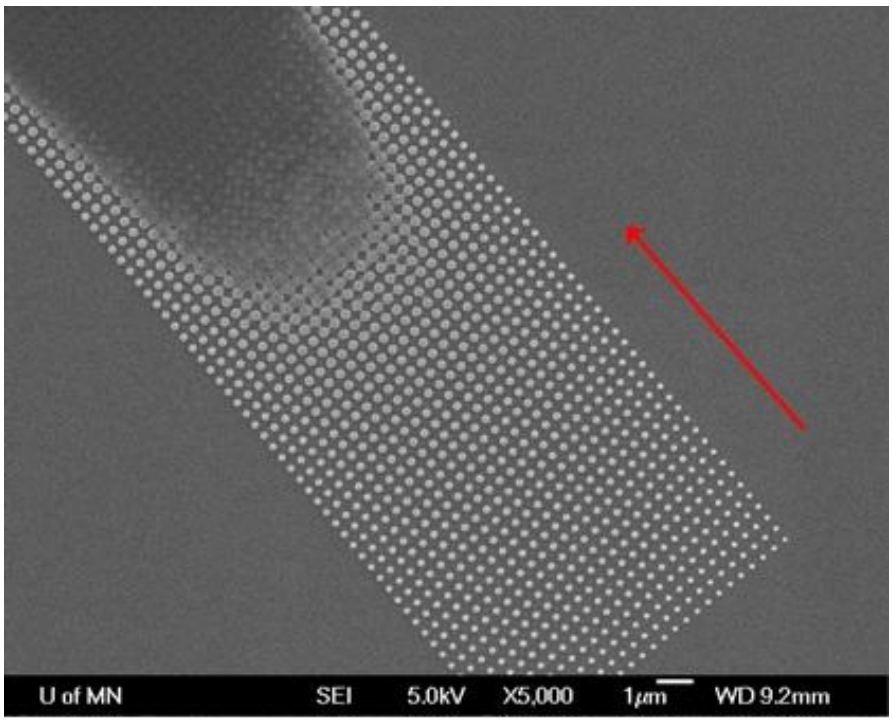

Fig. 3.12 Dose test

(Dose increasing as the direction of arrow)

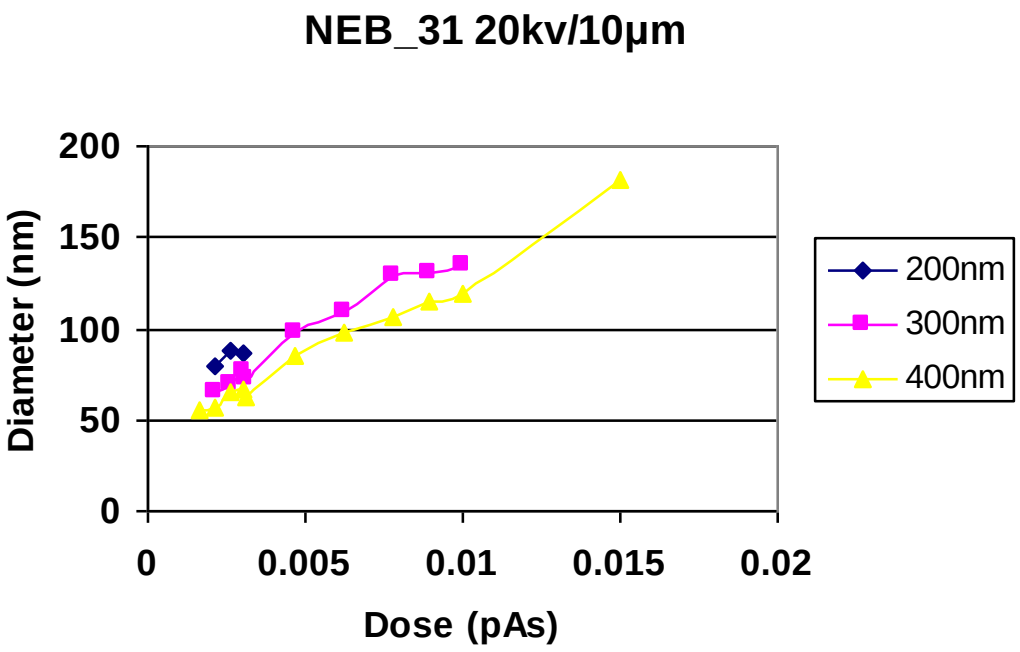

Fig. 3.13 Dose test result of NEB-31 pattern by EBL (Raith-150)

These results were very successful compared to others using the Raith 150, but they were not good enough to make stamps for AAO of the dimensions needed for this work. The diameter of AAO nanopores can be as small as 10 nm. As discussed previously, the spacing between the pores is twice of nanopore diameter in AAO. Under this anodization conditions, the spacing is only 20-30 nm. As determined by the results of the dose test, it was not possible to fabricate a mater stamp with 10 nm pillars by our EBL conditions. A higher acceleration voltage exposure system and a very quiet clean room environment will be required in future research.

3.3 Photoresist Templates Patterned by E-beam Lithography

For many applications, multilayered nanowires with low dimensions and low aspect ratios are required and interpore spacing could be larger (eg: MRAM), so AAO precision may not be needed. However, when the arrays are fabricated via etching of thin films, the edges of the multilayers can lose their integrity, which affects device performance increasingly as the nanowire diameters decrease. Therefore,electrochemical deposition can be used with templates other than AAO to produce sharp interfaces throughout the device thickness with varied desired dimensions. (27) (29) (130) For example, electron beam lithography (EBL) offers the advantage of forming ordered arrays of nanopores with low aspect ratio and the capability of adjusting the spacing among the nanopores. In this study, ordered arrays of polymethylmethacrylate (PMMA) with nanopores were fabricated with use of dot mode EBL, which considerably reduced processing time and cost.

E-beam lithography (EBL) of PMMA to form nanopores is shown in Fig. 3.14. A layer of PMMA was spun onto a Ti/Cu electrode film that had been sputtered onto a Si wafer. The Ti layer had a thickness of 5nm and was used to increase the adhesion between Cu (200nm) and Si. The bonding strength between Cu and PMMA has to be high so that the electrolyte, in subsequent electrodeposition, cannot infiltrate between them. Therefore, a layer of 3-animopropyl-triethoxysilane (APTES) was spun onto Cu to increase its adhesion strength with PMMA from 0.75 Kg/cm to 2.5 Kg/cm. (134) PMMA with molecular weight of 950 K and a concentration of 4% was spun onto the Cu film at 4000 rpm for 30 seconds, and it was then baked at 180^{o}C for one minute. Next, the PMMA film was patterned by Raith 150. The patterning parameters were set at a 20 kV accelerating voltage, a 20 μm aperture. Dot mode was selected as the exposure mode. For samples with area of 200 μm × 200 μm and 1000 nm spacing between pores, the exposure time was 2 minutes. After exposure, the samples were developed using a methylisobutylketone (MIBK) / isopropanol (IPA) (1:3) solution for 40 seconds at room temperature. Finally, the samples were washed by IPA and then dried using pure nitrogen. Fig. 3.15 is a typical PMMA pattern after EBL.

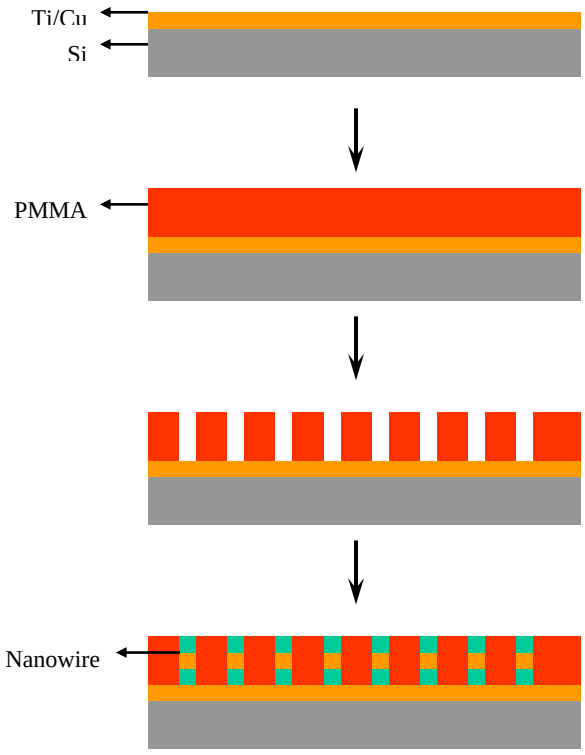

Fig. 3.14 Fabrication process of PMMA nanoholes by EBL

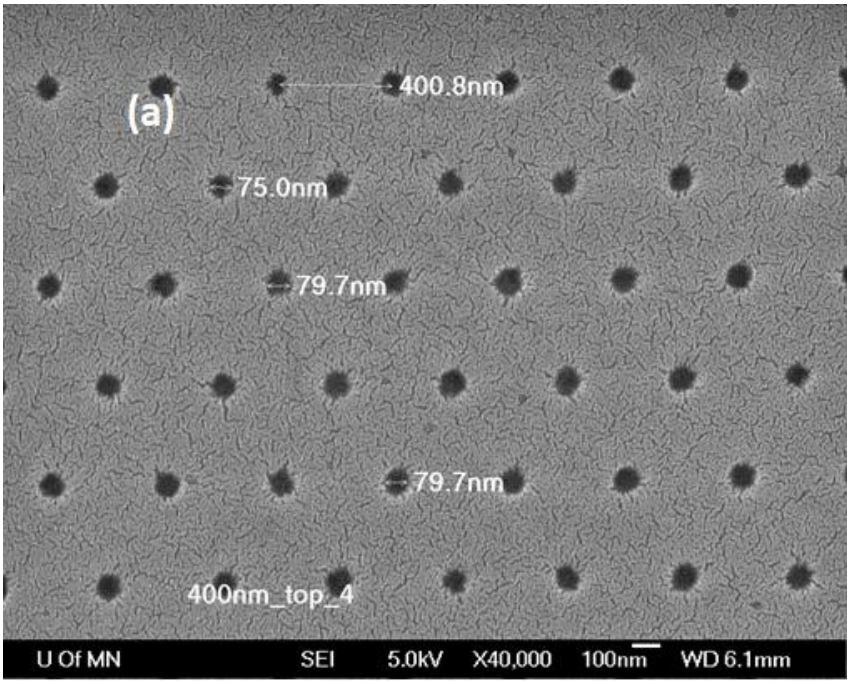

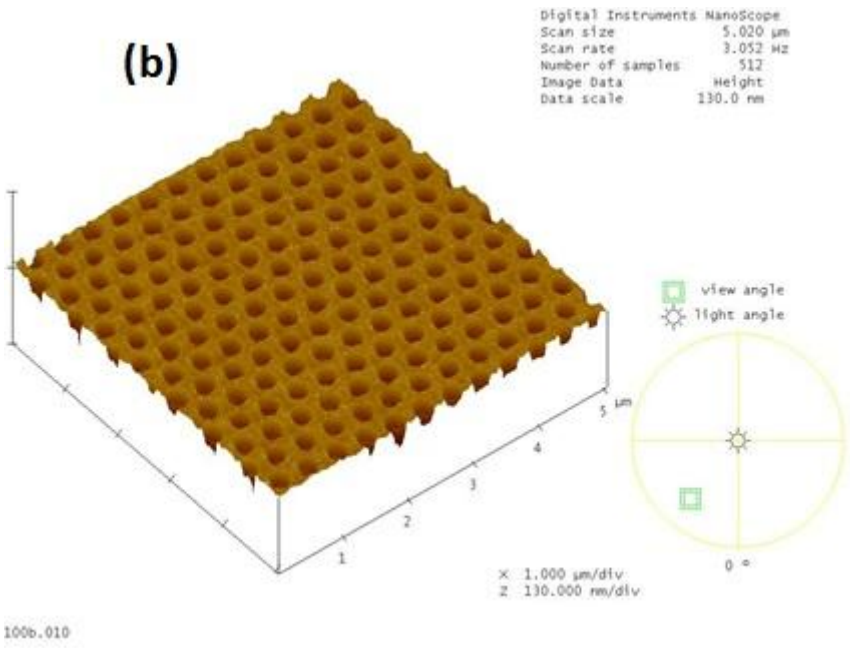

Fig. 3.15 (a) SEM and (b) AFM images of PMMA nanopores after EBL

In order to achieve as small as possible nanopores in PMMA, it was again necessary to perform a dose test which was similar as the dose test of EBL-31. But, because PMMA is a positive resist, nanoholes were obtained after the EBL in this study. As is well known, EBL is a very slow and expensive fabrication method. So, dot mode was selected as an exposure mode. Compared with area mode, dot mode saves exposure time and stage motion time. Meanwhile, it uses the exposure time to control the diameter of pattern.

Fig. 3.16 is the results of a dose test with PMMA (A4). It was clearly shown that the diameter of nanoholes increased gradually as the dose increased. At low doses, the holes were resolved. But again at high doses, the patterns connected together. The spacing between the nanoholes was designed to be 100 nm, 200 nm, 300 nm, and 400 nm in 4 different tests, respectively. When the spacing was smaller than 100 nm, all of

patterns connected even at very small doses (≈ 0.001 pAs). When the spacing was larger than 200 nm, single holes could be found. For patterns with 200 nm spacing, the smallest hole diameters were 75 nm at 0.002 pAs. As the dose increased to 0.015 pAs, the diameter of the holes was 150 nm. Then, all of patterns connected together as the dose increased further. For patterns with 300 nm spacing, the smallest hole diameters were 65 nm at 0.002 pAs. After dose increased to 0.03 pAs, the hole diameters were 210 nm. For patterns with 400 nm spacing, the smallest hole diameters were 50 nm at 0.001 pAs. After dose increased to 0.03 pAs, the hole diameters were 180 nm. It is clear that the achieved smallest pattern was 50 nm as the spacing was 400 nm and the dose was 0.001 pAs.

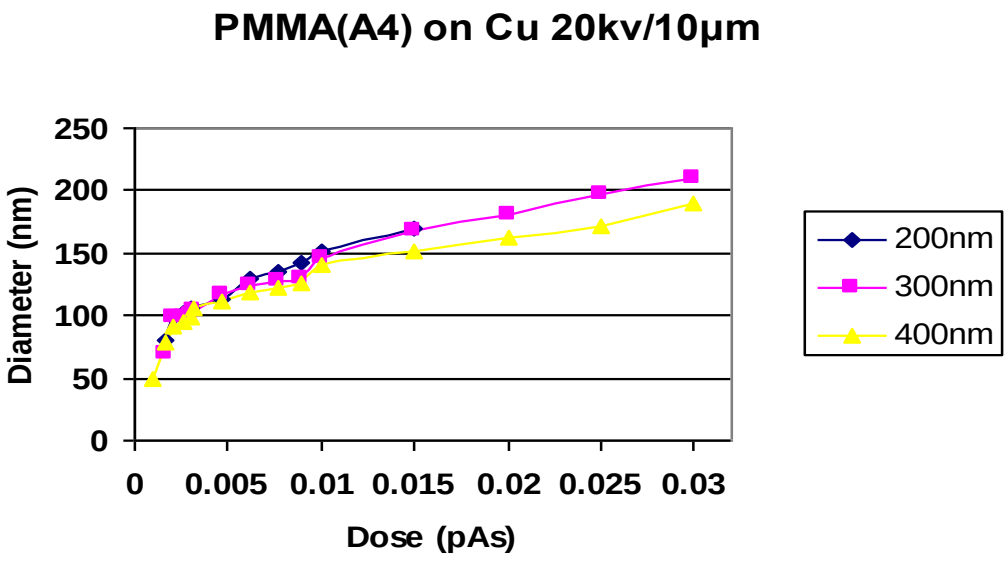

Fig. 3.16 Dose test results of PMMA (A4) by EBL

3.4 Thin film AAO templates

Because the electrical and structural properties of short, integrated nanowires are needed for several device applications, thin AAO templates (a few nanometers) will

play an important role in the future research. The AAO templates anodized by Al foil are not suitable for these applications because it is impossible to handle nanometer thick AAO templates. Thin AAO templates anodized from thin film Al on Si substrate show their advantage.

For the thin AAO templates on Si, removal of the barrier layer becomes a main problem. Normally, the barrier layer of AAO templates is removed by the chemical etching. An AAO template is immersed in 5 wt.% H_3PO_4 solution for couple of minutes depending on the thickness of barrier layer. But this method induces isotropic chemical etching of alumina. This method is not appropriate for applications in this project because the diameter of nanopore is widened during this process. Other methods have been developed to remove the barrier layer of thin AAO templates. Some people removed the barrier layer by gradually dropping the anodization voltage at the end of anodization process. (131) But, the barrier layer could not be removed completely by this method. Other electrochemical etch methods are also used to remove the barrier layer, for example, applying cathodic bias in a dilute KCl solution. (132) (133) (134) In this method, it is very important to know when Al is completely anodized. If the anodization time is not control accurately, a part of Al will remained on the top of bottom electrode. This could be a problem for electrodepositing nanowires due to the bad interfaces between nanowires and bottom electrode. This method is also not a good option for nanowire devices, because it is very hard to know when Al is completely anodized. In our experiments, thin AAO template is kept

a few seconds at the end of anodization process. When the anodization current starts increasing, it means the barriers have been removed.

Al thin films were deposited by evaporation under vacuum. Because evaporated Al thin film and Al foil have different fabrication processes, they have different properties, for example, grain size, stress distribution, and mechanical properties. All of these would affect the anodization procedure. It was necessary investigate the relation between the diameter of the nanopores and the anodization potential after first anodization and second anodization. The anodization conditions were in 1.5 M H_2SO_4 at 1 ^oC with anodization voltages varied from 6 V to 15 V. The diameters of the nanopores after the second anodizations are summarized in Fig. 3.17. The nanopore diameter increased slightly as the anodization potential was increased. The uniformity and the level of ordering of nanopores were much better after the second anodization. Meanwhile, the uniformity became better as the anodization voltage increased. In this research, an anodization voltage of 15 V was chosen for subsequent nanopore fabrication.

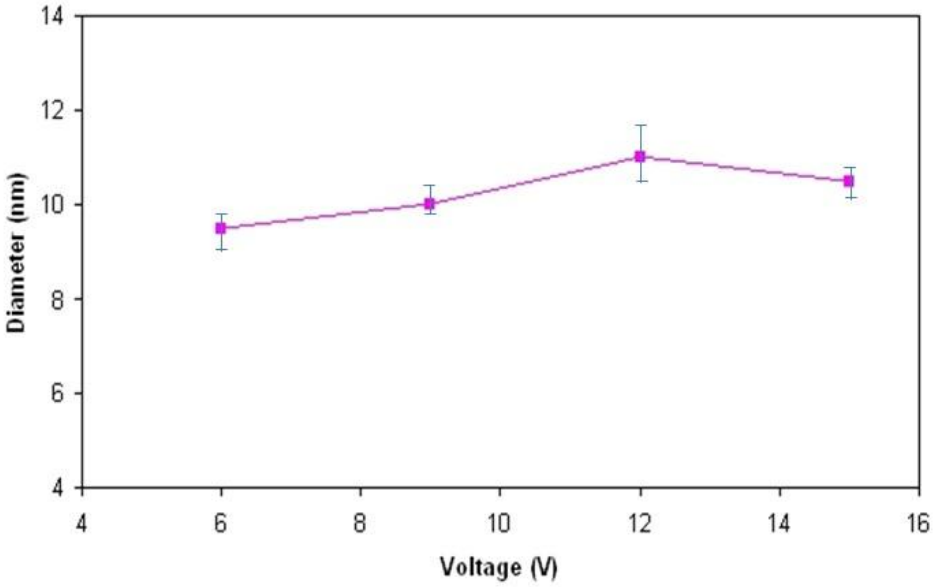

Fig. 3.17 Diameter of nanopore on Al thin film vs. anodization voltage

To make integrated nanowires using what was learned in the previous study, 200 μm Ti and 200 μm Cu films were coated on Si by sputtering,then, 1 μm thick Al thin films were evaporated. The anodization conditions were under 15 V in 1.5 M H_2SO_4 at 1 ^oC. First anodization process was set to 30 seconds. Unordered AAO nanopores were etched away by a mixture of 1.8 wt% Cr acid and 6 wt% H_3PO_4 at 60 ^oC for 20 minutes. Next, the Al thin film was anodized again under the same conditions. When anodization current started increasing dramatically, the anodization process was stopped. At this time, the Al thin film was completely anodized without peeling off, and the barrier layer was completely removed. After two-step anodization, a 600 nm thick AAO template with 10 nm diameter pores was fabricated as shown in Fig. 3.18.

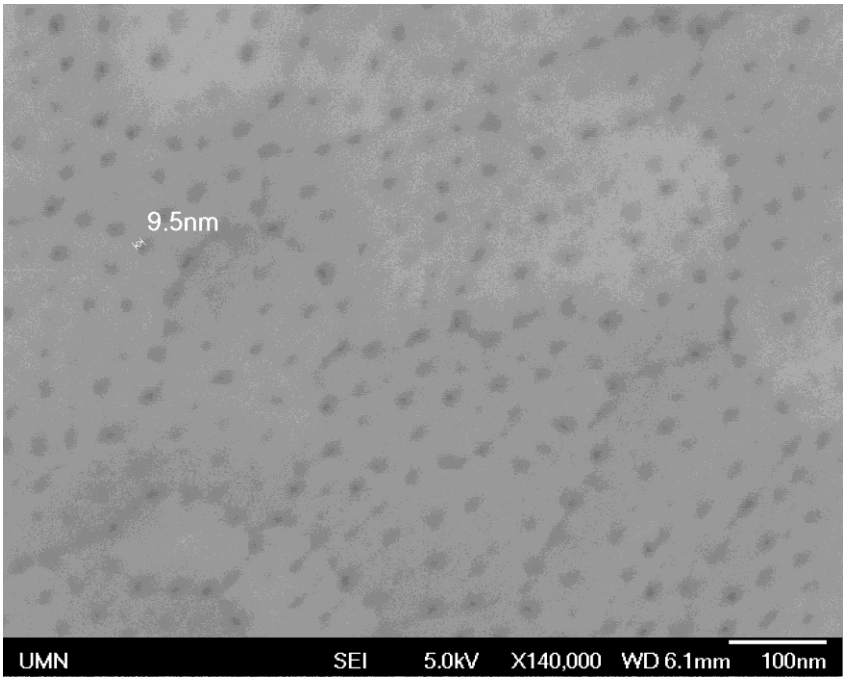

Fig. 3.18 AAO nanopore with 10 nm diameter on Si substrate

Then trilayer Co/Cu/Co nanowire was deposited into these integratednanopores by electroplating. The electrolyte was same as the solution discussed below for growing multilayered nanowires. Fig. 3.19 shows a nanowire that was grown out of the thin film AAO template. The mushroom-shaped cap is a Cu lead that was grown on the top of nanowire. The magnetic and magnetoelectronic properties of these trilayered nanowires are discussed in the next chapter, along with the properties of multilayered nanowires.

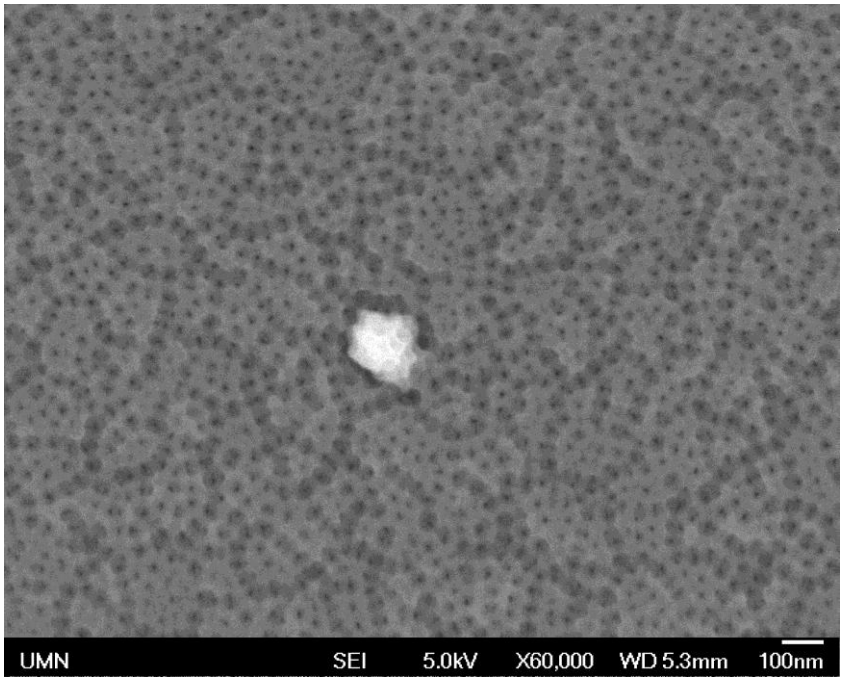

Fig.3.19 Single nanowire in thin film AAO template

3.5 Conclusions

Many types of templates were employed for the fabrication of nanowires by electrochemical deposition. E-beam lithography, nano-imprinted templates, and self-assembling templates (AAO) were explored to fabricate as small as possible nanopores for achieving nanowires with small diameters. Compared with other types of nanopores, AAO shows its advantage, for example, low cost, simple experimental setup. But most importantly, this research uncovered the optimized parameters required to reach the smallest diameter nanopores (≈ 10 nm). AAO templates can be fabricated from Al foil and Al thin film. The optimized conditions apply to long and short nanopores which will be of great benefit to potential application as devices in the future.

CHAPTER 4 Co/Cu NANOWIRES

In this research, 10nm diameter Co/Cu nanowires were electroplated into home-made AAO templates by using a single electrolyte. Multilayers were grown by switching the deposition potential. M-H hysteresis loops of these nanowires were characterized by VSM. The coercivity, remenance, and saturation field of multilayered Co/Cu nanowires were all dependent on the thicknesses of Cu layers and Co layers.

4.1 Fabrication of Multilayered Co/Cu nanowires

When the electroplating voltage is higher than ion's reduction potential, the ions start to will reduce to metal which deposits on the electrode. The reduction potentials of Co and Cu and -0.52V, respectively. Since Co and Cu ions have such different reduction potentials, multilayered Co/Cu nanowires can be easily deposited using different concentrations and then switching the deposition potential. Since Cu will deposit at -1V (below its reduction potential), its concentration was kept to 1% of the Co concentration to limit its contamination of the Co layers. Fig. 4.1 shows the electroplating process of 10 nm diameter multilayered Co/Cu nanowires into AAO templates. The growth rates of Co and Cu ions were 90 nm/s and 1 nm/s. The thickness of each layer (Co layers and Cu layers) can be adjusted by controlling deposition time. The electroplated multilayered nanowires clearly are shown in SEM (Fig. 4.2).

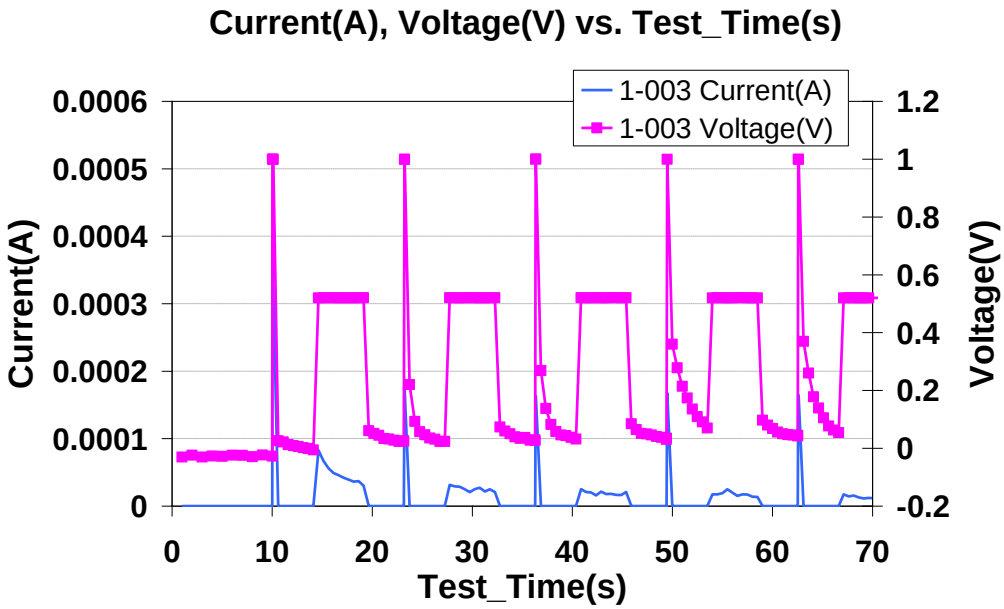

Fig.4.1 Multilayered Co/Cu nanowire electroplating process

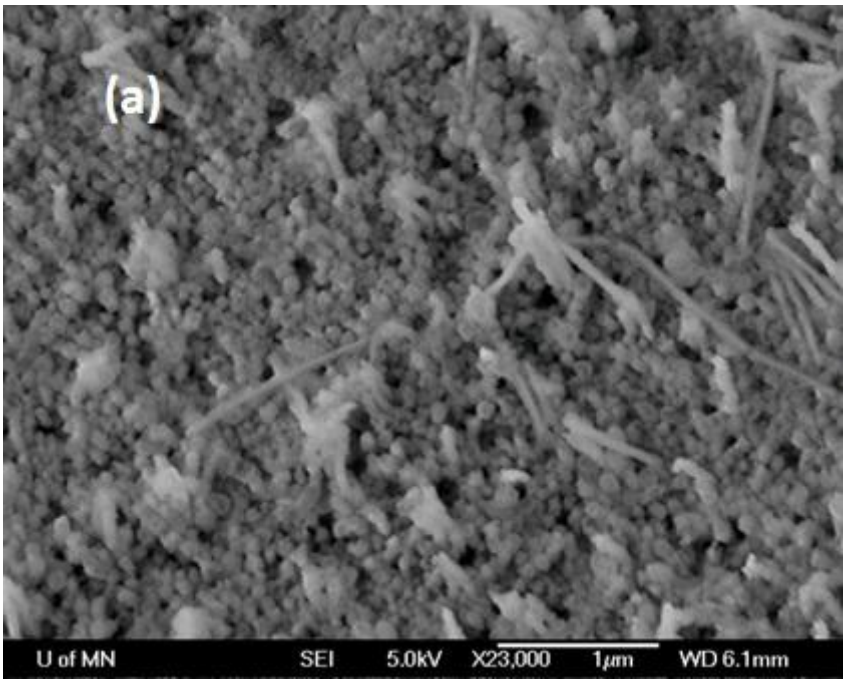

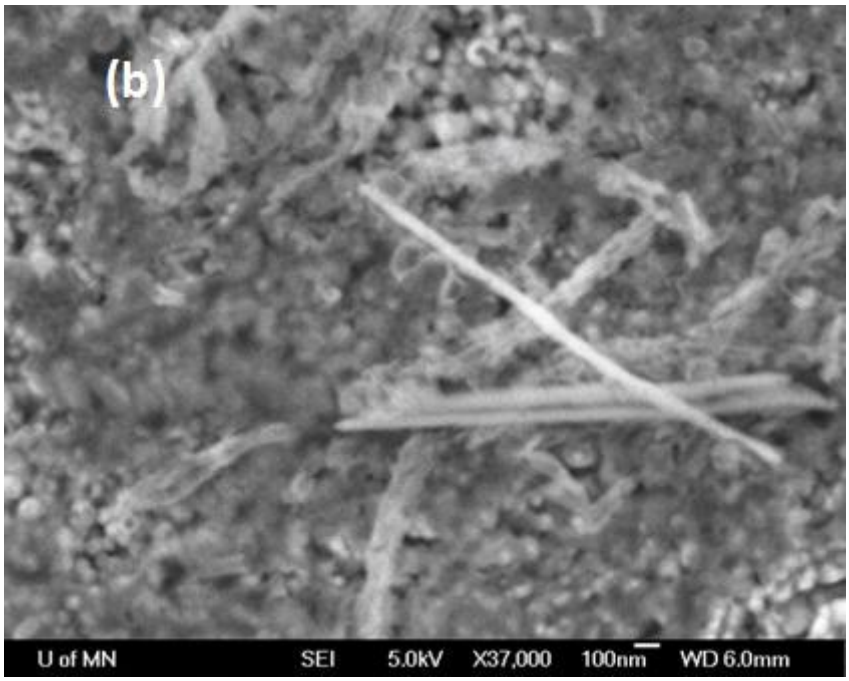

Fig. 4.2 SEM images of nanowire. (a) nanowires with the template etched partially; (b)single nanowire

4.2 Magnetic Properties of Multilayered Co/Cu nanowires

Fig. 4.3 shows the M-H loops of 300*[Co(27 nm)/Cu(X nm)] measured by VSM at room temperature. The Cu thickness was varied from 3 nm, 5 nm, to 11 nm respectively. The multilayered nanowires with 3 nm Cu were more easily saturated when the magnetic field was parallel to the nanowire axes. When the Cu thickness was increased to 5 nm, the multilayered nanowires showed isotropic magnetic properties. After the Cu thickness was increased to 11 nm, multilayer nanowires were more easily saturated when magnetic field was perpendicular to nanowire axis. Therefore, the anisotropy of the arrays changed from parallel to perpendicular to the wire axes as the Cu layer thicknesses were increased from 3 to 11 nm. The varied

magnetic anisotropies were due to the competition between shape anisotropy of each Co layer and magnetostatic interactions between the Co layers.

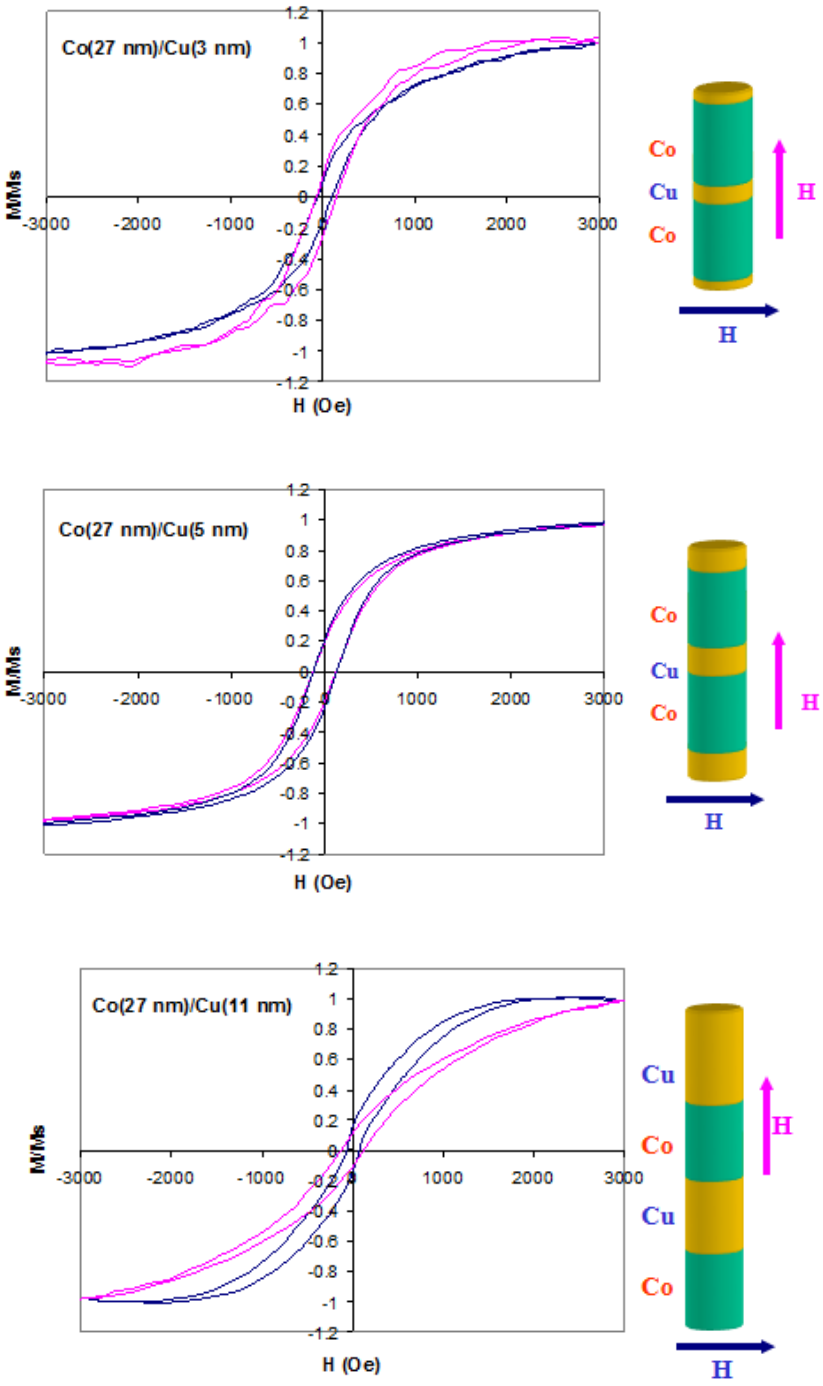

Fig.4.3 Hysteresis loops with 300*[Co(27 nm)/Cu(X nm)].

X=3 nm; b. X = 7nm; c. X=11 nm.

How does the Co thickness affect the M-H loops of multilayered magnetic nanowire arrays? Fig. 4.4 shows M-H loops when the Cu thickness was held constant (5 nm) and the Co thickness was varied from 9nm, 4.5 nm to 0.9 nm. When the thickness of Co was 4.5 nm and 9 nm, the multilayered nanowires were more easily saturated when the magnetic field was perpendicular to nanowire axis. This is due to the effect of shape anisotropy and crystalline anisotropy. As thickness of Co layer was smaller than nanowire diameter (10 nm), shape anisotropy dominated magnetization of Co layers to be in-plane. In previous chapter, it was mentioned that the crystalline anisotropy was in-plane for Co layers when multilayered Co/Cu nanowires were deposited in low pH electrolytes. The total effect of shape anisotropy and crystalline anisotropy can explain why the easy axis of multilayered Co/Cu nanowire was perpendicular to the nanowire axis. When the thickness of Co layers kept decreasing to 0.9 nm, multilayered Co/Cu nanowires showed isotropic M-H loops due to a lack of continuity in the Co layers. Co layers were so thin that they could not form an entire Co layer in nanowires.

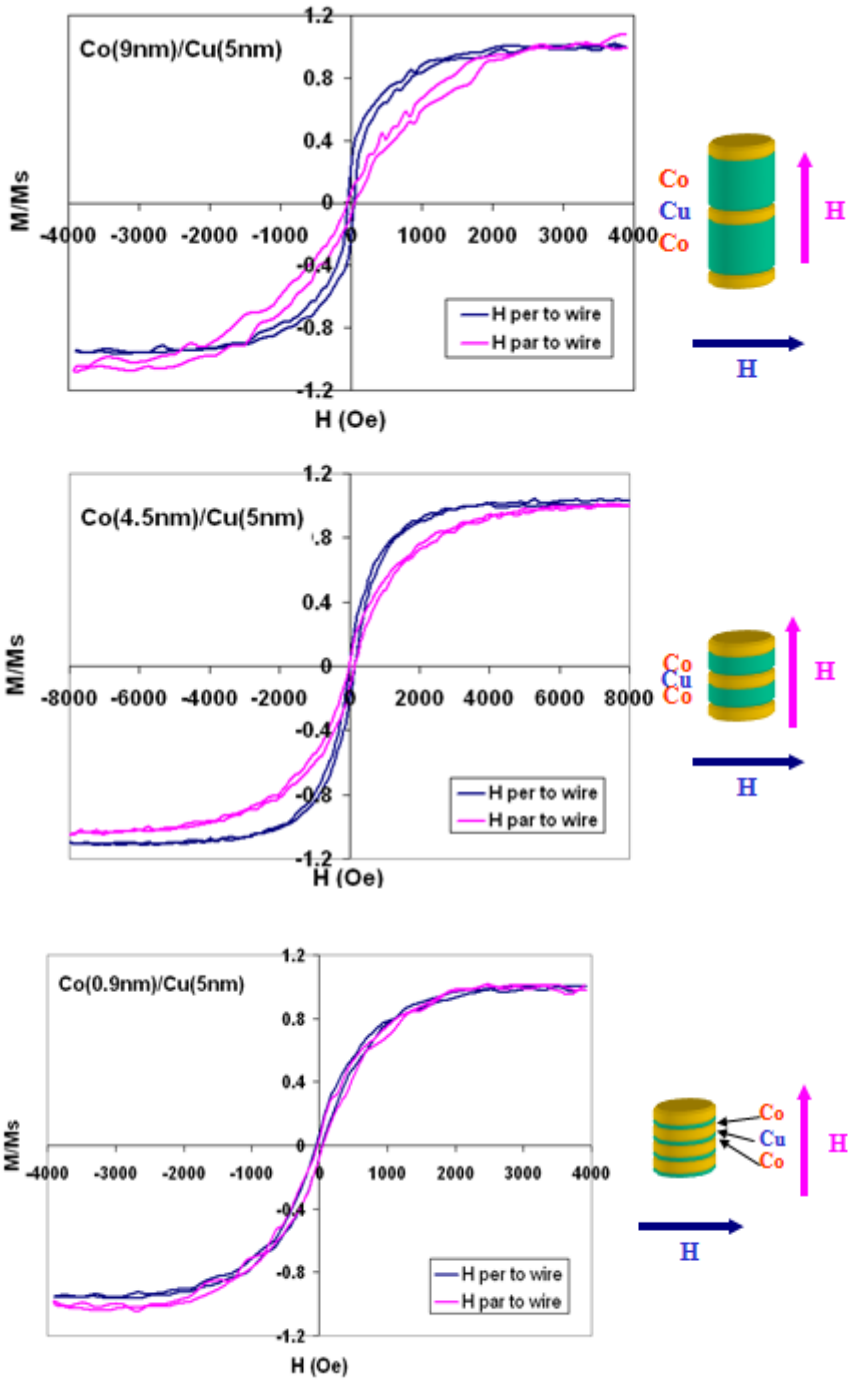

Fig.4.4 Hysteresis loops with 300*[Co (X nm)/Cu (5 nm)].

a. X=9 nm; b. X = 4.5 nm; c. X=0.9 nm.

4.3 Conclusions

Co/Cu multilayered nanowires with 10nm diameter were successfully grown into AAO templates by electrochemical deposition. The magnetic anisotropy of arrays of Co/Cu nanowire was changed by varying the thickness of Co and Cu layers. When the thickness of Cu increased, the easy axis of the arrays switched from out-of plane to in-plane. When Cu thickness was 5 nm and Co thickness kept decreasing, the easy axis of nanowire remained in-plane. However, when Co thickness was smaller than 1 nm, the Co layer appeared to be discontinuous because the nanowire arrays had isotropic magnetic properties.

CHAPTER 5 MAGNETO TRANSPORT PROPERTIES OF MANETIC NANOWIRE ARRAYS

5.1 Giant Magnetoresistance (GMR) of Co/Cu Nanowires with 10 nm Diameter

A PPMS (Physical Property Measurement System) from Quantum Design was used to measure magnetotransfer curve from 2 K to 300 K. The system working frequency of AC current was 413 Hz. The excitation current range was 0.01 mA to 0.5 mA. The contact method used was quasi-four-terminal. A sample rotation stage was available with a range of 180 degrees, and this was used to adjust an angle between current and magnetic field.

During the measurement process, a current passed between two leads bonded to the nanowire samples. Two leads were used to measure the potential drop across the nanowire samples. The effects of the leads and contact resistance can be eliminated by this method. In this study, Au wires were used as the leads and Ag epoxy was used to bond Au wires on the nanowire samples since Ag epoxy works very well in a large range of temperatures. (113)

The resistances vs. H of Co/Cu multilayered nanowires with 10 nm diameters at 150 K, 200 K, and 300 K are shown in Fig. 5.1. The nanowires were at low resistance states when they were completely saturated at high positive or negative magnetic fields. The measurements were done with an applied filed either perpendicular or

parallel to nanowire axis. As the temperature increased from 150 K to 300 K, the resistance at H=0 (Oe) increased from 3.7 Ω to 4.63 Ω. This is due to Mattheisen's rule which describes the resistance of metals increasing with temperatures as the number of collisions between electrons and phonons increases. Also, the number of collision between electrons and magnons increases with temperature. Both of these scattering effects lead to the easy spin-flipping of magnetization of Co layers, so the GMR ratio of an array of nanowires will decrease at high temperatures.

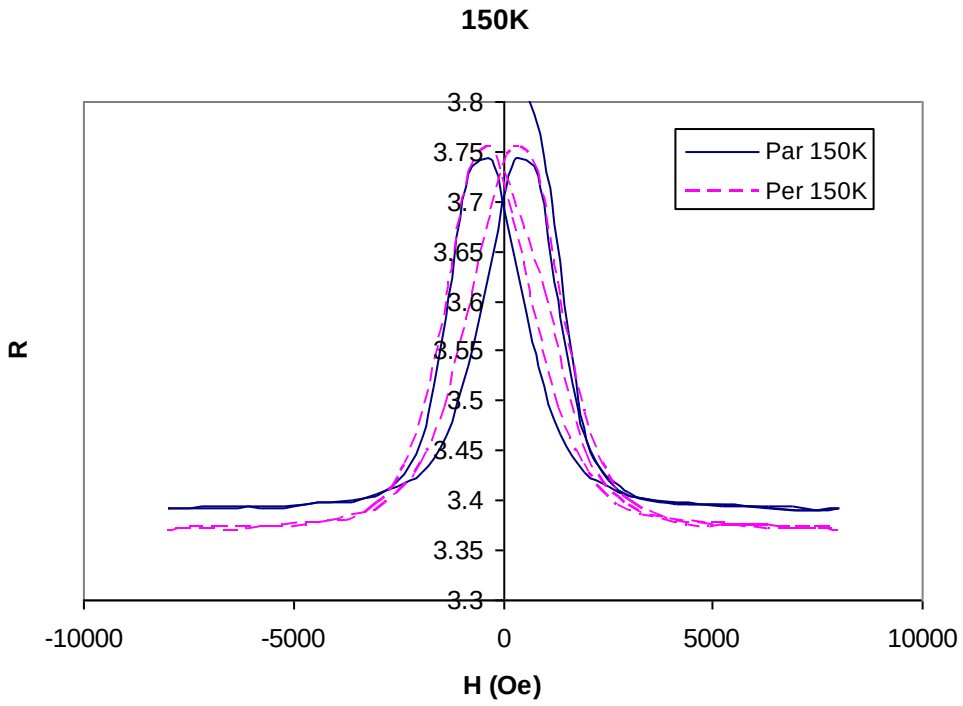

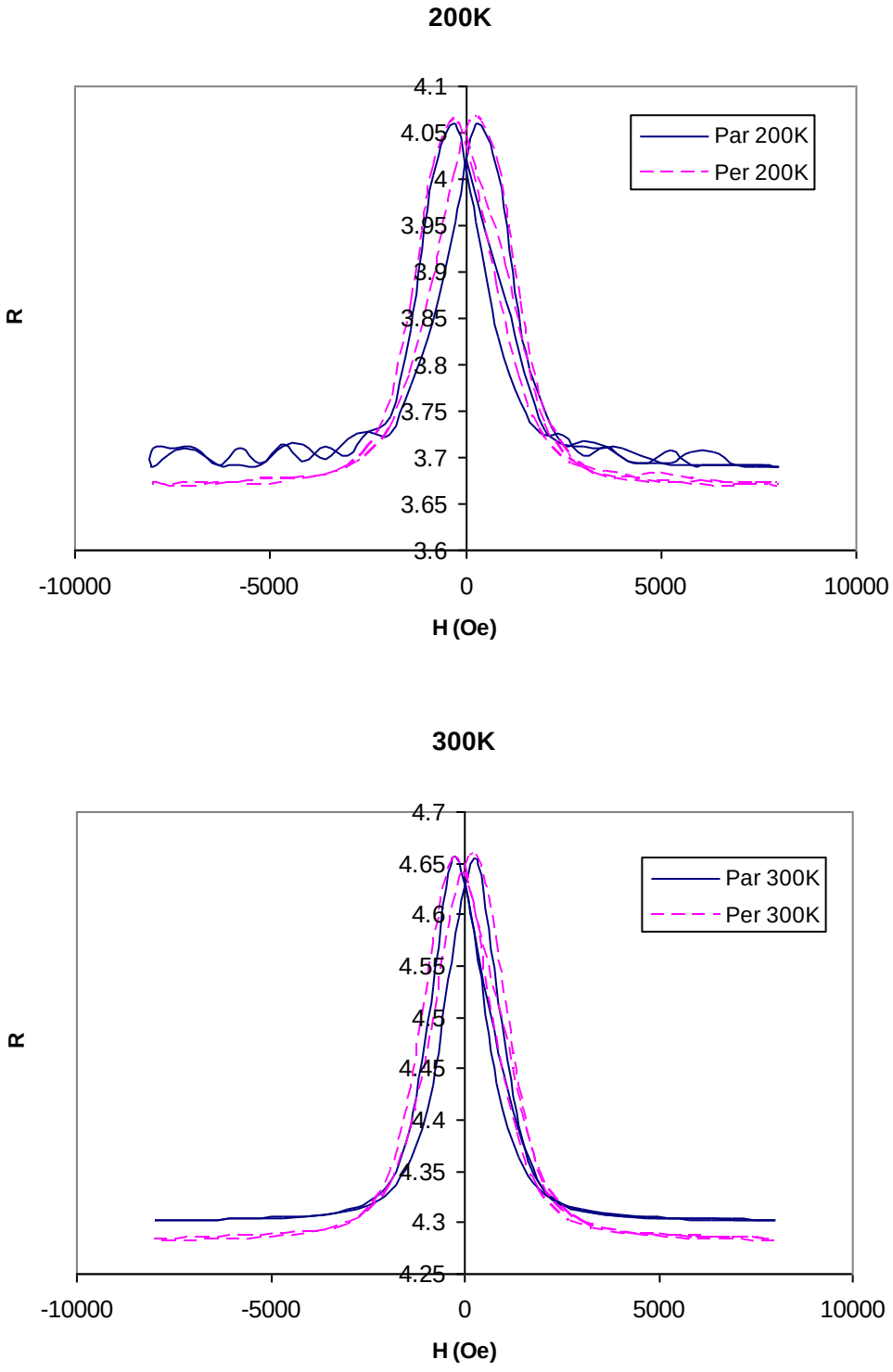

Fig. 5.1. R vs. H of 300x[Co(27 nm)/Cu(5 nm)] at 150K, 200K, and 300K.

The magnetoresistance of nanowires of 300x[Co(27 nm)/Cu(5 nm] are shown in Fig. 5.2. Multilayered Co/Cu nanowires had high GMR when the applied magnetic field was perpendicular to the nanowire axis. Again, GMR ratios at low temperatures were higher than that at high temperatures. GMR ratios of 9% and 8.2% was achieved in this study, but with the nanowires were grown with Cu leads on each end to ensure the multilayers were in the center of the nanopores. The lead resistance is subtracted and shown in Fig. 5.3

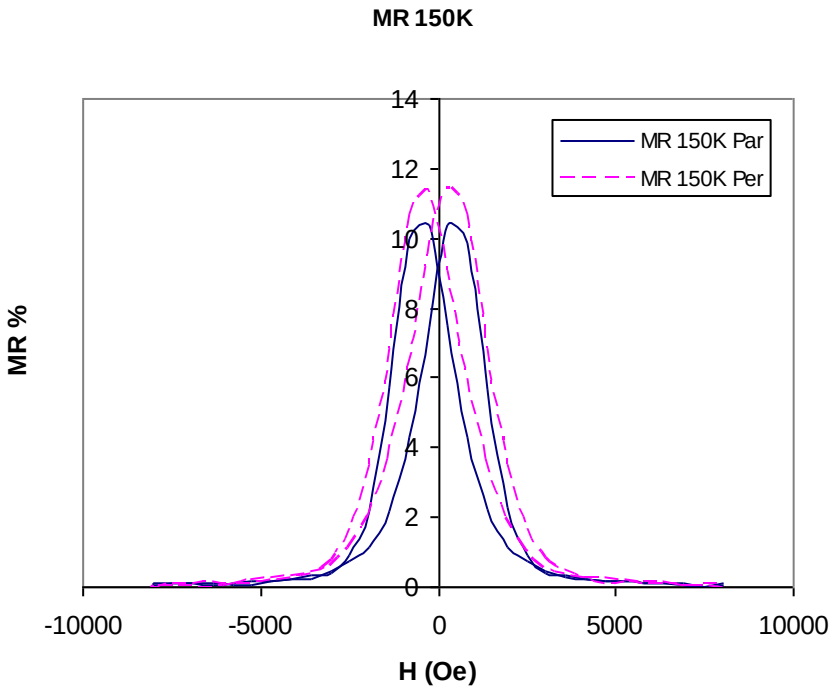

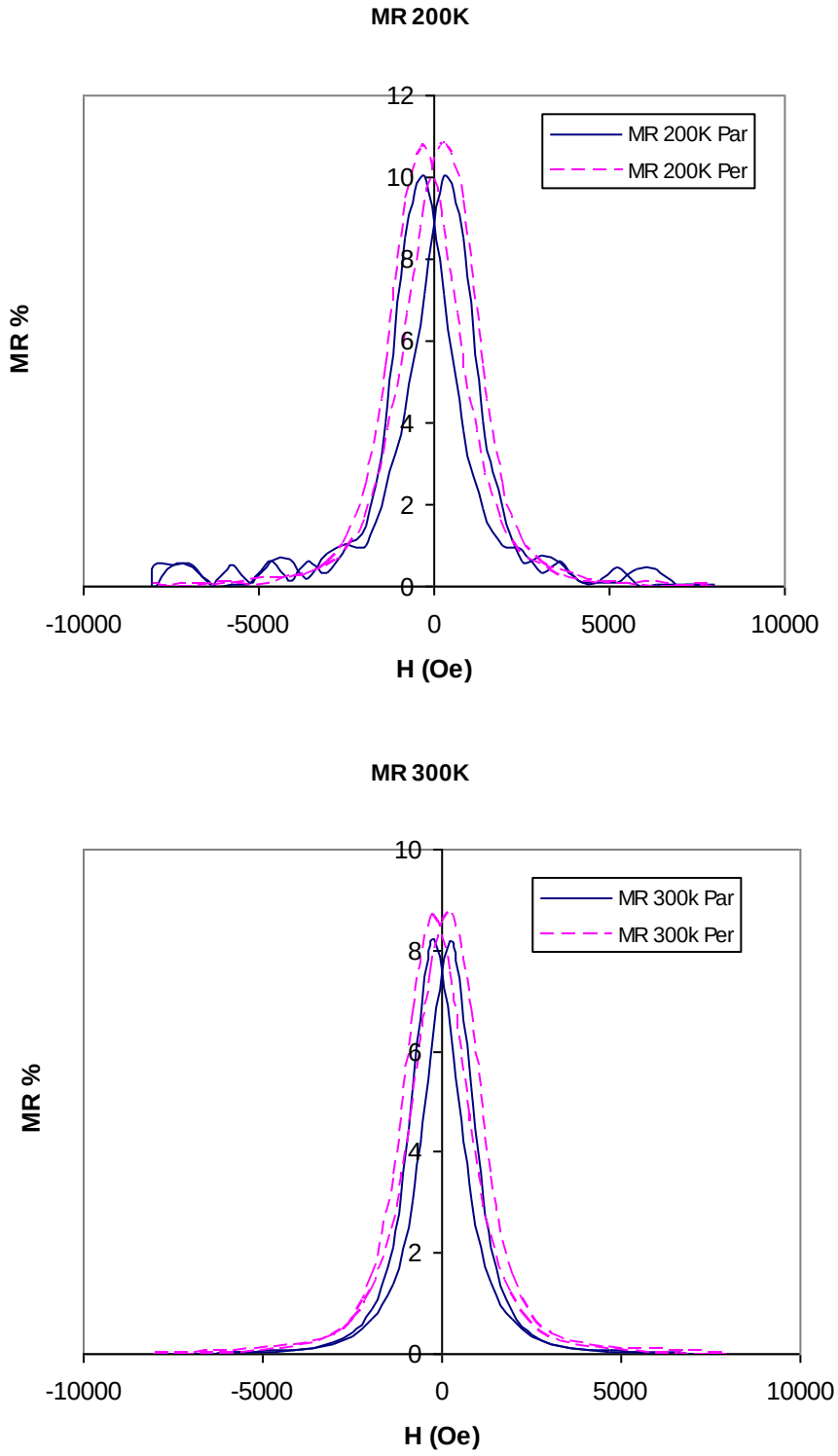

Fig. 5.2. GMR of 300x[Co(27 nm)/Cu(5 nm)] at 150 K, 200 K, and 300 K.

These results show that multilayered nanowires (300 bilayers) with thick Co layers (27 nm) had high magnetoresistance (MR). (31) Some researchers have found that 10 nm Cu thicknesses yields the maximum values of MR for thicker nanowires (30 - 60nm diameters), (72) (27) however, this study focused on obtaining thin structures for minimum shield-shield spacing which is desired for read sensors. It was found that MR in these 10 nm diameter wires was substantially larger if using 5 nm Cu spacers than other thicknesses as shown in Fig. 5.3. Note that the lead resistances have been subtracted from these values, and the measurements were made at 150 K in order to measure MR in all of the samples. At 300 K, the multilayered structure of (27nm Co/ 5nm Cu) x300 had 19% MR.

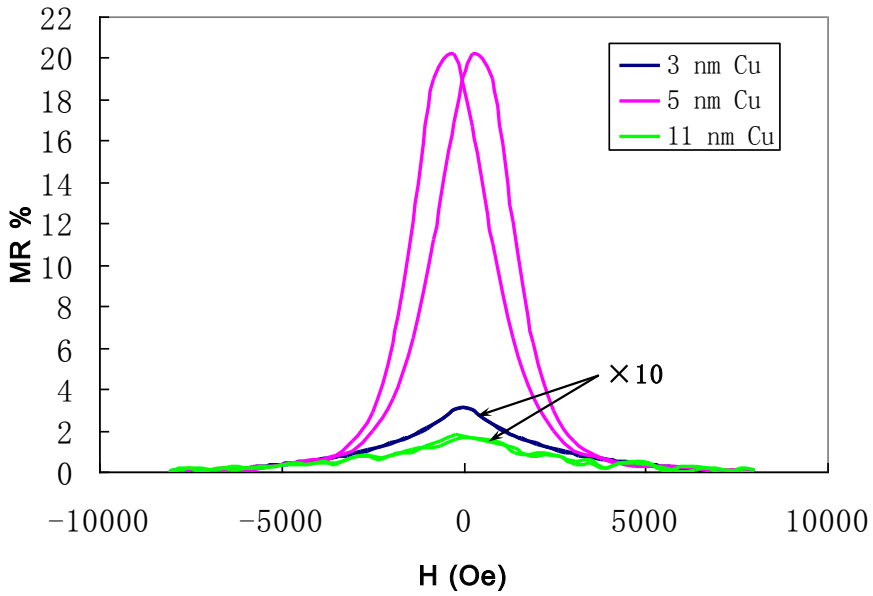

Fig. 5.3. MR of 10 nm diameter, multilayered nanowires with 27 nm Co and various Cu spacer layers.

To further reduce the sensor size, a multilayered nanowire study was again conducted to determine the optimal tradeoff between the thickness of the magnetic layers (t_{Co}) and the magnetoresistance. GMR of 13% was found at 12 nm Co, after which MR decreased to be negligible at 1 nm Co. A favorably small structure was reached with 4.5 nm Co with 11% MR, as shown in Fig. 5.4. This MR is four fold that of thin-film CPP GMR structures with similar magnetic thicknesses, (135) but has 10x less RA product (shown in next chapter) as incorporated into a read sensor without nanoleads.

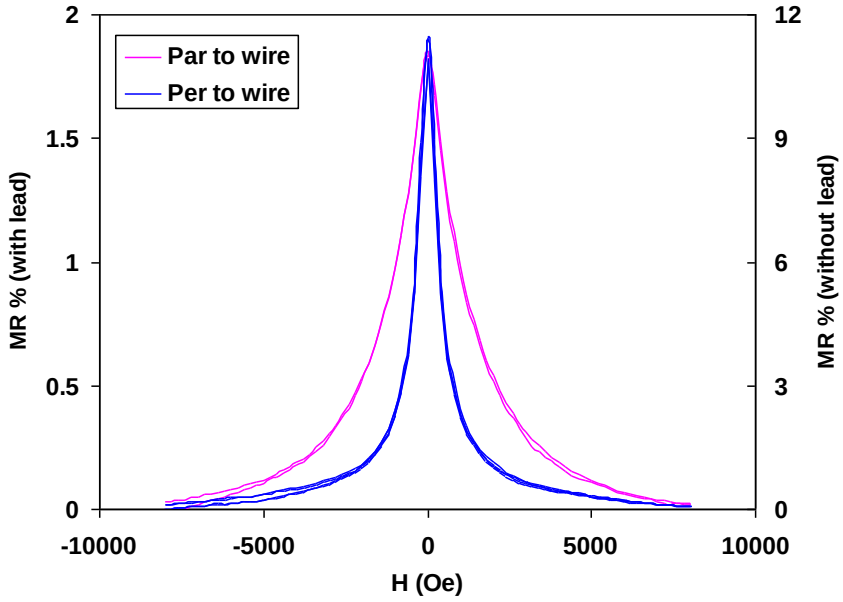

Fig. 5.4. Room temperature MR of 10 nm diameter nanowires with 4.5 nm Co/ 5nm Cu.

5.2 Spin Transfer Torque (STT) Switching in Co/Cu nanowire

5.2.1 STT switching in trilayered Co/Cu nanowire

STT switching of the electrodeposited nanowires investigated by other groups was mainly focused on multilayered Co/Cu structures or multilayered Co/Cu/Cu separated

by thick Cu layers. The STT switching data did not show switching properties of a single Co layer. In this research, 10 nm diameter trilayer Co/Cu/Co nanowires were fabricated in 700 nm thick AAO templates on Si substrates. Conductive AFM tips were used to probe as few nanowires as possible and to achieve sufficient current densities to switch the magnetization of Co layers.

A single electro-deposition bath was again used to electroplate these trilayers at room temperature. Fig. 5.5 shows the STT switching measurement setup. An external magnetic field was applied along perpendicular direction to nanowire axis to cause the magnetization switching of the free layers.

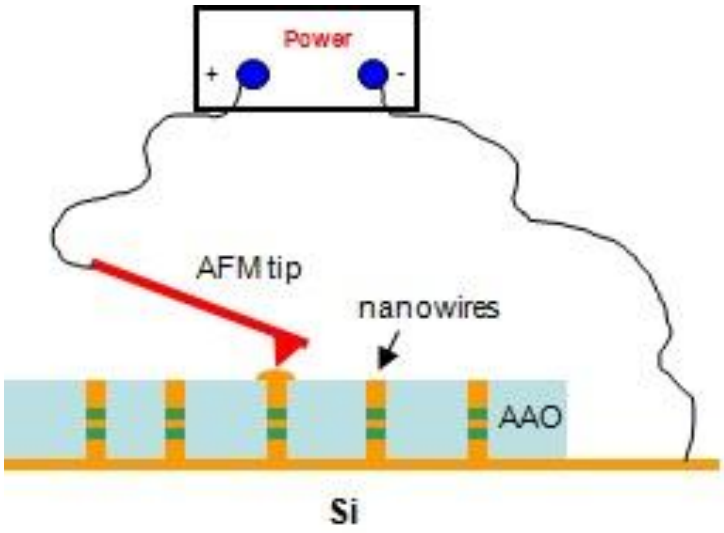

Fig. 5.5. Co/Cu/Co nanowires STT switching measurement setup

The STT switching experimental results are presented in Fig. 5.6. The magnetizations of the two Co layers were anti-parallel at all currents when a 65 Oe field was applied. The total energy of STT switching and the external field was

smaller than the magneto-static energy between two Co layers, as shown in Fig. 5.6 (a). The resistance of the nanowires was 8 Ω at this state. After H was increased to 130 Oe, STT switching was observed as shown in Fig. 5.6 (b). The switching current densities (J_{AP-P}/J_{P-AP}) were 4.85x 10^8 A/cm^2 and -4.9 x 10^8 A/cm^2 respectively. As H was increased to 250 Oe, J_{AP-P} increased to 5.0 x 10^8 A/cm^2, and J_{P-AP} decreased to -4.7 x 10^8 A/cm^2.

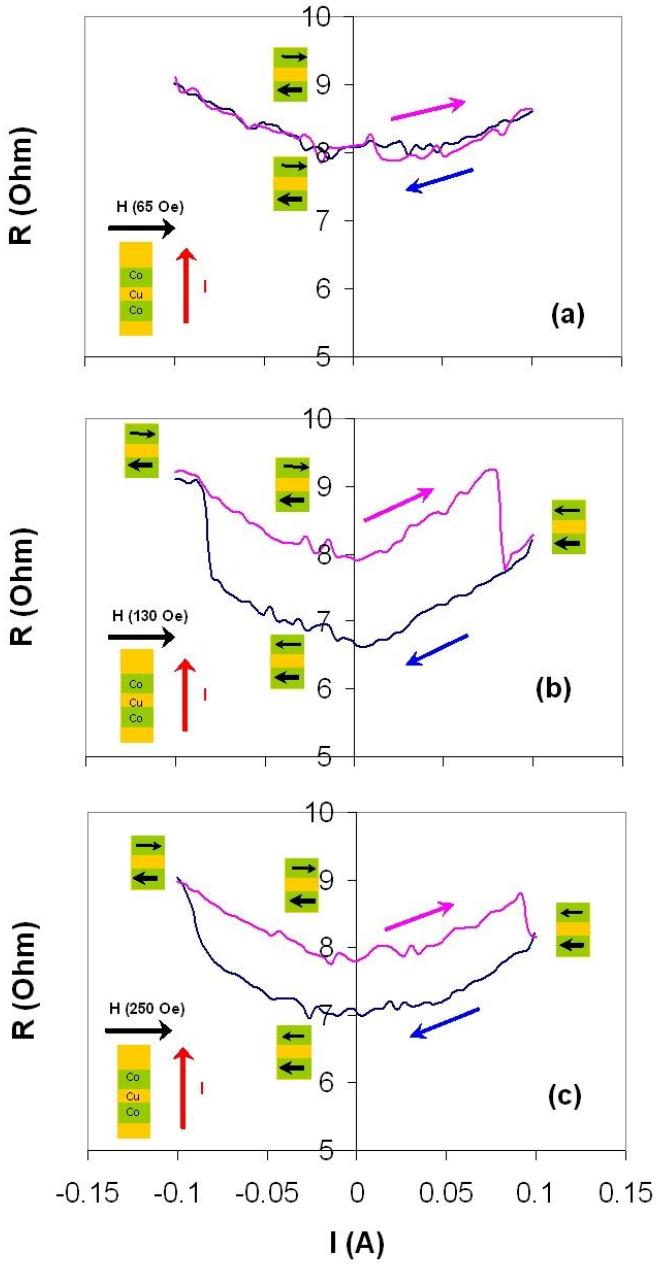

Fig. 5.6. STT switching of Co/Cu/Co nanowires under different applied magnetic fields.(a) H=65 Oe; (b) H=130 Oe; (c) H=250 Oe.

The magnetoresistance was calculated to be 17.6% after the lead resistance was subtracted. This GMR ratio is high enough for applications such as sensors or memories. In order to study the reproducibility of switching, the trilayered nanowire was measured numerous times. Fig. 5.7 (a) shows spin transfer curves when the

current flowed from positive to negative direction. The magnetization of the free layer switched from a parallel state to an anti-parallel state (P→AP) compared to the fixed layer. The critical switching current density ($J_{P\text{-}AP}$) was very reproducible, as seen. The average of $J_{P\text{-}AP}$ was –4.9 x 10^8 A/cm^2. As the free layer switched from anti-parallel to parallel (AP→P) to the fixed layer, $J_{AP\text{-}P}$ was observed to be exactly the same each cycle as shown in Fig. 5.7 (b). The $J_{AP\text{-}P}$ was 4.85 x 10^8 A/cm^2. Compared with the range of $J_{P\text{-}AP}$, the distribution of $J_{AP\text{-}P}$ was neglible. The standard distribution of $J_{P\text{-}AP}$ was 11.5%. However the standard distribution of $J_{AP\text{-}P}$ was only 0.014%. This asymmetrical switching phenomenon indicates that there were several energy barriers in trilayer Co/Cu/Co nanowires.

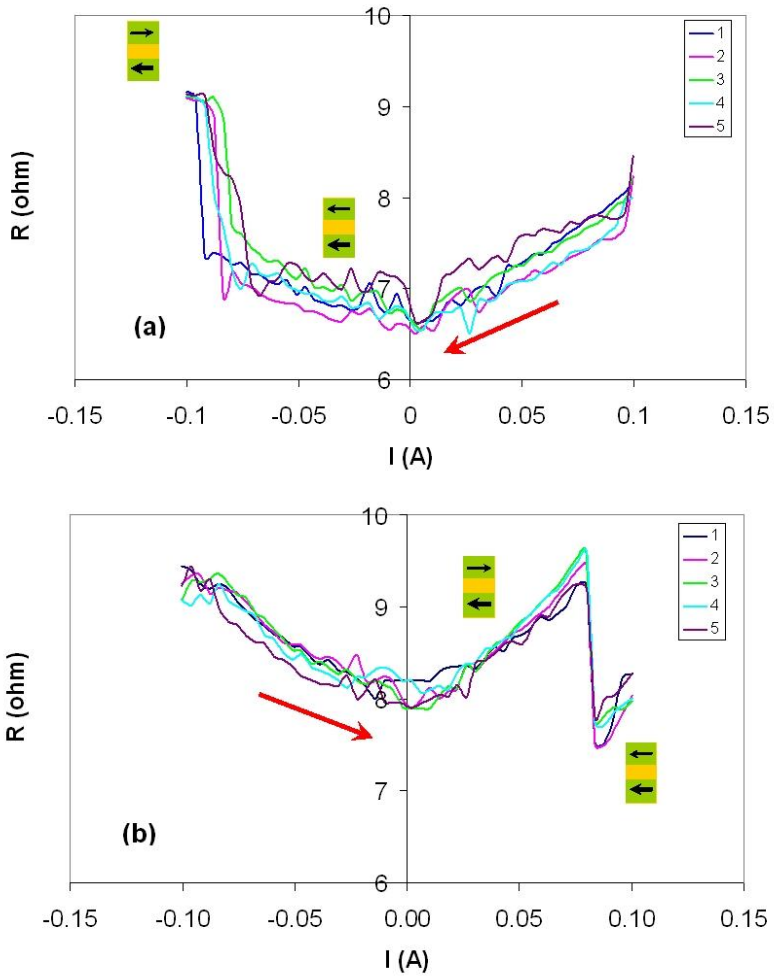

Fig. 5.7. Resistance vs current in the Co/Cu/Co nanowire as H=130 Oe. The critical current density was measured numerous times. (a) current flowing from positive to negative direction; (b) current flowing from negative to positive direction.

Since the area of the probe was 0.02 μm^2, 50 nanowires were contacted with the AFM tip in parallel for this measurement, which led to a total (wires and matrix) RA product of 0.16 $\Omega\mu m^2$ and a ΔRA = 0.033 Ω. This value will decrease when device structures (30 nm long) are grown between shield films without leads. The resistance of each trilayer structure alone (without leads or matrix) was extrapolated

to be 35 - 45 Ω. For a 10 nm diameter device, this will lead to a RA product of 0.003 Ωum^2.

5.2.2 STT switching in multilayered Co/Cu nanowire

The resistance and contact area for the 10 nm diameter nanowires were determined by varying the pressure on the contact probe. The STT switching curves were noisy with some jumps. Small jumps (1% – 2%) were likely due to individual layers flipping, and larger jumps (6.25%) were due to collective spin flipping between interacting Co layers (Fig. 5.8). For nanowires with larger diameter, the individual spin flips were not present, and the curves were similar to typical STT switching results. Similar as in the first electroplated GMR nanowires, (72) these nanowires exhibit antiferromagnetic coupling from magneto-statics as $t_{Cu} > 3$ nm (98). A critical current of 1.9 mA ($J_{AP\text{-}P}$=2.7x10^7 A/cm^2) transferred the STT from the layers aligned with the applied field to the layers antiparallel to it. For nanowires with small diameter, the antiferromagnetic coupling was strong, and the resistance went back to the initial value at a positive 0.8 mA ($J_{P\text{-}AP}$=1.3x10^7 A/cm^2).

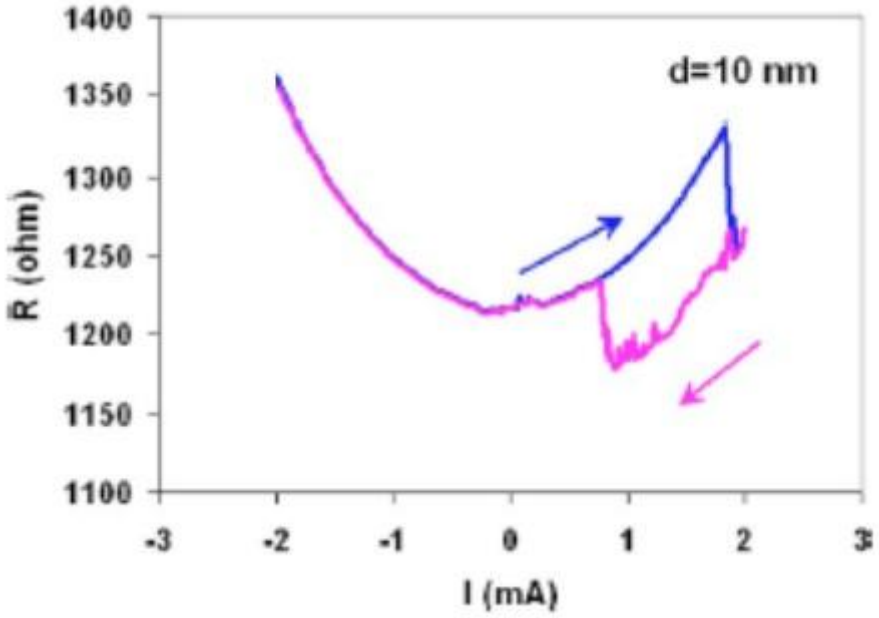

Figure 5.8. Resistance vs current for 10 nm diameter nanowires,

Figure 5.8 shows resistance jump (6.5%) for the 10 nm nanowires which less than that (11%) was shown in previous chapters, indicating that not all of the antiparallel layers switched. The 1 – 2% jumps were always shown in the curves from positive to negative current, which was due to spin flips in intermediate layers. Switching of layers located in the center of a "domain" of parallel layers caused positive R jumps, but when domains grew together to annihilate antiparallel nearest neighbors, R jumps became negative. Such effect on nanowires with small diameters is to be investigated in order to obtain STT switching similar to that on 60 nm diameter wires, which is very promising for high density device arrays.

5.3 Conclusions

Giant magnetoresistance was measured in multilayered Co/Cu nanowires with 10 nm diameter. The highest GMR ratio was 19.5% using 300x[Co(27 nm)/Cu(5 nm] nanowires after the lead resistance was subtracted. When the thickness of Co layer was only 4.5 nm, GMR of nanowires was as high as 11%. These thin layers are promising for future read heads as shield to shield spacing must be very small.

STT switching was successfully measured on trilayered and multilayered Co/Cu nanowires with 10 nm diameter. The critical current density to switch the direction of magnetization was 10^8 A/cm^2 in trilayered Co/Cu nanowires. For multilayered Co/Cu nanowires, the critical current density was 10^7 A/cm^2. The critical switching current is related to deposition conditions. A total RA product is 0.16 Ωum^2 and a ΔRA is 0.033Ω. Since these nanowires had 10 times smaller area than thin film GMR structures, their RA products are extremely small 3mΩ/um^2 while maintaining 20Ω total resistance for 30nm thick structures These are very promising for next generation read heads. On the other hand, multilayered structures can be designed with low critical current densities while maintaining high device density and high MR for applications in STT-RAM.

CHAPTER 6 SUMMARY AND FUTURE WORK

Magnetic nanowires with small diameters have gained a great deal of interest in recent years due to their potentials on fundamental research and real applications, especially in small size magnetic sensors, high density magnetic recording media, and STT switching -MRAM.

Co/Cu nanowires with 10 nm diameter were successfully deposited into AAO templates by the electrochemical deposition method. This technique can efficiently grow high density and uniform magnetic nanowires with low costs and equipment requirements. In order to form ordered nanopores, two-step anodization was employed to fabricate AAO templates using Al foils and Al thin films on Si substrates. Compared with other techniques such as nano-imprinting or ebeam with PMMA, Al anodization can easily fabricate nanopore templates with larger areas and smaller diameter pores. It was found that the extremely small nanopores (diameter < 10 nm) could be fabricated in 1.5 M H_2SO_4 at an anodization potential of 15 V. The hysteresis loops of nanowires could be varied controllably using Cu and Co layer thicknesses. By varying the thickness of the Cu layers, the direction of anisotropy could be controlled due to the interaction between layers in each nanowire and also between neighboring nanowires. CPP-GMR of 19% was found in multilayered Co (27 nm)/Cu(5 nm) nanowire array. GMR of 11% was obtained from Co (4.5 nm)/Cu(5 nm) nanowires. Meanwhile, the RA product was only 0.16 Ωum^2 and a ΔRA =

0.033Ω. Such findings can be potentially applied in high density CPP-GMR reader for Terrabit/in^2 media in the future. STT switching was successfully measured on trilayered and multilayered Co/Cu nanowires with 10 nm diameter. The critical current density to switch the direction of magnetization was 10^8 A/cm^2 in trilayered Co/Cu nanowires and 10^7 A/cm^2 in multilayered Co/Cu nanowires, which demonstrates the potential application of nanowires in STT switching -MRAM.

Even though nanowires with small diameter have many good magnetic properties, more investigations have to be carried out. First, the effect of surface boundary of nanowires on magnetic properties is not clear as the nanowire diameter keeps decreasing. Both micro-magnetic simulation and experiments are needed for a deep understanding. Second, nanowires were deposited from a single electrolyte, it is essential to study the interface between Co layers and Cu layers which affects the magnetic properties of nanowires. Third, magnetic nanowires with different Co thickness show potential applications as multi-state STT switching -MRAM. If this were successful, single nanowires can be used to record information more densly as a new generation of STT switching -MRAM.

References:

1. **M.N.Baibich, J.M.Broto, A.Fert, F. Nguye Van Dau, F.Petroff, P.Etienne, G.Creuzet, A.Friederich and J. Chazelas.** *Phys.Rev.Let.* 1988, Vol. 61, 2472.

2. **S.Parkin, N.More,and K.P.Roche.** *Phys. Rev. Lett.* 1990, Vol. 64, 2304.

3. **A.Barthelemy, V.Cros, J.L. Duvail, A. Fert, R. Morel, F. Parent, F. Petroff, and L. B. Steren.** *Nanostructured Materials.* 1998, Vol. 6, 217.

4. **F.Spizzo, C.Ferrero, A.Mazuelas, F. Albertini, F. Casoli, L. Nasi, F. Ronconi, and T. H. Metzger.** *J.Appl.Phys.* 2009, Vol. 105, 123533.

5. **B. Dieny, V. S. Speriosu, B. A. Gurneyand, S. P. Parkin, D. R. Willhoit, S. Metin.** *J. Magn. Magn. Mater.* 1991, Vol. 93, 101.

6. **B. Dieny, V. S. Sperisu, S. Metin, S. P. Parkin, B. A. Gurney, and D. R. Willhoit.** *J. Appl. Phys.* 1991, Vol. 69, 4774.

7. **T.Shinjo, and H.Yamamoto.** *J. Phys. Soc.Japan.* 1990, Vol. 59, 3061.

8. **K.Nakamoto, H. Hochiya, H. Katada, K. Hoshino, N. Yoshida, H.Takei, M. Shiimoto, M. Hatatani, K. Watanabe,.** *IEEE Trans. Magn.* 2008, Vol. 44, 95.

9. **K.Nakamonto, H.Hoshiya, H. Katada, T. Okada, M. Hatatani, K. Hoshino, N. Yoshida, I. Nunokawa, K. Etoh, and K. Watanable.** *IEEE Trans. Magn.* 2005, Vol. 41, 2914.

10. **X.Peng, P. Kolbo, K. Nikolaev, S. Chen, Z. Wang.** *J. Magn. Magn. Mater.* 2009, Vol. 321, 1889.

11. **M., Julliere.** *Phys. Lett. A.* 1975, Vol. 54, 225.

12. **T.Miyazaki, N.Tezuka.** *J.Magn.Magn.Mater.* 1995, Vol. 139, L231.

13. **S.S.P.Parking.** *Nature Mater.* 2004, Vol. 3, 862.

14. **D.D.Djayaprawira, K.Tsunekawa,M.Nagai,.** *Appl.Phys.Lett.* 2005, Vol. 86, 092502.

15. **S.Lkeda, J.Hayakawa,Y.Ashizawa,Y.M.Lee.** *Appl.Phys.Lett.* 2008, Vol. 93, 082508.

16. **S.Mao.** *IEEE Tran. Magn.* 2006, Vol. 42, 97.

17. **D.C.Ralph, M.D.Stiles,.** *J.Magn.Magn.Mater.* 2008, Vol. 320, 1190.

18. **E.B.Myers, D.C.Ralph, J.A.Katine, R.N.Louie, and R.A.Buhrman,.** *Science.* 1999, Vol. 285, 867.

19. **M.Tsoi, A.G.M.Jansen,J.Bass, W.C.Chiang, M.Seck, V.Tsoi, P.Wyder.** *Phys.Rev.Lett.* 1998, Vol. 80, 4281.

20. **T.Seki, S.Mitani,K.Yakushiji,and K.Takanashi.** *Appl.Phys.Lett.* 2006, Vol. 89, 172504.

21. **J.Hayakawa, S.Ikeda, Y.M.Lee, R.Sasaki, T.Meguro, F.Matsukura, H.Takahashi, H.Ohno.** *Jpn.J.Appl.Phys.* 2005, Vol. 44, L1267.

22. **B.Doudin, A.Blondeland, and J.P.Ansermet.** *J.Appl.Phys.* 1996, Vol. 79, 6090.

23. **A.Blondel, J.P.Meier, and B.Doudin,.** *Appl.Phys.Lett.* 1994, Vol. 79, 6090.

24. **K.Liu, K.Nagodawithana,P.C.Searson,and C.L.Chien.** *Phys.Rev.B.* 1995, Vol. 51, 7381.

25. **L.Piraux, M.J.George, F.J.Despres, C.Leroy, E.Ferain, R.Legras, K.Ounadjela, and A.Fert.** *Appl.Phys.Lett.* 1994, Vol. 65, 2484.

26. **P.R.Evans, G.Yi,W.Schwarzache.** *Appl.Phys.Lett.* 2000, Vol. 76, 481.

27. **T.Ohgai, X.Hoffer,L.Gravier,J.E.Wegrowel,and J.P.Ansermet.** *Nanotech.* 2003, Vol. 14, 978.

28. **S.Dubois, J.M.Beuken,L.Piraux,J.L.Duvail,A.Fert,J.M.George,and J.L.Maurice.** *J.Magn.Magn.Mater.* 1997, Vol. 165, 33.

29. **X.T.Tang, G.C.Wang,and M.Shima.** *Phys.Rev.B.* 2007, Vol. 75, 134404.

30. **H.Masuda, and K.Fukuda.** *Science.* 1995, Vol. 268, 1466.

31. **H.Masuda, and M.Satoh,.** *Jpn.J.Appl.Phys.* 1996, Vol. 35, L126.

32. **W.Lee, R.Ji,U.Gosele,and K.Nielsch.** *Nature Materials.* 2006, Vol. 5, 741.

33. **T.Ohgai, X.Hoffer,L.Gravier,and J.P.Ansermet.** *J.Appl.Electrochem.* 2004, Vol. 34, 1007.

34. **Y.Peng, T.Cullis,G.Mobus,X.Xiaojing,and b.Inkson.** *Nanotech.* 2007, Vol. 18, 485704-1.

35. **N.Q.Zhao, X.X.Jiang,C.S.Shi,J.J.Li,Z.G.Zhao,and X.W.Du.** *J.Mater.Sci.* 2007, Vol. 42, 2878.

36. **H.Asoh, K.Nishio,M.Nakao,A.Yokoo,T.Tamamura,and H.Masuda.** *J.Vac.Sci.& Technol.B.* 2001, Vol. 19, 569.

37. **H.Masuda, H.Yamada,M.Satoh,and H.Asoh.** *Appl.Phys.Lett.* 1997, Vol. 71, 2770.

38. **J.Choi, K.Nielsch,M.Reiche,R.B.Wehrspohn,and U.Gosele.** *J.Vac.Sci.& Technol.B.* 2003, Vol. 21, 763.

39. **J.Choi, R.B.Wehrspohn,and U.Gosele.** *Adv.Mater.* 2003, Vol. 15, 1531.

40. **C.Xu, S.Bao,L.Kong,and H.Li.** *J.Solid State Chem.* 2006, Vol. 179, 1351.

41. **J.Zou, X.Qi,L.Tan,and B.J.H.Stadler.** *Appl.Phys.Lett.* 2006, Vol. 89, 093106.

42. **C.Y.Peng, C.Y.Liu,N.W.Liu,H.H.Wang,A.Datta,and Y.L.Wang.** *J.Vac.Sci.& Technol.B.* 2005, Vol. 23, 559.

43. **A.Parge, T.Niemann,M.Seibt,and M.Munzenberg.** *J.Appl.Phys.* 2007, Vol. 101, 104302.

44. **S.Kaka, M.R.Pufall,W.H.Rippard,T.J.Silva,S.E.Russek, and J.A.Ketine.** *Nature (London).* 2005, Vol. 437, 389.

45. **A.Saib, M.Darques,L.Piraux,D.J.Vanhoenacker,and I.Huynen.** *IEEE Trans.Microw.Theroy Tech.* 2005, Vol. 53, 2043.

46. **C.A.Ross.** *Phys.Rev.B.* 2002, Vol. 65, 144417.

47. **G.C.Han, B.Y.Zong,P.Luo and Y.H.Wu.** *J.Appl.Phys.* 2003, Vol. 93, 9202.

48. **S.Melle, J.L.Menendez,G.Armelles,D.Navas,M.Vazquez,K.Nielsch,R.B.Wehrspohn,and U.Gosele.** *Appl.Phys.Lett.* 2003, Vol. 83, 4547.

49. **Q.Liu, J.Wang,Z.Yang,and D.Xue.** *Phys.Rev.B.* 2005, Vol. 72, 144412.

50. **J.Zhang, W.Li,G.A.Jones, and T.H.Shen.** *J.Appl.Phys.* 2006, Vol. 99, 08Q502.

51. **W.Schwarzacher, O.I.Kasyutich,P.R.Evans,M.G.Decanini.**

J.Magn.Magn.Mater. 1999, Vol. 198, 185.

52. **V.M.Fedosyuk, W.Schwarzacher,O.I.Kasyutich,and G.Yi.** *Physcis of Low dimensional Structure.* 1999, Vol. 11, 61.

53. **H.J.Blythe, v.M.Fedosyuk,W.Schwarzacher,and O.I.Kasyutich.**

J.Magn.Magn.Mater. 2000, Vol. 208, 251.

54. **L.Piraux, S.Dubois,J.L.duvail,K.Ounadjela, and A.Fert.** *J.Magn.Magn.Mater.* 1997, Vol. 175, 127.

55. **J.M.Garcia, a.Thiaville,J.Miltat.** *J.Magn.Magn.Mater.* 2002, Vol. 249, 163.

56. **K.R.Pirota, and M.Vazquez.** *Adv.Engr.Mater.* 2005, Vol. 7, 1111.

57. **J.Cho, J.U.Wu,J.H.Min,J.Hyun,s.P.Ko,J.Y.Soh,X.Q.Liu, and Y.K.Kim.**

J.Magn.Magn,Mater. 2006, Vol. 303, E281.

58. **M.Darques, a.Encinas,L.Vila,and L.Piraux.** *J.Phys.D: Appl.Phys.* 2004, Vol. 37, 1411.

59. **H.Schwanbeck, and U.Schmidt.** *Electrochimica Acta.* 2000, Vol. 45, 4389.

60. **A.Encinas-Oropesa, M.Demand,L.Piraux,I.Huynen,and U.Ebel.** *Phys.Rev.B.* 2001, Vol. 63, 104415.

61. **M.Darques, L.Piraux,AEncinas,P.G.Bayle,A.Popa,and U.Ebel.** *Appl.Phys.Lett.* 2005, Vol. 86, 072508.

62. **S.Ge.C.Li, X.Ma,W.Li,L.Xi,and C.Li.** *J.Appl.Phys.* 2001, Vol. 90, 509.

63. **J.L.Budendorff, C.Meny,e.Beaurepaire,P.Panissod,and J.P.Bucher.** *Eur.Phys.J.B.* 2000, Vol. 17, 638.

64. **J.Garcia-Otera, M.Porto,J.Rivs,and A.Bunde.** *Phys.Rev.Lett.* 2000, Vol. 84, 167.

65. **J.Escrig, D.Altbir,M.Jaafar,D.Navas,A.Asenjo,and M.Vazquez.** *Phys.Rev.B.* 2007, Vol. 75, 184429.

66. **R.OBarr, and S.Schultz.** *J.Appl.Phys.* 1997, Vol. 81, 5459.

67. **M.Lederman, R.O'Barr,and S.Schultz.** *IEEE Trans.Magn.* 1995, Vol. 31, 3793.

68. **L.Piraux, S.Dubois, E.Ferain, R.Legras, K.Ounadjela, J.M.George, J.L.Mauric,and A.Fert.** *J.Magn.Magn.Mater.* 1997, Vol. 165, 352.

69. **J.E.Wegrowel.** *IEEE Trans.Magn.* 1998, Vol. 34, 903.

70. **K.Liu, K.Ngodawithana,P.C.Searson,and C.L.Chien.** *Phys.Rev.B.* 1995, Vol. 51, 7381.

71. **L.Piraux, J.George,J.Despres,C.Leroy,E.Ferain,R.Legras,K.Ounadjela,and A.Fert.** *Appl.Phys.Lett.* 1994, Vol. 65, 2484.

72. **A.Blondel, B.Doudin,and J.P.Ansermet.** *J.Magn.Magn.Mater.* 1997, Vol. 165, 34.

73. **A.Fabian, C.Terrier,S.SGuisan,P.Guittienne,L.Gravier,and J.P.Ansermet.** *J.Phys: Condens.Mater.* 2006, Vol. 18, 1569.

74. **J.U.Cho, J.H.Min,S.P.Ko,J.Y.Soh,Y.K.Kim,and J.H.Wu.** *J.Appl.Phys.* 2006, Vol. 99, 08C909.

75. **L.Gravier, J.E.Wegrowe,T.Wade,A.Fabian,and J.P.Ansermet.** *IEEE Trans.Magn.* 2002, Vol. 38, 2700.

76. **L.Gravier, S.Serrano-Guisan,and J.P.Ansermet.** *J.Appl.Phys.* 2005, Vol. 97, 10C501.

77. **A.Robinson, and W.Schwarzacher.** *J.Appl.Phys.* 2003, Vol. 93, 7250.

78. **L.Wang, K.Yu-Zhang,A.Metrot,P.Bonhomme,and M.Troyon.** *Thin Solid Films.* 1996, Vol. 288, 86.

79. **M.Chen, P.C.Searson,and C.L.Chier.** *J.Appl.Phys.* 2003, Vol. 93, 8253.

80. **A.Blondel, J.P.Meier, B.Doudin, J.P.Ansermet, K.Attenbourough, R.H.P.Evans, G.Nabiyouni,and W.Schwarzacher.** *J.Magn.Magn.Mater.* 1995, Vol. 148, 317.

81. **G.P.Heydon, S.R.Hoon,S.L.T.A.N.Farley,M.S.Valera,K.Attenbourough,and W.Schwarzacher.** *J.Phys.D:Appl.Phys.* 1997, Vol. 30, 1081.

82. **S.Dubois, E.Chassaning,J.L.Duvail,L.Piraux,and m.G.Waals.** *J.Chem.Phys.* 1999, Vol. 96, 1316.

83. **J.Velev, and Y.C.Chang.** *J.Magn.Magn.Mater.* 2002, Vol. 250, 219.

84. **J.Choi, O.S.Jun,H.Ju,and J.Chon.** *Nano.Lett.* 2005, Vol. 5, 2179.

85. **Y.K.Su, D.H.Qin,H.L.Zhang,H.Li,and H.L.Li.** *Chem.Phys.Lett.* 2004, Vol. 388, 406.

86. **A.Fert, L.Piraux.** *J.Magn.Magn.Mater.* 1999, Vol. 200, 338.

87. **D.M.Edwards, J.Mathon,and R.B.Muniz.** *IEEE Trans.Magn.* 1991, Vol. 3, 3548.

88. **J.Mathon.** *Contemp.Phys.* 1991, Vol. 32, 143.

89. **A.Fert, T.Valet,and J.Barans.** *J.Appl.Phys.* 1994, Vol. 75, 6693.

90. **A.Fert, T.Valet and.** *Phys.Rev.B.* 1993, Vol. 75, 6693.

91. **C.Kittel, M.A.Ruderman and.** *Phys.Rev.B.* 1954, Vol. 96, 99.

92. **T.Kasuya.** *Prog.Theor.Phys.* 1956, Vol. 16, 4558.

93. **S.Dubois, C.Marchal, J.M.Beuken, L.Piraux, J.L.Duvail, A.Fert, J.M.George, and L.Maurice.** *Appl.Phys.Lett.* 1997, Vol. 70, 396.

94. **L.Piraux, J.M.George, J.F.Despres, C.Leroy, E.Ferain, R.Legras, K.Ounadjela, A.Fert.** *Appl.Phys.Lett.* 1994, Vol. 65, 2484.

95. **L.Piraux, S.Dubois, C.Marchal, J.M.Beuken, L.Filipozzi, J.F.Despres, K.Ounadjela, and A.Fert.** *J.Magn.Magn.Mater.* 1996, Vol. 156, 317.

96. **K.Liu, K.Nagodawithana,P.C.Searson,and C.L.Chien.** *Phys.Rev.B.* 1995, Vol. 51, 7381.

97. **D.Pullini, G.Innocenti,D.Busquests and A.Rultolo.** *Appl.Phys.Lett.* 2007, Vol. 90, 133106.

98. **K.Liu, K.Nagodawithana,P.Searson,and C.Chien.** *Phys.Rev.B.* 1995, Vol. 51, 7381.

99. **A.Encinas, M.Demand,J.M.George,and L.Piraux.** *IEEE Trans.Magn.* 2002, Vol. 38, 2574.

100. **M.Darques, A.S.Bogaert,F.Elhoussine,and L.Piraux.** *J.Phys.D:Appl.Phys.* 2006, Vol. 39, 5052.

101. **J.U.Cho, J.Wu,J.H.Min,J.H.Lee,H.Liu,and Y.K.Kim.** *J.Magn.Magn.Mater.* 2007, Vol. 310, 2420.

102. **B.J.H.Stadler, L.Tan and.** *J.Mater.Res.* 2006, Vol. 21, 2870.

103. **I.Enculescu, M.E.Toimil-Molares,C.Zet,M.Daub,L.Westerberg,R.Neumann,and R.Spohr.** *Appl.Phys.A.* 2007, Vol. 86, 43.

104. **J.De La Torre Medina, m.Darques,T.Blon,L.Piraux, and A.Encinas.** *Phys.Rev.B.* 2008, Vol. 77, 014417.

105. **P.Nallet, e.Chassaning,M.G.Waals,and M.J.Hytch.** *J.Appl.Phys.* 1996, Vol. 79, 6884.

106. **A.Fabian, C.Terrier,S.Serrano Guisan, X.Hoffer, M.Dubey, L.Gravier, J.P.Ansermet, and J.E.Wegrwe.** *Phys.Rev.Lett.* 2003, Vol. 91, 257209-1.

107. **A.Fabian, C.Terrier,S.S.Guisan X.Hoffer,M.Dubery,L.Gravier,and J.P.Ansermet.** *Phys.Rev.Lett.* 2003, Vol. 91, 257209.

108. **F.B.mancoff, N.D.Rizzo,B.N.Engle,and S.Tehrani.** *Nature (London).* 2005, Vol. 437, 393.

109. **T.Blon, .M.Tempfli, S.M.Tempfli, L.Piraux, S.Fusil, r.Guilemet, K.Bouzehouane, C.Dranlot,and V.Cros.** *J.Appl.Phys.* 2007, Vol. 102, 103906.

110. **L.Piraux, K.Renard,and R.Guilemet.** *Nano.Lett.* 2007, Vol. 7, 2563.

111. **J.E.Wegrowel, X.Hoffer,P.Guittienne,A.Fabian,L.Gravier,T.Wade,and J.P.Ansermet.** *J.Appl.Phys.* 2002, Vol. 91, 6806.

112. **X.Huang, L.Tan,H.Cho.and B.J.H.Stader.** *J.Appl.Phys.* 2009, Vol. 105, 07D128.

113. **S.K.Thamida, and H.Chang.** *Chaos.* 2002, Vol. 12, 240.

114. **C.Hennesthal.** *JPK instruments AG.* 2003, Vol. 1.

115. **L.Tan.** *Ph.D dissertation.* University of Minnesota, 2008.

116. **F.Keller, M.S.Hunter,and D.L.Robinson.** *J.Electochem.Soc.* 1953, Vol. 100, 411.

117. **J.W.Diggle, T.C.Downie,and C.W.Coulding.** *Chemical Review.* 1969, Vol. 69, 365.

118. **L.Piraux, J.M.George, J.F.Despres,C.Leroy, E.Ferain,R.Legras, K.Ounadjila, and A.Fert.** *Appl.Phys.Lett.* 1994, Vol. 65, 2484.

119. **L.Piraus, s.Dubois,A.Fert,L.Belliard.** *Eur.Phy.J.B.* 1998, Vol. 4, 413.

120. **M.Getzlaff.** *Fundameantals of Magnetism.* 2008.

121. **A.Fert, and T.Valet.** *Phys.Rev.B.* 1993, Vol. 48, 7099.

122. **M.J.Carya, N.Smith,S.Maat,J.R.Childress.** *Appl.Phys.Lett.* 2008, Vol. 93, 102509.

123. **J.C.Slonczewski.** *J.Magn.Magn.Mater.* 1996, Vol. 159, L1.

124. **J.Z.Sun, D.J.Monsma,d.W.Abraham,M.J.Rooks,and R.H.Koch.** *Appl.Phys.Lett.* 2002, Vol. 81, 2202.

125. **J.E.Wegrowe.** *Phys.Rev.B.* 2003, Vol. 68, 214414.

126. **P.D.McGary, L.Tan,J.Zou,B.J.H.Stadler,P.Downey,and A.Flatau.**

J.Appl.Phys. 2006, Vol. 99, 08B310.

127. **http://ruppweb.dyndns.org/.**

128. **http://en.wikipedia.org/wiki/Atomic_force_microscope.**

129. **www.britannica.com.**

130. **K.Nielsch, P.B.Wehrspohn,J.Barthel,J.Kirschner,U.Gosele,S.F.Fischer,and**

H.Kronmuller. *Appl.Phys.Lett.* 2001, Vol. 79, 1360.

131. **H.Masuda, M.Ohya,H.Asoh,M.Nakao,M.Nohtomi,and T.Tamamura.**

Jpn.J.Appl.Phys. 1999, Vol. 238, L1403.

132. **A.P.Li, F.Muller,and U.Gosele.** *Electochem.& Solid-State Lett.* 2000, Vol. 3,

131.

133. **F.Nasirpouri, P.Southern,M.Ghorbani,A.Irajizad,and W.Schwarzacher.**

J.Magn.Magn.Mater. 2007, Vol. 308, 35.

134. **C.G.Khan Malek, and S.S.Das.** *J.Vac.Sci.Technol.B.* 1998, Vol. 16, 3543.

135. **R.C.Furneaux, W.R.Rigby,A.P.Davidson.** *Nature.* 1989, Vol. 337, 147.